

学位論文

Superconducting gap in the iron-based  
superconductor  $\text{BaFe}_2(\text{As}_{1-x}\text{P}_x)_2$  studied by  
angle-resolved photoemission spectroscopy  
(角度分解光電子分光による鉄系超伝導体  
 $\text{BaFe}_2(\text{As}_{1-x}\text{P}_x)_2$  の超伝導ギャップの研究)

平成27年12月博士（理学）申請

東京大学大学院理学系研究科

物理学専攻

徐 健



**Superconducting gap in the iron-based  
superconductor  $\text{BaFe}_2(\text{As}_{1-x}\text{P}_x)_2$  studied by  
angle-resolved photoemission spectroscopy**

**THESIS**

Jian Xu

Department of Physics, University of Tokyo

December, 2015



# Abstract

The discovery of the iron-based high critical transition temperature ( $T_c$ ) superconductors has aroused a new wave of investigations on the high  $T_c$  superconductors. The key point of the investigations on the high  $T_c$  superconductors is the pairing mechanism, which is reflected by the superconducting gap symmetry. Other than the cuprate superconductors, the gap symmetry of the iron-based superconductors has been controversial in many iron-based superconductors. To solve this problem, using angle-resolved photoemission spectroscopy (ARPES), we investigated the isovalent doped  $\text{BaFe}_2(\text{As}_{1-x}\text{P}_x)_2$ , in which no charge doping is involved.

The analysis method of the superconducting gap is important. Therefore, prior to judging what the spectrum detected by ARPES corresponds to, we analyzed the possible orbitals of the available spectrum by calculating the polarization dependent photoemission response using the electric dipole selection rules. According to the comparison between experimental and calculated results, the orbital character of the Fermi surface in  $\text{BaFe}_2(\text{As}_{1-x}\text{P}_x)_2$  was determined.

Moreover, the bands and Fermi momenta ( $k_F$ s) were determined through the fitting of each momentum distribution curve (MDC) using a Lorentzian-Gaussian function. After that the energy distribution curves (EDCs) were selected based on  $k_F$ ; the value of superconducting gap ( $\Delta$ ) on the  $k_F$  was given by the fitting of symmetrized EDCs to the Norman function.

The superconducting gap symmetry on the electron Fermi surfaces was analyzed at different  $k_F$  positions as obtained from the analysis above. Through ARPES measurements, we obtained the superconducting gap of  $\text{BaFe}_2(\text{As}_{1-x}\text{P}_x)_2$  for a series of doping concentration, including the optimal doping ( $x = 0.3$ ) and over doping ( $x = 0.34$ ,  $x = 0.38$ , and  $x = 0.45$ ). We mainly studied the superconducting gaps on the electron Fermi surfaces as well as those on the hole Fermi surfaces, and consider that the complexity of the superconducting gap symmetry in  $\text{BaFe}_2(\text{As}_{1-x}\text{P}_x)_2$  comes from the competition of spin and orbital fluctuations.

In heavily doped materials ( $x = 0.45$ ), we conclude that the spin fluctuation is dominant based on strongly anisotropic of superconducting gap and nodes on the edge of the Electron Fermi surface comparing with the previous theoretical study; with decreasing doping, for example, at  $x = 0.38$ , the effect of orbital fluctuation turns significant. In fact, the spin fluctuation also increases with decreasing doping; yet the orbital fluctuation increases faster, as suggested by the increasing of gap size and the decreasing of the anisotropic of superconducting gap symmetry with decreasing doping, which compared with the previous theoretical study. The orbital fluctuation becomes dominant when  $x < 0.34$ ; near the optimal doping or even

prior to that (slightly over doping region), the orbital fluctuation decreases abruptly while spin fluctuation continues increasing. The conclusion here has solved the contradiction appeared in some previous studies, and is consistent with the previous theoretical and experimental results, such as the theoretical superconducting gap calculation considering competition of spin and orbital fluctuations. It is found that the competition of spin and orbital fluctuations appears in the optimal doping and slightly over doping region, where one of two fluctuations becomes dominant depending on the doping concentration. We believe that the pairing symmetry changing from nodal  $s$ -wave to  $s_{\pm}$ -wave corresponds to the doping ration  $x = 0.45$  to the optimal doping.

All the codes for analyzing the polarization dependent photoemission response, MDC/EDC,  $k_F$ , and superconducting gap were written by software IGOR.

# Contents

<b>1</b>	<b>Introduction</b>	<b>3</b>
1.1	History . . . . .	3
1.2	Thesis motivation . . . . .	5
1.3	Thesis structure . . . . .	5
<b>2</b>	<b>Background</b>	<b>7</b>
2.1	Superconductors . . . . .	7
2.2	High- $T_c$ cuprate superconductors . . . . .	7
2.2.1	Crystal structure . . . . .	8
2.2.2	Strongly correlated electron system . . . . .	10
2.2.3	Gap structure . . . . .	12
2.2.4	Phase diagram . . . . .	14
2.3	Iron-based superconductors . . . . .	15
2.3.1	Crystal and electronic structure . . . . .	15
2.3.2	Orbital character of energy bands . . . . .	17
2.3.3	Phase diagram . . . . .	17
2.4	Superconducting gap . . . . .	20
2.4.1	Experimental studies . . . . .	20
2.4.2	Theoretical studies . . . . .	26
2.5	Physical properties of P doped $\text{BaFe}_2\text{As}_2$ . . . . .	28
<b>3</b>	<b>Experimental methods</b>	<b>39</b>
3.1	Principles of photoemission spectroscopy . . . . .	39
3.1.1	Photoemission spectroscopy . . . . .	39
3.1.2	Angle-resolved photoemission spectroscopy (ARPES) . . . . .	41
3.1.3	Spectral function and self-energy . . . . .	45
3.1.4	Electron escape depth . . . . .	49
3.2	Experimental setup . . . . .	51
3.2.1	PF BL-28A . . . . .	51
3.2.2	SSRL BL-5-4 . . . . .	51

<b>4</b>	<b>Analysis of ARPES spectra</b>	<b>57</b>
4.1	Electric dipole approximation and selection rules . . . . .	57
4.2	Polarization dependent photoemission response . . . . .	58
4.2.1	Experimental measured and theoretical calculated spectra using linearly polarized light . . . . .	58
4.3	Method of spectral analysis . . . . .	62
4.4	Method of gap estimation . . . . .	65
4.5	Summary . . . . .	66
<b>5</b>	<b>Superconducting gap</b>	<b>69</b>
5.1	Introduction . . . . .	69
5.2	Experimental results of ARPES . . . . .	70
5.2.1	$k_z$ mapping on the Fermi surfaces . . . . .	70
5.2.2	Superconducting gap on the electron Fermi surfaces . . . . .	70
5.2.3	Superconducting gap on the hole Fermi surfaces . . . . .	82
5.3	Discussion about the superconducting gap . . . . .	87
5.3.1	Orbital fluctuation . . . . .	87
5.3.2	Spin fluctuation . . . . .	89
5.3.3	Competition between spin and orbital fluctuations . . . . .	91
5.4	Analysis of the superconducting gap on the hole Fermi surfaces . . . . .	92
5.5	Summary . . . . .	94
<b>6</b>	<b>Conclusions and prospects</b>	<b>97</b>
6.1	Conclusions . . . . .	97
6.2	Prospects . . . . .	98

- Symbols and Units

Symbol	Physical Quantity	Units
$A$	Photoemission spectrum	-
$a, b, c$	Lattice constants	Å
$c, c^+$	Annihilation and creation operators	-
$d, p$	$d$ and $p$ orbit	-
$E$	Energy	J, eV
$E_B, E_{kin}, E_F$	Kinetic, binding, and Fermi energy	eV
$E_P$	Pass energy	eV
$e$	Charge of electron	C
$\varepsilon(\mathbf{q}, \omega)$	dielectric function	F m <sup>-1</sup>
$G$	Arbitrary reciprocal lattice vector	m <sup>-1</sup>
$G$	Green's function	-
$H$	Hamilton	eV
$h(\hbar)$	Planck constant (Dirac constant)	eV · s
$h, k, l$	Miller indices	1
$i, j$	Site indices	-
$k_B$	Boltzmann coefficient	JK <sup>-1</sup>
$k$	Wave number	m <sup>-1</sup>
$k_x, k_y, k_z$	Wave number in $x, y,$ and $z$ direction	m <sup>-1</sup>
$k_F$	Fermi wave number	m <sup>-1</sup>
$l_k$	Mean free path	m
$m^*$	Effective mass	kg
$n$	Carrier concentration	-
$n$	Operator	-
$P$	Pressure	Pa
$p$	Electron momentum	N · s
$p_x, p_y, p_z$	Electron momentum in $x, y,$ and $z$ direction	N · s
$R_H$	Hall coefficient	cm <sup>3</sup> /C
$R_0$	Mean radius of hemisphere analyzer	cm
$S_{ab}$	Seebeck coefficient	μV/K
$T$	Temperature	K
$T_c$	Critical temperature of superconductors	K
$t, t', t''$	Transfer intergrals between the nearest, second nearest, and third nearest neighbor sites	eV
$U$	On-site Conlomb interaction	eV
$U_p, U_d$	On-site Conlomb interaction on O and Cu sites	eV
$v_F$	Fermi velocity	m/s

Symbol	Physical Quantity	Units
$w$	Slit width	m
$Z_k$	Residue of pole	1
$\alpha$	Acceptance angle of the slit	rad
$\Delta_{SC}$	Superconducting gap	eV, meV
$\Delta_{CT}$	Charge transfer energy	eV
$\delta$	Phase Delay	rad
$\delta$	A small quantity	1
$\epsilon_k$	Dispersion	eV
$\varepsilon$	Incommensurability	1
$\theta$	Space angle	rad
$\lambda$	Escape depth	nm
$\mu$	Chemical potential	eV
$\nu$	Frequency	Hz
$\rho$	Electrical resistivity	m $\Omega$ cm, $\mu\Omega$ cm
$\Sigma$	Self energy	eV
$\sigma$	Spin index	-
$\Phi$	Work function	eV
$\phi, \varphi$	Space angle	rad
$\tau$	Mean lifetime of electrons	s
$\chi$	Magnetic susceptibility	emu/g
$\Psi$	State function	-
$\omega$	Energy	eV

# Chapter 1

## Introduction

### 1.1 History

Superconductors are certain materials with zero electrical resistance and perfect diamagnetism when they are cooled to a temperature lower than a critical point; owing to which they exhibited great potential in application [1].

In 1911, a Dutch scientist Heike K. Onnes observed that the electrical resistivity of mercury dropped abruptly to zero, which is usually called superconductivity [2]. Subsequent researches confirmed the universality of this phenomenon; in many other elemental metal and compounds the superconductivity also appeared [3]. In addition to zero resistivity at low temperature, another typical characteristic called the Meissner effect was observed by W. Meissner and R. Ochsenfeld in year 1933 [4]. In the superconducting state, the interior magnetic field is completely expelled from the superconductors [4]. The Meissner effect would be broken if a sufficient high magnetic field was applied. According to how the Meissner effect vanishes, the superconductors can be categorized into two types.

Until 1986, amounts of superconductors had been reported, including metals, alloys, oxides, organic compounds, and so on [5–8]. The critical temperatures ( $T_c$ ) of superconducting transformation in these materials are very low [5, 8]. Therefore, at that time superconductivity was regarded as an interesting physical phenomenon rather than one with application potential [3].

The variety of the structure symmetry aroused the continuous survey for inner mechanisms of superconductivity. The first theoretical breakthrough was proposed by John Bardeen, Leon Cooper, and John Robert Schrieffer (BCS theory) in 1957 [9]. BCS theory enabled in describing superconductivity as a microscopic effect derived from the boson-like state of Cooper pairs coming from the interaction between the electrons and the phonons [9]. Conventional superconductivity could be well explained by BCS theory. According to calculation using BCS theory, a maximum  $T_c$  was predicted to be about 40 K (controversial), which is consistent

with the low  $T_c$  in abovementioned superconductors. In addition, some novel physical phenomena appeared in the superconductors, like the coexistence with charge density wave or spin density wave, which require further study [10].

In year 1986, the discovery of high  $T_c$  cuprate superconductors [11] broke the  $T_c$  limitation predicted by BCS theory [12], uncovering a new page of the research on the superconductivity. In the subsequent competition in surveying high  $T_c$  cuprate superconductors,  $\text{YBa}_2\text{Cu}_3\text{O}_7$  was found to possess a  $T_c$  above liquid nitrogen temperature [13], which is a significant signal for practical application. Until now the champion of cuprate superconductors is  $\text{HgBa}_2\text{Ca}_2\text{Cu}_3\text{O}_{9-\delta}$  with a  $T_c$  higher than 130 K at room pressure and 164 K at high pressure [14, 15]. The cuprate superconductors are in multi-layered perovskite crystal structures containing  $\text{CuO}_2$  plane(s) [16, 17], which is a strongly correlated system, is the basic part of the cuprate superconductors. Detailed introduction of the layered structure and related mechanism will be presented in chapter 2.

Later, BCS superconductor  $\text{MgB}_2$  which has a  $T_c$  of about 40 K was discovered in 2001 [18]. In addition, heavy Fermion superconductors and carbon superconductors were also discovered and attracted attention of many researchers. Recently, it was reported that  $\text{H}_2\text{S}$  has a  $T_c$  as high as 203 K under high pressure [19].

Recently, the iron-based superconductors, a new family of the superconducting materials, were discovered one after another since 2008, when H. Hosono group reported a  $T_c$  of 26 K in fluorine-doped  $\text{LaFeAsO}$  [20]. The antiferromagnetism of parent compound  $\text{LaFeAsO}$  indicated new characteristics, which excited a new wave of experimental and theoretical researches [21, 22]. In these several years, typical structures of iron-based superconductors have been revealed, such as 11 ( $\text{FeSe}$ ), 111 ( $\text{LiFeAs}$ ), 122 ( $\text{BaFe}_2\text{As}_2$ ), 1111 ( $\text{LaFeAsO}$ ), and so on [23–26]. Modifications have been carried out to the parent compounds, including hole doping, electron doping, and isovalent doping to each site [27–29].

Proximity of superconductivity and antiferromagnetism in iron-based materials triggered a wave of experimental and theoretical studies. Spin and orbital fluctuation mechanisms of superconductivity and complex pairing symmetry were suggested and mentioned in amounts of experimental and theoretical studies. Various kinds of iron-based superconductors were discovered in succession. Such as different structures of 11 ( $\text{FeSe}$ ) [23], 111 ( $\text{LiFeAs}$ ) [24], 122 ( $\text{BaFe}_2\text{As}_2$ ) [30], 1111 ( $\text{LaFeAsO}$ ) [26] with hole doping, electron doping, and isovalent doping. Among those iron-based superconductors  $\text{BaFe}_2(\text{As}_{1-x}\text{P}_x)_2$  has attracted much attention because of the presence of superconducting gap nodes [29]. Detailed introduction to the structure, gap symmetry, and properties of these materials will be given in chapter 2.

## 1.2 Thesis motivation

In this thesis, the angle-resolved photoemission spectroscopy (ARPES) is taken as a main tool to study the gap structure in iron-based superconductors. The purpose is to observe the electronic band structure and directly reveal the gap structure. The following problems were encountered and relevant solutions were explored:

(1) For investigating the anisotropic of superconducting gap symmetry, it is important to distinguish the  $k_F$  on the different Fermi surface sheets in the experimental spectrum. And we cannot exclude if the outer Electron Fermi surface mixing or not with the inner Electron Fermi surface in the strong intensity on the edge of spectrum measured using circularly polarized by a simple second derivative on the ARPES spectrum. Then therefore, we calculate polarization dependent photoemission response using electric dipole approximation and selection rules, and find out that outer Electron Fermi surface does not mix with the inner ones.

(2) For obtaining the value of superconducting gap, it is important for us to obtaining the right  $k_F$ . It is roughly to infer the position of  $k_F$  by eye or only fitting the momentum distribution curve (MDC) near the Fermi surface. Then therefore, we fit the amounts of MDCs using the Lorentzian-Gaussian function for obtaining the band structure and get the  $k_F$ . And then fitting the symmetrized energy distribution curves (EDCs) by the Norman function and obtain the fitting result gap  $|\Delta|$ .

(3) Nodes (or at least obviously very small gap) exists around the two 1/4 regions of the two edges on the inner Electron Fermi surface in the  $\text{BaFe}_2(\text{As}_{1-x}\text{P}_x)_2$  ( $x = 0.38$ ) was reported in previous ARPES study (unpublished). Then therefore, we measured several different samples of the same doping composition ( $x = 0.38$  and  $x = 0.34$ ) several times in the same experimental condition using different polarized light for searching the nodes and get a serious conclusions consistent of superconducting gap symmetry, and did not find the nodes.

(4) Although the superconducting gap size on the inner election pocket in  $x = 0.3, 0.34, 0.38$  and  $0.45$  systematically decreases with the doping percentage, which is consistent with the tendency of  $T_c$ , the superconducting gap symmetry has not a linear relationship between the anisotropy and  $x$ . We solve this problem by considering the competition of spin and orbital fluctuations.

## 1.3 Thesis structure

In this thesis, the superconducting gap symmetry of  $\text{BaFe}_2(\text{As}_{1-x}\text{P}_x)_2$  was studied via angle-resolved photoemission spectroscopy (ARPES). This thesis is organized as follows.

In chapter 1, the history of superconductivity is introduced. The motivation and structure of this thesis are described.

In chapter 2, the crystal structure, strongly correlated electron system, gap structure, and phase diagram of cuprate and iron-based superconductors are introduced successively. The superconducting gap in iron-based superconductors and physical properties of P-BaFe<sub>2</sub>As<sub>2</sub> are then presented.

In chapter 3, the principles of photoemission spectroscopy, especially the ARPES are given. Important equations of spectral function, self-energy, and electron escape depth are then deduced. At last the experimental setup of adopted two ARPES lines are introduced.

In chapter 4, the method of ARPES spectral analysis are introduced. Electric dipole approximation and selection rules are used to calculate the polarization dependent photoemission response for distinguishing the orbital characters in the spectrum. The Lorentzian-Gaussian function is used to fit MDCs for obtaining the band structure and  $k_F$ . The Norman function is used to fit the symmetrized EDC and obtain the superconducting gap. Abundant experimental results of superconducting gap were presented using the method mentioned in this chapter.

In chapter 5, the experimental results of superconducting gap symmetry on the Electron Fermi surfaces in BaFe<sub>2</sub>(As<sub>1-x</sub>P<sub>x</sub>)<sub>2</sub> ( $x = 0.3, 0.34, 0.38$  and  $0.45$ ) are introduced. Several superconducting gap on the hole pockets are also introduced. We analyse the possibility of the competition of spin and orbital fluctuations exists in the BaFe<sub>2</sub>(As<sub>1-x</sub>P<sub>x</sub>)<sub>2</sub>. In addition, theoretical analysis of the experimental results was carried out and compared to the previous theory. The superconducting gap results of BaFe<sub>2</sub>(As<sub>1-x</sub>P<sub>x</sub>)<sub>2</sub> were also discussed, which suggested that the competition of spin and orbital fluctuations change with the doping concentration  $x$ .

In chapter 6, abovementioned results are summarized; concluding remarks and prospects are made.

At last, acknowledgements and cited references are listed.

# Chapter 2

## Background

### 2.1 Superconductors

As we introduced in chapter 1, various superconductors have been reported [5–8]. The reported year and critical temperature  $T_c$  of several typical superconductors are summarized in Fig. 2.1 [31]. It is noticed that the reported maximum  $T_c$  increases slowly before 1980s; while an abrupt increase appeared after 1986. The discovery of cuprate superconductors as well as H<sub>2</sub>S with a  $T_c$  of 203 K at high pressure (top right corner in Fig. 2.1) has greatly enhanced people's confidence in practical application of superconductors [19].

To date, according to the structure and contained elements, the superconductors can be categorized into several types: metals and alloys, cuprate superconductors, heavy Fermion superconductors, carbon superconductors, organic superconductors, and recently reported iron-based superconductors [31]. The superconductivity of each appeared owing to its own mechanism, and some of them still need further investigation; yet they also have some similarities. For example, layered structure proved to be crucial in cuprate, iron-based superconductors as well as MgB<sub>2</sub> [18]. Hence, it is instructive to review the previous studies.

### 2.2 High- $T_c$ cuprate superconductors

Cuprate superconductors, as the first system breaking the McMillan rule [12] predicted by BCS theory, exhibit significant research value on both physical mechanism and application prospect. Especially, the investigation on the structures and coupling mechanisms is inspiring. In this section, a brief review of crystal structure, gap structure, and phase diagram in the cuprate superconductors will be introduced.

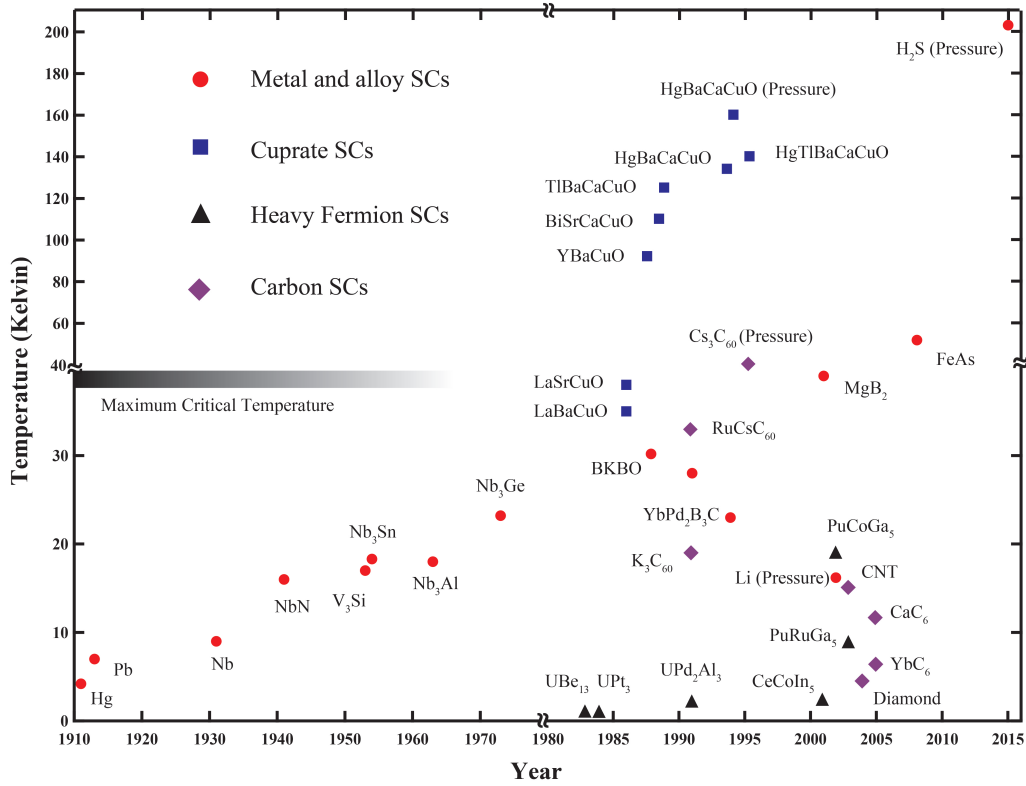


Figure 2.1: Reported years and  $T_c$  of typical superconductors; red, blue, black, and purple points denote metal and alloy, cuprates, heavy Fermion, and carbon superconductors, respectively.

## 2.2.1 Crystal structure

High- $T_c$  cuprate superconductors possess multi-layered perovskite crystal structures containing singular or plural  $\text{CuO}_2$  planes [16, 17]. In the multi-layered perovskite structures, the electronic states on the  $\text{CuO}_2$  planes play an important role in the properties of high- $T_c$  superconductivity and low energy excitations. As illustrated in Fig. 2.2(a), the 2-dimensional  $\text{CuO}_2$  layers can be observed in the schematic crystal structure of  $\text{La}_{2-x}\text{Sr}_x\text{CuO}_4$  [32, 33]. The  $\text{CuO}_2$  planes with charge carriers are clamped by charge reservoir layers. The number of layers of the  $\text{CuO}_2$  planes  $n$  can be 1 - 4. For example, the hole-doped superconductor  $\text{YBa}_2\text{Cu}_3\text{O}_7$  [13] has two  $\text{CuO}_2$  layers, i.e.,  $\text{CuO}_2$ -Y- $\text{CuO}_2$  double layer structure [34]; this double layer structure is usually taken as superconductive layer while the other parts are considered as carrier reservoir layer. The  $\text{CuO}_2$  chain [35] in the carrier reservoir layer can adjust the carrier concentration of the superconductive layer. In addition, it also affects the carrier distribution and transporting properties [36].

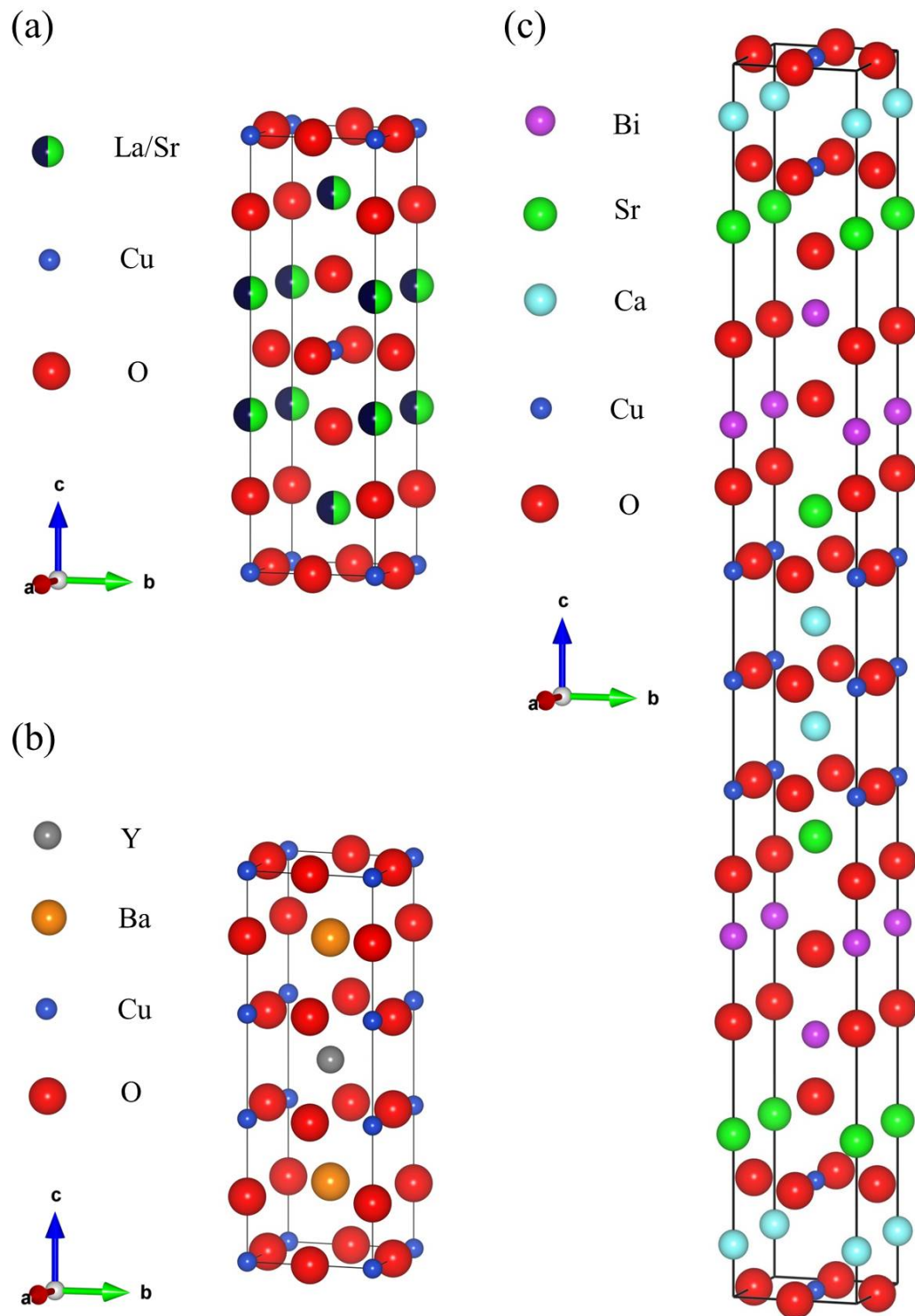


Figure 2.2: Schematic crystal structure of (a)  $\text{La}_{2-x}\text{Sr}_x\text{CuO}_4$  [33] with one  $\text{CuO}_2$  layer, (b)  $\text{YBa}_2\text{Cu}_3\text{O}_7$  [13] with two  $\text{CuO}_2$  layers, and (c)  $\text{Bi}_2\text{Sr}_2\text{Ca}_2\text{Cu}_3\text{O}_{10+\delta}$  [37] with three  $\text{CuO}_2$  layers. Structures are performed by software VESTA [38].

## 2.2.2 Strongly correlated electron system

The key element of the high- $T_c$  cuprate superconductors,  $\text{CuO}_2$ , belongs to Mott insulator, which is one typical strongly correlated electron system. The strongly correlation in  $\text{CuO}_2$  comes from strong on-site Coulomb repulsion. For the record, Mott insulator is special because it should be metal based on band theory but it's not [39]. Mott insulator can be described by the Hubbard model and its Hamiltonian can be expressed by:

$$H = \sum_{i,j,\sigma} t_{ij} c_{i\sigma}^\dagger c_{j\sigma} + U \sum_i n_{i\uparrow} n_{i\downarrow}, \quad (2.1)$$

in which,  $i$  and  $j$  are site indices,  $\sigma$  is spin index,  $t_{ij}$  is hopping integral,  $c_{i\sigma}^\dagger$  and  $c_{j\sigma}$  are creation and annihilation operators, operator  $n_{i\sigma} = c_{i\sigma}^\dagger c_{j\sigma}$ , and  $U$  is the on-site Coulomb interaction, respectively. Figure 2.3(a) shows the schematic diagram of the electronic structure that can be described by the Hubbard model.

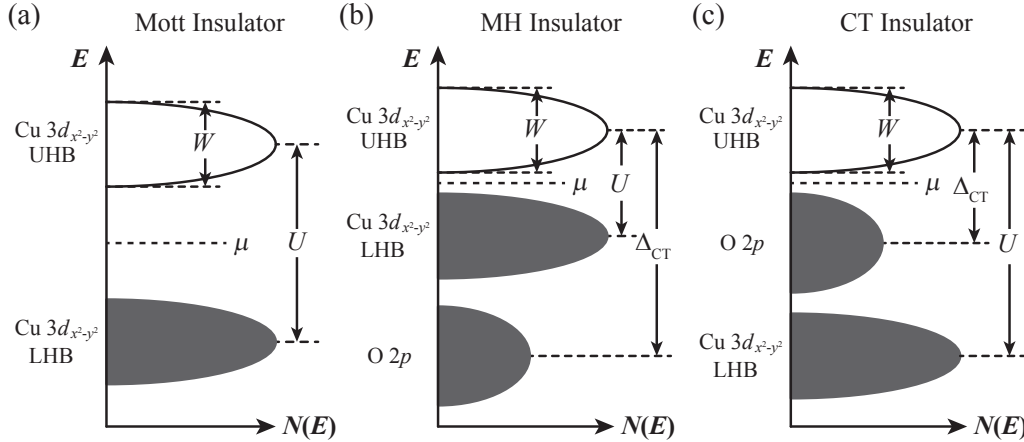


Figure 2.3: Schematic pictures for the electronic structure of (a) the Hubbard model and (b), (c) the three band Hubbard model. (b) Mott-Hubbard (MH) insulator when  $\Delta_{\text{CT}} > U$ . (c) charge transfer (CT) insulator when  $\Delta_{\text{CT}} < U$  [40].

Mott insulator can be categorized into the Mott-Hubbard (MH) insulators and the charge transfer (CT) ones [40], depending on  $\Delta_{\text{CT}}$ , as shown in Fig. 2.3(b)-(c). Doping can transform Mott insulators into some unique metal, like high- $T_c$  cuprate superconductors, most of which are hole-doped charge transfer insulators [41]. The  $\text{Cu } 3d_{x^2-y^2}$  orbital and the  $\text{O } 2p_x$  and  $2p_y$  orbitals on the  $\text{CuO}_2$  plane determine the important properties of the cuprate superconductors, which were verified by amounts of theoretical and experimental studies [42, 43]. Therefore, the Hamiltonian of the cuprate superconductors can be described by a three band model [44], as

expressed by:

$$\begin{aligned}
 H = & \sum_{l\sigma} \varepsilon_p p_{l\sigma}^\dagger p_{l\sigma} + \sum_{i\sigma} \varepsilon_d d_{i\sigma}^\dagger d_{i\sigma} + \sum_{\sigma\langle il\rangle} t_{pd} (p_{l\sigma}^\dagger d_{i\sigma} + d_{i\sigma}^\dagger p_{l\sigma}) \\
 & + \sum_l U_p p_{l\uparrow}^\dagger p_{l\uparrow} p_{l\downarrow}^\dagger p_{l\downarrow} + \sum_i U_d d_{i\uparrow}^\dagger d_{i\uparrow} d_{i\downarrow}^\dagger d_{i\downarrow}, \quad (2.2)
 \end{aligned}$$

in which,  $l$  and  $i$  are the positions of O sites and Cu sites; subscripts  $p$  and  $d$  are indexes of  $p$  orbital on O sites and  $d$  orbital on Cu sites;  $\varepsilon_p$  and  $\varepsilon_d$  are dispersion relation of electron;  $t_{pd}$  is hopping integral between O and Cu on the  $\text{CuO}_2$  plane;  $\langle il \rangle$  is the sum of nearest neighbour of Cu and O sites;  $p_{l\sigma}^\dagger$  ( $d_{i\sigma}^\dagger$ ) and  $p_{l\sigma}$  ( $d_{i\sigma}$ ) are creation and annihilation operators of  $p$  ( $d$ ) orbit;  $U_p$  and  $U_d$  are the on-site Coulomb interaction on O and Cu atoms in the  $\text{CuO}_2$  plane, respectively [45–47].

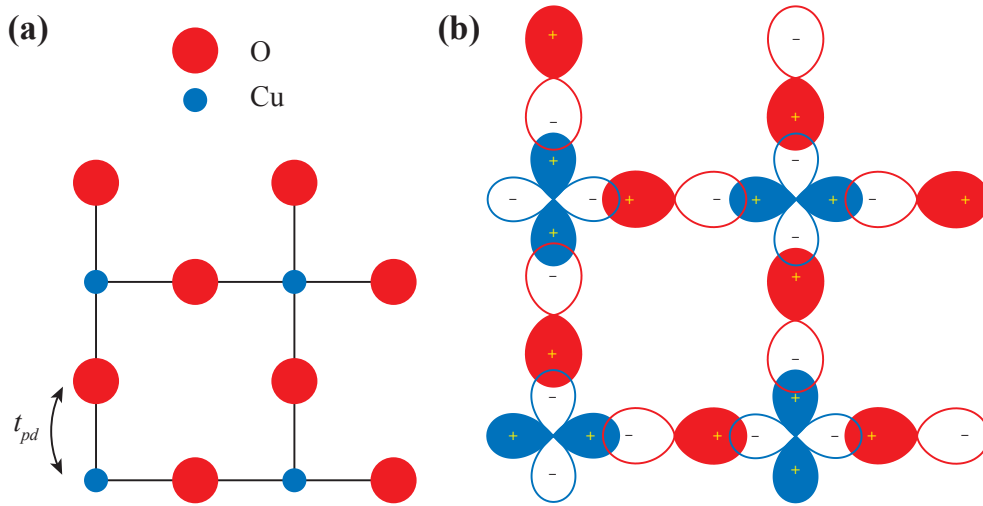


Figure 2.4: Schematic diagram of (a) the  $\text{CuO}_2$  plane and (b) the electronic orbital order; red and blue denotes the oxygen and copper sites.

The effect of  $p$  orbital in the Mott insulators may result in the distinguishing of Mott-Hubbard insulators (MH insulator) or charge transfer insulators (CT insulator) [40]. When only the  $d$  orbital of Cu is considered, as shown in Fig. 2.3(a), the Hubbard model expressed by Eq. 2.1 gives two bands above and below the Fermi surface, called upper Hubbard band and lower Hubbard band, respectively. In Fig. 2.3(a), Hubbard energy  $U$  is the band gap between upper and lower Hubbard bands and  $W$  is the width of the valence band; Mott insulators would turn into conductors when  $W > U$ . In the three band model expressed by Eq. 2.2,  $p$  orbitals of O are also taken into account as well as  $d$  orbitals of Cu, as described by an additional  $p$  band in Fig. 2.3(b)-(c). In Fig. 2.3(b)-(c),  $\Delta_{\text{CT}}$  is the charge transfer energy;

and the size relationship between  $U$  and  $\Delta_{\text{CT}}$  mainly decides the type of the Mott insulators. When  $\Delta_{\text{CT}} > U$ , the insulators are called Mott-Hubbard insulators, in which the excited charge transport is mainly contributed by the  $d$  orbital electrons. On the contrary, when  $\Delta_{\text{CT}} < U$ ,  $p$  orbital electrons could be excited to  $d$  orbital under the fundamental excitation, called charge transfer insulators.

Schematic diagram of the  $\text{CuO}_2$  planes and the electronic orbitals are shown in Fig. 2.4. In Fig. 2.4(a),  $t_{pd}$  is the hopping intergral between the adjacent Cu and O sites; while the interaction is illustrated by the overlapping of electron cloud in Fig. 2.4(b) [3].

The physical properties of Mott insulators can be modified by doping (isovalent doping, hole doping and electron doping) [27–29]. The isovalent doping mainly affects the crystal structure of the materials [29]. In the hole doped Mott-Hubbard insulators the holes are doped in the lower Hubbard band while in the hole doped charge transfer insulators the holes are doped in the  $p$  band [28, 48]. In the electron doped Mott-Hubbard and charge transfer insulators, the electrons are doped in the upper Hubbard band [48]. Noticed that the Hubbard energy  $U$  is about 7 eV and the charge transfer energy  $\Delta_{\text{CT}}$  is about 1.5 eV - 2 eV in the high  $T_c$  cuprate superconductors [49] ( $U > \Delta_{\text{CT}}$ ), all the cuprate superconductors are doped charge transfer insulators.

### 2.2.3 Gap structure

One of the most important approaches for inferring the origin of superconductivity is the pairing order parameter [50]. The investigation on the superconducting gap structure is very effective in predicting the pairing order parameters. In the previous studies, the cuprate superconductors have been verified to have a  $d$ -wave symmetry [51]. According to the BCS theory, twice the superconducting gap ( $2\Delta_{\text{SC}}$ ) is equal to the energy required to separate one Cooper pair. The superconducting gap  $\Delta_{\text{SC}}$  is an important characteristic of the superconductors. It is related to the critical temperature ( $T_c$ ) of the superconductors as expressed by  $\Delta_{\text{SC}} = 1.76 T_c$  based on the BCS Theory. Angle-resolved photoemission spectroscopy (ARPES) [52, 53] can detect the spectrum of dispersion to determine the size of the superconducting gap. The principle of ARPES will be introduced in chapter 3.

Nodal structure in the superconducting gap was discovered in the cuprate superconductors (e.g.,  $\text{Bi}_2\text{Sr}_2\text{CaCu}_2\text{O}_{8+x}$ ), as illustrated in Fig. 2.5(a) [54]. The structure of the superconducting gap  $\Delta$  corresponds to the  $d$ -wave gap, the size of  $|\Delta|$  reduces to zero when the Fermi surface angle is around  $45^\circ$ . In other words, the node is along the  $(0, 0) - (\pi, \pi)$  direction on the Fermi surface, which demonstrates that the pairing mechanism in the cuprate superconductors is  $d$ -wave symmetry [51]. When the temperature is above  $T_c$  (the normal state), the pseudogap is opening in the

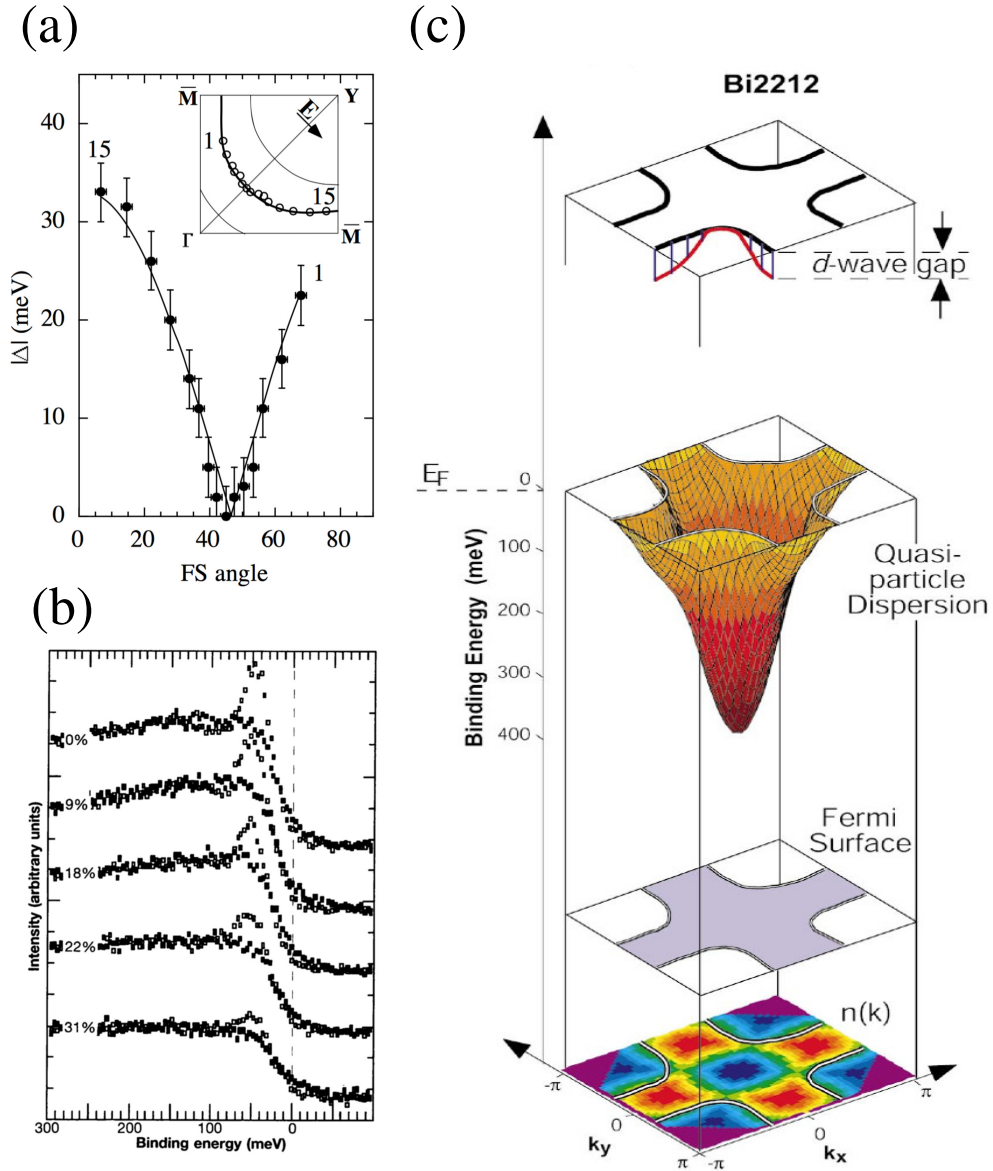


Figure 2.5: (a) The superconducting gap of  $\text{Bi}_2\text{Sr}_2\text{CaCu}_2\text{O}_{8+x}$  (Bi2212) in  $d$ -wave symmetry; node appears in the diagonal region of the Fermi surface (FS) [54]; (b) energy distribution curves (EDCs) over (real squares) and below (hollow squares)  $T_c$  of  $\text{Bi}_2\text{Sr}_2\text{CaCu}_2\text{O}_{8+x}$  along the  $(\pi, 0) - (\pi, \pi)$  (antinodal) direction with different dopant concentration  $x$ ; superconducting gap ( $T > T_c$ ) and pseudogap ( $T < T_c$ ) structures appear below the Fermi level [55]; (c) Fermi surfaces, quasi particle dispersion, and  $d$ -wave pseudogap of overdoped  $\text{Bi}_2\text{Sr}_2\text{CaCu}_2\text{O}_{8+x}$  (Bi2212) from the bottom to the top, respectively [56].

antinodal region as shown in Fig. 2.5(b) [55]. In the superconducting state ( $T < T_c$ ), the energy distribution curves (EDCs) have a structure with sharp shoulder, which is a quasiparticle peak; while a gap structure with no shoulder (pseudogap) appears below the Fermi level when  $T > T_c$ , as shown in Fig. 2.5(b) [55]. Figure 2.5(c) shows an integrated graph of Fermi surface, quasi-particle dispersion, and gap structure of overdoped  $\text{Bi}_2\text{Sr}_2\text{CaCu}_2\text{O}_{8+x}$  [56]. The physical properties of the pseudogap can be investigated by ARPES, scanning tunneling microscope (STM) measurements and so on; preformed Cooper pairs was also suggested by theoretical works [9]; however, the origin of the pseudogap still remains unrevealed.

### 2.2.4 Phase diagram

Phase diagram of hole-doped and electron-doped high  $T_c$  cuprate superconductors exhibits asymmetry, as shown in Fig. 2.6 [56]. The left half is the phase diagram of one typical electron-doped high  $T_c$  superconductor  $\text{Nd}_{2-x}\text{Ce}_x\text{CuO}_4$ , while the right half gives a representative hole-doped material  $\text{La}_{2-x}\text{Sr}_x\text{CuO}_4$ . Antiferromagnetic (AFM) order appears in the parent compound and low doping regions. Neel temperature  $T_N$  decreases with the increasing of the dopant concentration until the superconducting phase appears or the AFM order disappears. In addition, the pseudogap region appears in a triangular region, varying with the dopant concentration and temperature.

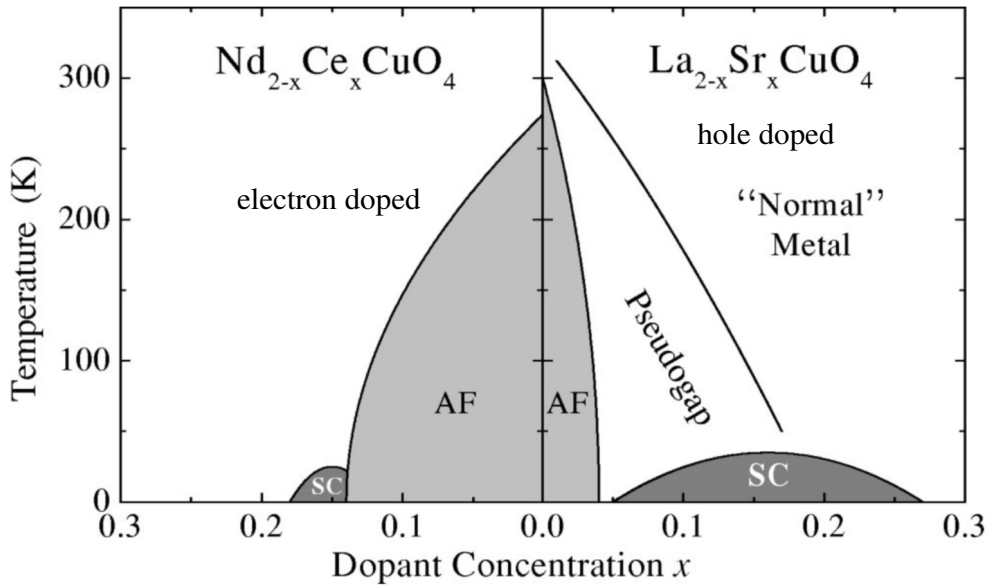


Figure 2.6: Phase diagram of the the cuprate superconductors, including the electron doped ones like  $\text{Nd}_{2-x}\text{Ce}_x\text{CuO}_4$  and hole doped ones like  $\text{La}_{2-x}\text{Sr}_x\text{CuO}_4$  [56].



clamped between two La-O layers; the former one acts as superconductive layer and hence is the focus of theoretical research. Notice is taken that although iron-based superconductors have similar layered structure (superconductive layer) as cuprate superconductors, they are different from the cuprate superconductors in essence. For example, Cu and O atoms are in the same plane, and As atoms are located out of the Fe layer; resulting in the 2D and quasi 3D band structures of cuprate and iron-based superconductors, respectively. The distance between As layer and Fe layer has great influence on the band structure [60].

So far, the iron-based superconductors include a series of well-known materials; e.g., LaFeAsP in 1111 system (ZrCuSiAs-like structure) [26], LiFeAs in 111 system (Cu<sub>2</sub>Sb-like structure) [24], BaFe<sub>2</sub>As<sub>2</sub> in 122 system (ThCr<sub>2</sub>Si<sub>2</sub>-like structure) [30], FeSe in 11 system (i.e., the edge-shared tetrahedrons accumulated along *c* axis) [23], and so on. Therefore, it is available in testing and comprehending the physical mechanism for superconductivity in high  $T_c$  superconductors.

All the iron-based superconductors have conducting layers, which are consisted of iron and pnictogens or chalcogens, such as LaOFeAs [20] and FeSe [61] shown in Fig. 2.8. The iron-pnictide or iron-chalcogen layers play an important role in the iron-based superconductors, like the CuO<sub>2</sub> planes in the cuprate superconductors. The iron-pnictide or iron-chalcogen layers are quasi-2-dimensional with pnictides or chalcogens locate over and below irons plane, while Cu-O layer is 2-dimensional.

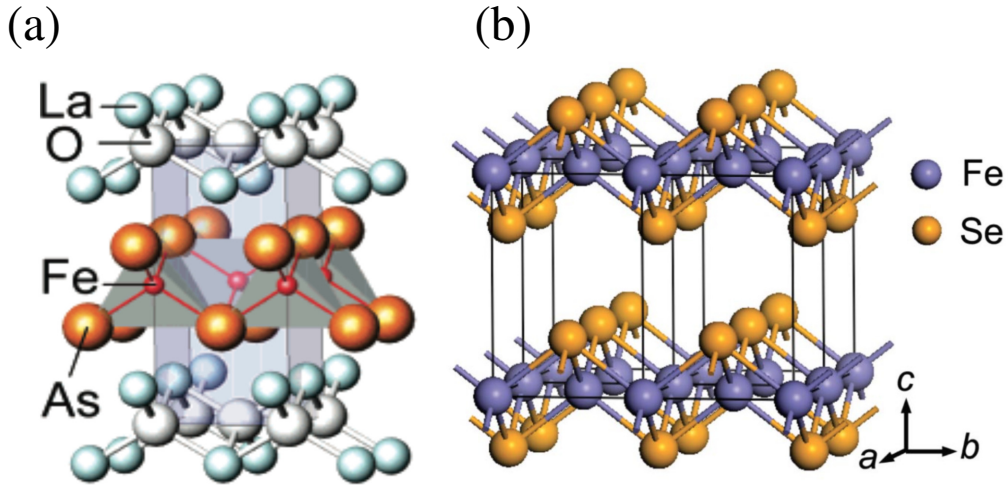


Figure 2.8: Crystal structure of (a) LaOFeAs [20] and (b) FeSe [61].

The electronic structure near Fermi level is mainly contributed by Fe *d* orbitals. Schematic diagram of the iron-pnictide layer is shown in Fig. 2.9(a). Pnictides form the so-called two-iron unite cell. The first Brillouin zone is shown in Fig. 2.9(b). Iron-based superconductors have complex structure on the Fermi surface.

For example, single-layered FeSe only consists of the electron-like Fermi surface sheets around the corner  $(\pi, \pi)$  of the folded Fermi surface; while (Tl, Rb) doped FeSe consists of the electron-like Fermi surface sheets around both center and  $(\pi, \pi)$  [62]. In addition, the Fermi surface of 122 systems like  $\text{BaFe}_2(\text{As}_{1-x}\text{P}_x)_2$  [63] and the 1111 systems like LaFeAsO [60] consists of three hole-like Fermi surface sheets around the Brillouin zone center and two electron-like Fermi surface sheets around the corner of the folded Brillouin zone.

### 2.3.2 Orbital character of energy bands

The band structure can be calculated by the local density approximation (LDA) as illustrated in Fig. 2.10 [68] and Fig. 2.20(I) [67]. Apart from theoretical predictions, experimental verifications are even more crucial. Zhang *et al.* investigated the orbital characters of bands in  $\text{BaFe}_{1.85}\text{Co}_{0.15}\text{As}_2$  by ARPES using  $p$  and  $s$  linearly polarized light, as shown in Fig. 2.11(c) [69].

They analyzed the orbital characters of bands by the relationship between light polarization and spatial symmetry of  $3d$  orbitals, which could be inferred from the electric dipole approximation and selection rules, as we will introduce in section 4.1. The orbital characters of bands were illustrated in Fig. 2.11(d), in which the Brillouin zone (BZ) and coordinate  $x, y, z$  were defined in Fig. 2.11(a)-(c). We have taken into account the fact that the cut plane for the electron pockets is tilted by a non-negligible angle. Taking the 122 type iron-based superconductors as an example, the angle at the centre of the electron pockets is about 22 degree for  $h\nu = 40$  eV, and 36.5 degree for  $h\nu = 18$  eV. Moreover, detailed numerical calculation of the spectral weight is necessary, which will be presented in section 4.2.

There are some contradictions between the theoretical and the experimental researches. In the iron-based superconductors the orbital characters on the inner electron pockets, the experimental result were the same as the theoretical result, while the outer electron pockets are not. We will discuss this problem in detail in section 4.2.

### 2.3.3 Phase diagram

The Phase diagrams of hole-doped, electron-doped, and isovalent-doped 122 type iron-based high  $T_c$  superconductors exhibits similar behaviors [27–29], as shown in Fig. 2.12. The superconducting phase appears in certain stoichiometric regions; while the antiferromagnetic (AFM) order appears in the parent compound and the low doping regions in the iron pnictide. The AFM order vanishes when temperature exceeds the Neel temperature  $T_N$ , which slowly decreases with increasing dopant concentration. Different from the cuprate ones, crystal structure phase transition (tetragonal-to-orthorhombic phase transition) occurs in the iron-based pnictides at

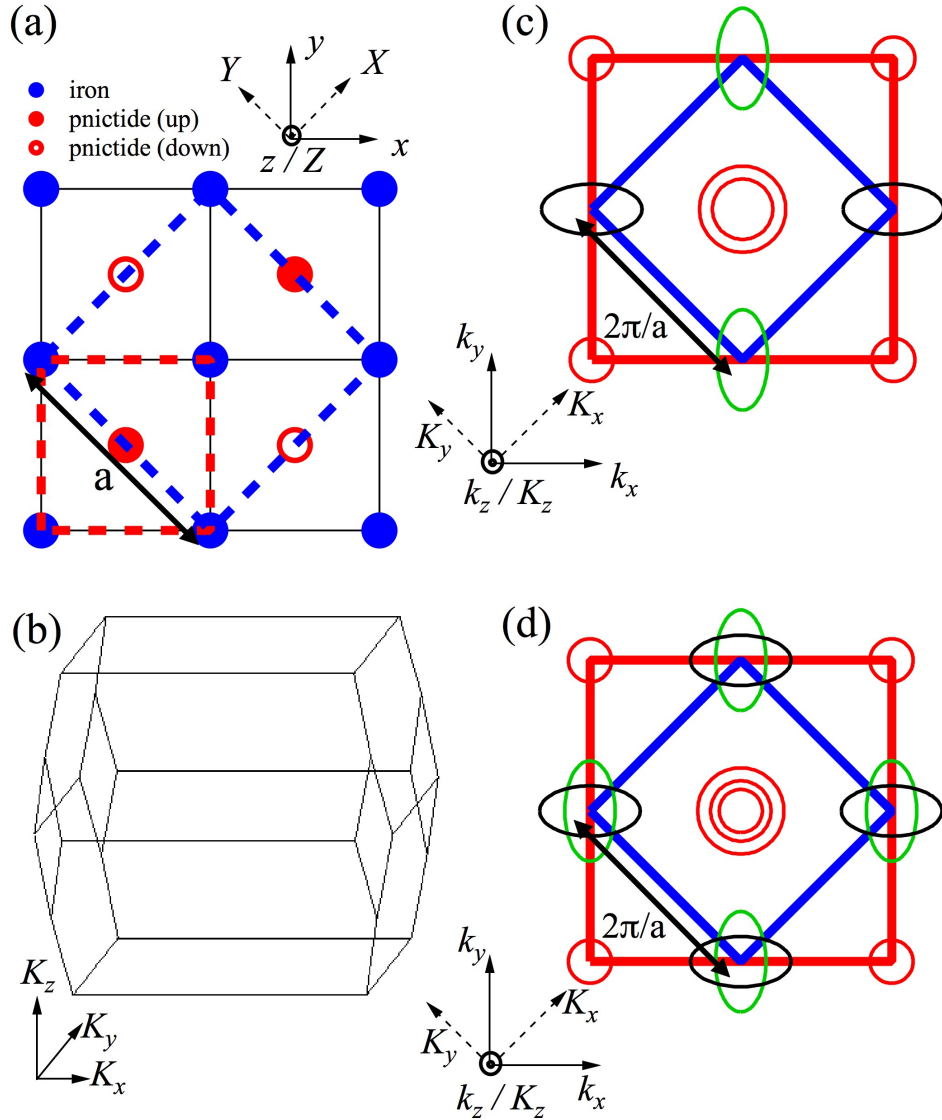


Figure 2.9: (a) Schematic drawing of the iron-pnictide layers; dashed red and blue squares denote the unit cell containing one and two iron atoms; blue solid circles are iron atoms, red real and hollow circles are pnictides over and below the iron planes, respectively; (b) first Brillouin zone of two-iron unit cell; (c) and (d) schematically show the unfolded (solid red lines) [64] and folded (solid blue lines) [65] Brillouin zones with hole and electron pockets, corresponding to the unit cell with one and two iron atoms [66, 67].

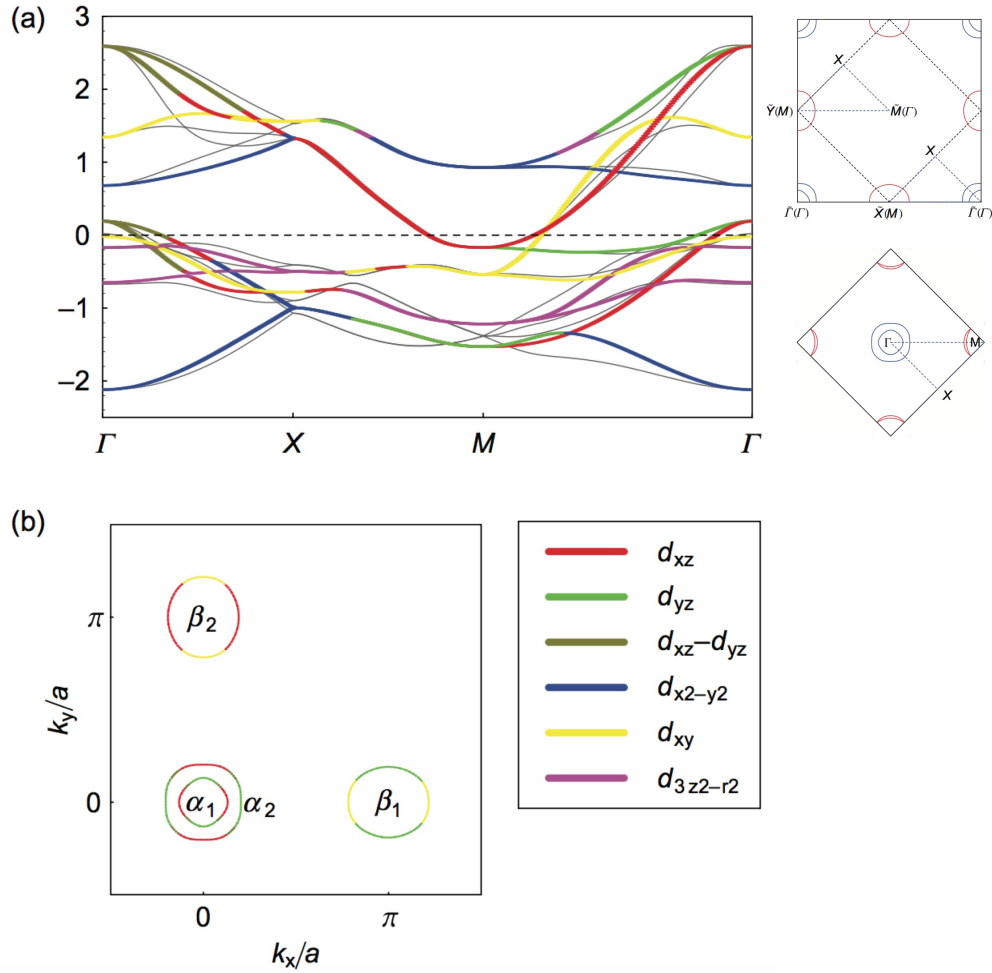


Figure 2.10: Band structure and Fermi surface in folded (a) and unfolded (b) Brillouin zone of the five-band model;  $\Gamma$ , X, and M are the symmetry points in the Brillouin zone; the red, green, yellow, blue, magenta, and brown lines denote the  $d_{xz}$ ,  $d_{yz}$ ,  $d_{xy}$ ,  $d_{x^2-y^2}$ ,  $d_{3z^2-r^2}$ , and  $d_{xz} - d_{yz}$  orbitals, respectively [68].

the temperature  $T_s$ , which is slightly higher than  $T_N$ . An electronic nematic phase transition usually accompanies the structural transition in the iron pnictides [70,71]. The AFM phase may coexist with the SC phase in the iron-based superconductors [72], which usually does not happen in the cuprate ones, as illustrated in Fig. 2.6.

The phase diagrams of iron-based superconductors are quite different from and more complex than that of the cuprate ones. For example, the phase diagrams of Co-doped 1111 systems contain the SC phase, the spin-density-wave (SDW) phase, AFM phase and the ferromagnetic (FM) phase, as is shown in Fig. 2.13 [73].  $T_s$  and  $T_N$  in the phase diagram of  $\text{BaFe}_2(\text{As}_{1-x}\text{P}_x)_2$ , as shown in Fig. 2.12(c), are close to each other, suggesting that the spin and orbital fluctuations are comparable

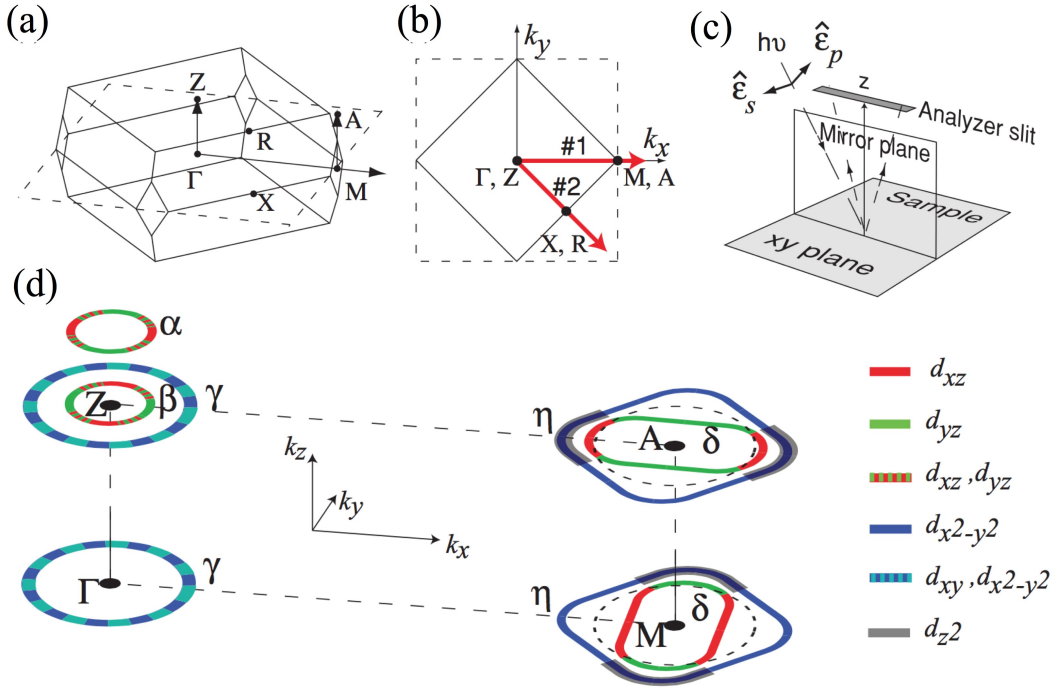


Figure 2.11: (a), (b) Brillouin zone (BZ) of iron-based superconductors; (c) definition of polarized light; and (d) schematic graph of orbital characters of bands on the Fermi surface [69].

around the optimal doping, indicating the possible existence of the spin and orbital fluctuations competition near the optimal doping.

## 2.4 Superconducting gap

The superconducting gap in the iron-based superconductors exhibits complex features; which is quite different from that of the cuprate superconductors. As mentioned in section 2.2, cuprate superconductors have the universal  $d$ -wave pairing symmetry. Thus, systematic investigation of the superconducting gap turns out to be important. To date, a large amount of experimental and theoretical works on the gap symmetry have been carried out, as described in the following.

### 2.4.1 Experimental studies

In the experimental studies of 1111 systems, the appearance of nodeless gap was reported in  $\text{PrFeAsO}_{1-y}$  [74],  $\text{LaFeAsPO}_{0.7}$  [75] and so on, yet a line nodal gap was also found in  $\text{LaOFeP}$  [76–78]. In the 122 systems, a nodeless gap appeared in the optimally doped  $\text{Ba}_{1-x}\text{K}_x\text{Fe}_2\text{As}_2$  (hole doping) [79] and in a wide range of

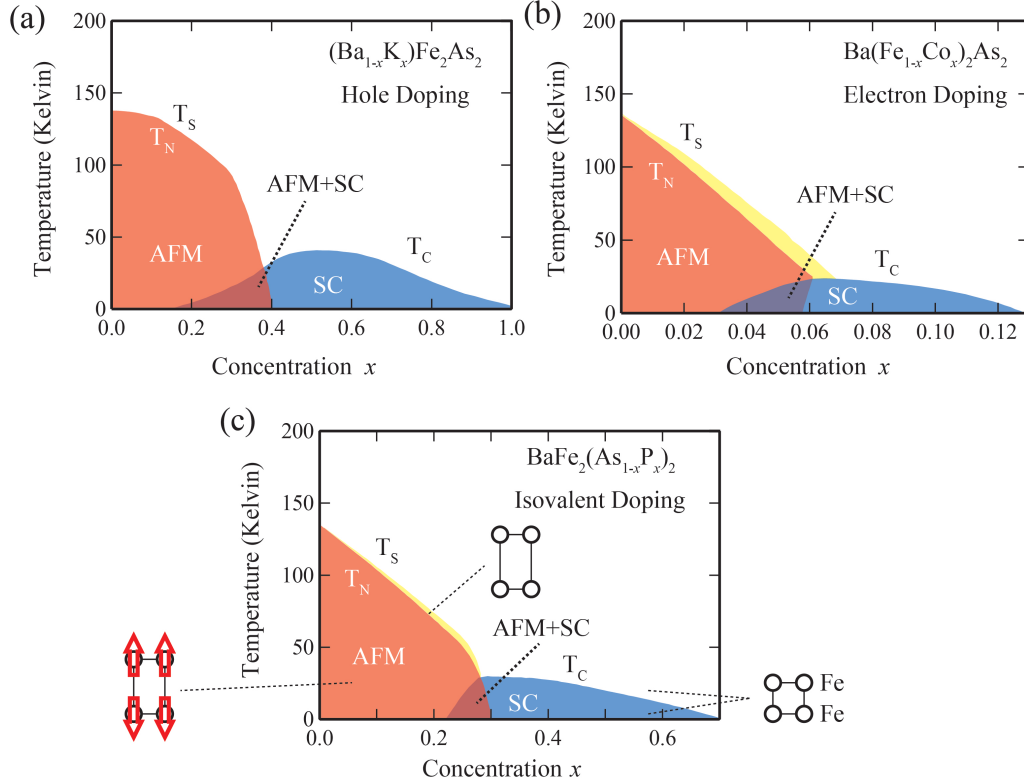


Figure 2.12: Phase diagram of the hole-doped [27], electron-doped [28], and isovalent-doped [29] 122 type iron-based superconductors.

Co doping in  $\text{Ba}(\text{Fe}_{1-x}\text{Co}_x)_2\text{As}_2$  (electron doping) [80]; while the nodal gap was reported in the isovalently-doped  $\text{BaFe}_2(\text{As}_{1-x}\text{P}_x)_2$  [81, 82] and  $\text{Ba}(\text{Fe}_{1-x}\text{Ru}_x)_2\text{As}_2$  [82], hole-doped  $\text{Ba}_{0.6}\text{K}_{0.4}\text{Fe}_2\text{As}_2$  [83], and  $\text{KFe}_2\text{As}_2$  [84, 85].

A nodal structure with fourfold symmetry in the superconducting gap was suggested in the isovalent-doped iron-based superconductor  $\text{BaFe}_2(\text{As}_{1-x}\text{P}_x)_2$  by angle-resolved thermal conductivity measurements in a magnetic field (Fig. 2.14), and closed-loop line nodes in the flat part of electron pocket was also suggested, as shown in Fig. 2.15 [86].

However, contradictory results were reported by several ARPES experiments [79, 87, 88], as shown in Fig. 2.16 in  $\text{BaFe}_2(\text{As}_{1-x}\text{P}_x)_2$ .

Full superconducting gap on the hole Fermi surfaces (FSs) in  $\text{BaFe}_2(\text{As}_{1-x}\text{P}_x)_2$  ( $x = 0.35$ ) has been observed by laser ARPES measurements ( $h\nu = 7$  eV) [79]. Zhang *et al.* [87] have observed a horizontal superconducting gap node on the outer hole Fermi surface around  $Z$  point and isotropic superconducting gaps on electron Fermi surfaces by ARPES measurements in optimally doped  $\text{BaFe}_2(\text{As}_{1-x}\text{P}_x)_2$  ( $x = 0.3$ ). However, Yoshida *et al.* [88] suggested no horizontal superconducting gap node on the hole Fermi surfaces and anisotropic superconducting gaps on the outer

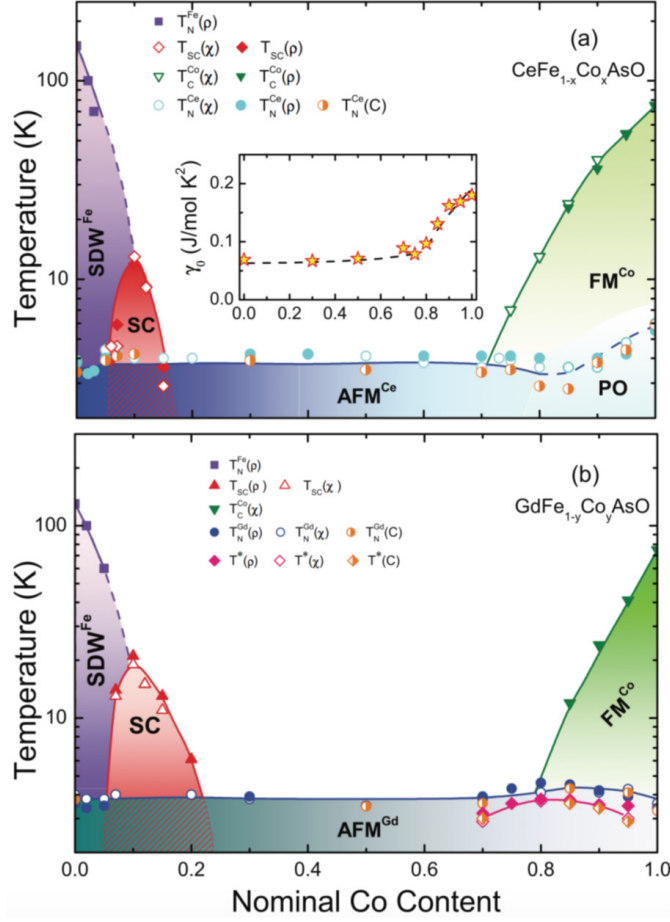


Figure 2.13: Phase diagram of the 1111-type iron-based superconductors  $\text{CeFe}_{1-x}\text{Co}_x\text{AsO}$  and  $\text{GdFe}_{1-y}\text{Co}_y\text{AsO}$  [73].

electron Fermi surface by ARPES measurements in the same doping composition, which agreed with the angle-resolved thermal conductivity measurements [86].

Although Shimojima *et al.* [79] considered that the spectrum using photons of  $h\nu = 7$  eV is around the  $Z$  point ( $k_z = \pi$ ) in the Brillouin zone in  $\text{BaFe}_2(\text{As}_{1-x}\text{P}_x)_2$  ( $x = 0.35$ ), our Fermi surface mapping in the  $k_{\parallel}-k_z$  plane (Fig. 5.1), which crosses the  $\Gamma$  and  $X$  points in the folded Brillouin zone, shows that  $h\nu = 7$  eV is a little far away from the  $Z$  point. The range of Fermi surface angle ( $\theta_{\text{FS}}$ ) on the outer hole Fermi surface is narrow ( $-20^\circ \sim 20^\circ$ ); and therefore they did not measure the crucial angles ( $\theta_{\text{FS}} = 45^\circ$  or its fourfold symmetric angles around the  $Z$  point), which is along the  $\Gamma$ - $X$  direction. The related information shall be mentioned in section 2.4.2.

It is also controversial about the line nodes in the superconducting gap as suggested by Zhang *et al.* [87]. For example, the gap symmetry reported by Zhang

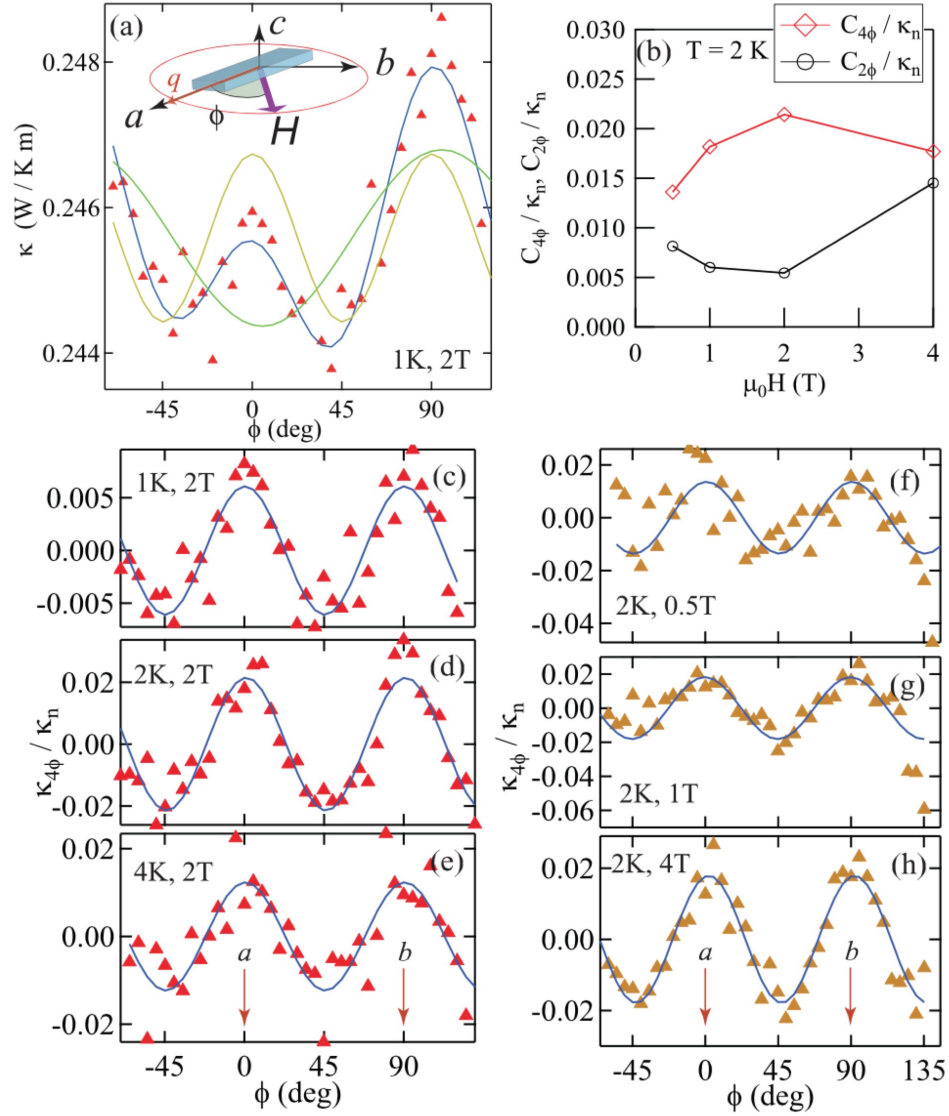


Figure 2.14: (a) Angular variation of the thermal conductivity  $\kappa$  in  $\text{BaFe}_2(\text{As}_{1-x}\text{P}_x)_2$  ( $x = 0.33$ ); (b) magnitudes of twofold ( $\kappa_{2\phi}$ ) and fourfold ( $\kappa_{4\phi}$ ) symmetry of  $\kappa$ ; (c)-(h)  $\kappa_{4\phi}$  under different conditions [86].

*et al.* does not show the four-fold symmetry reported by the thermal conductivity measurements [86]. Because the sharp superconducting gaps were not observed, as shown in Fig. 2.16(III.a), it is difficult to make definite conclusion on the existence of horizontal superconducting gap node definitely. Besides, the range of  $\theta_{\text{FSS}}$  on the electron Fermi surfaces are also narrow; therefore it is also difficult to conclude whether the gaps on the electron Fermi surfaces are isotropic or not.

Superconducting gaps with no line nodes were observed around the  $Z$  ( $h\nu =$

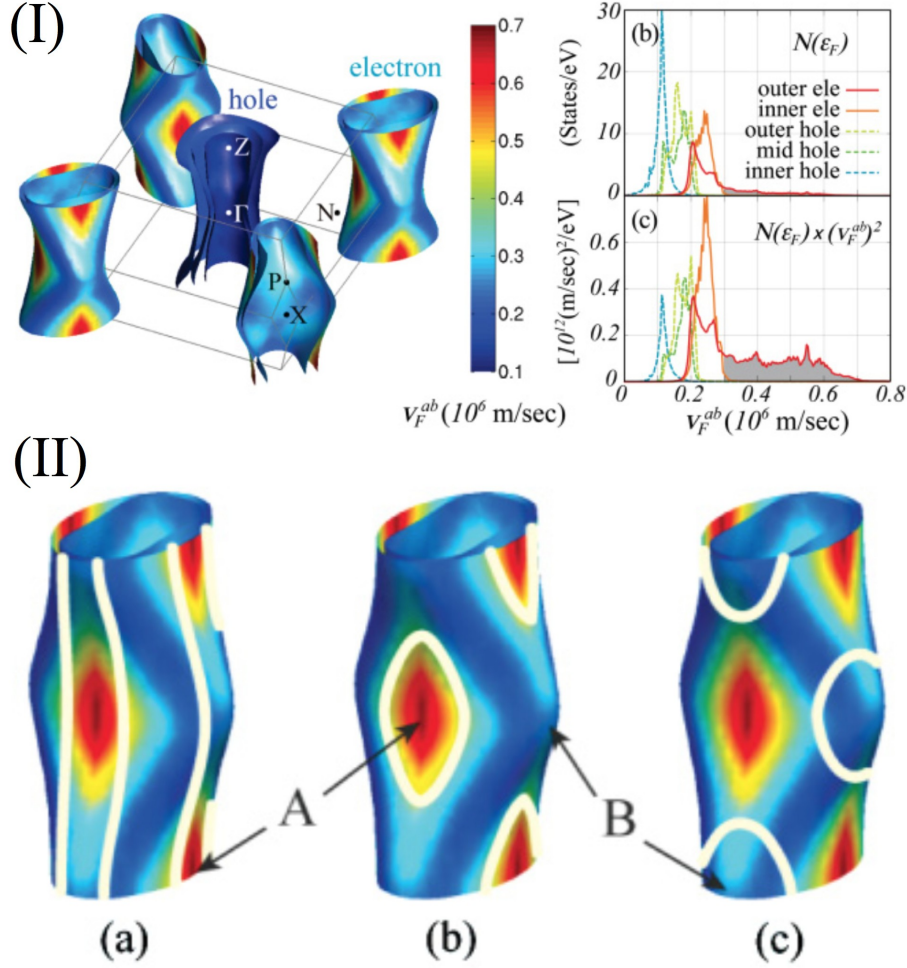


Figure 2.15: (I.a) Fermi surface of  $\text{BaFe}_2(\text{As}_{1-x}\text{P}_x)_2$  ( $x = 0.33$ ), (I.b), (I.c) The density of state (DOS),  $N(\epsilon_F)$  and  $N(\epsilon_F) \times v_F^{ab}$ ; (II.a), (II.b) and (II.c) several kinds of closed-loop line nodes structure drawn by white line, and only (II.b) is suggested [86].

35 eV) point, which is exactly opposite to the result from Zhang *et al.*, as shown in Fig. 2.16(II.a). In addition, from low photon energies to high photon energies the superconducting gaps also exhibited a contrary trend of  $\alpha$  band (Fig. 2.16(II.c), marked by red points) to Zhang *et al.*'s study (Fig. 2.16(III.b) marked by green points). Notice is taken that there are subtle differences between the Fermi surface mapping in the  $k_{\parallel}$ - $k_z$  plane given by the results of Zhang *et al.* [87] and Yoshida *et al.* [88]. The symmetrized cuts including the  $Z$  point, as shown in Fig. 2.16(II.a) and Fig. 2.16(III.a), gave two and three bands, respectively. In fact, cuts crossing the  $\Gamma$  point (not shown here) also presented different numbers of bands [87, 88].

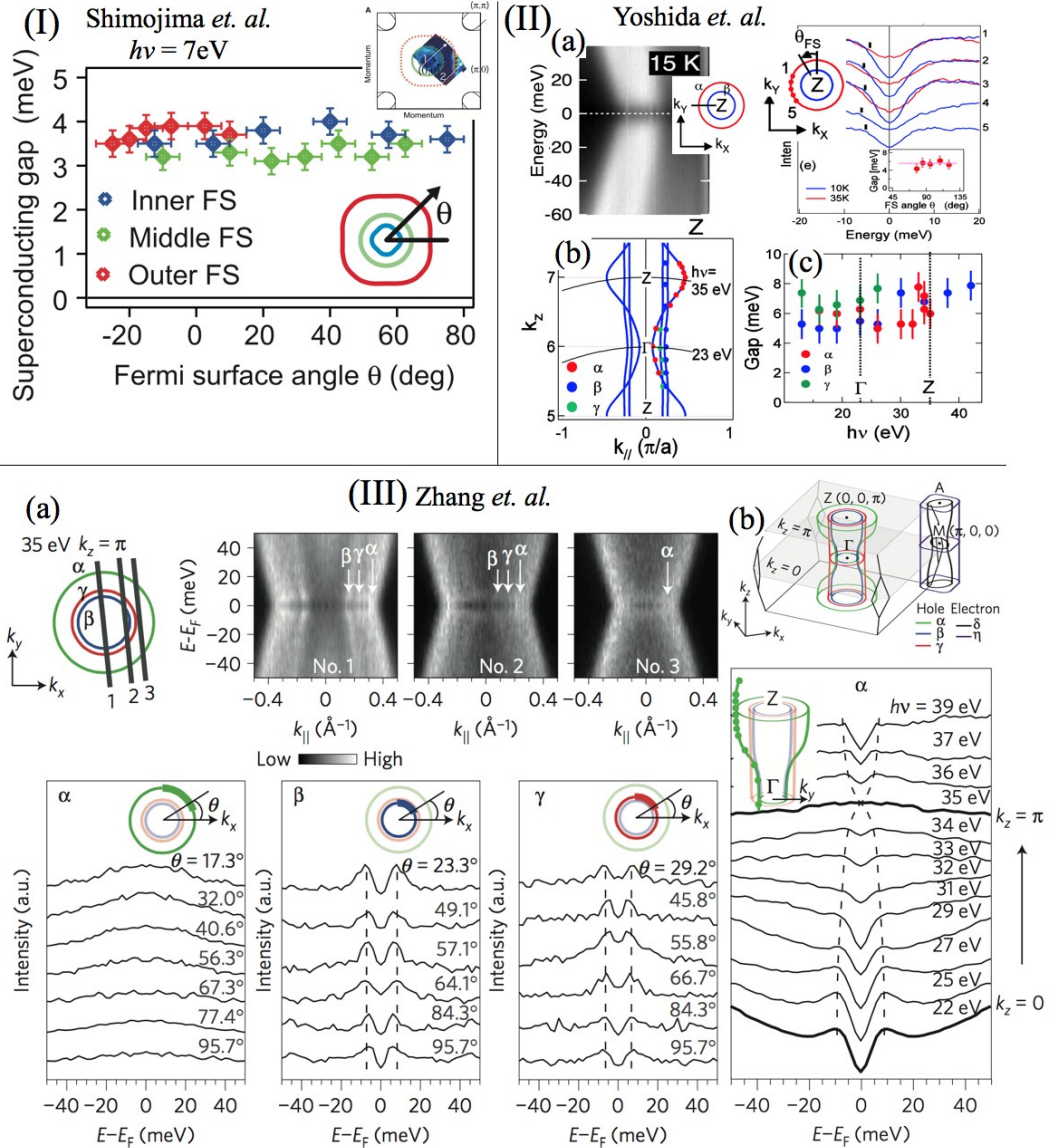


Figure 2.16: Superconducting gap (I) around the  $Z$  point ( $h\nu = 7\text{ eV}$ ) [79]; (II.a) around the  $Z$  point ( $h\nu = 35\text{ eV}$ ) and (II.b)-(II.c) with various  $k_z$  [88]; (III.a) around the  $Z$  point ( $h\nu = 35\text{ eV}$ ) and (III.b) with various  $k_z$  [87] on the hole Fermi surfaces in the  $\text{BaFe}_2(\text{As}_{1-x}\text{P}_x)_2$  measured by ARPES. Fermi surface angles ( $\theta_{\text{FS}}$ ) are defined as illustrated. Note that the definition of the Fermi surface angle in (I) is different from the other two.

These numerous experimental results on the nodal or nodeless gap exhibit no systematic tendency, suggesting that the gap of the iron-based superconductors cannot be simply described by one unified model. Hence, several theoretical models were suggested, which will be introduced in the following section.

### 2.4.2 Theoretical studies

Various potential mechanisms, such as external pressure [89], height of pnictogen [60], spin- and orbital-fluctuations [67], were suggested to explain the complexity of the structure of gap nodes in the iron-based superconductors.

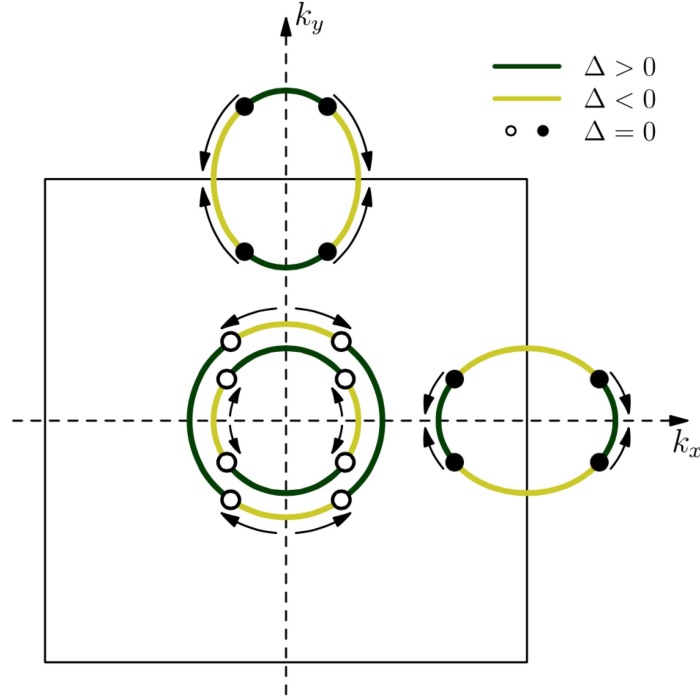


Figure 2.17: Sketch of the shift in gap nodes under the uniaxial strain along  $x$  direction [89].

Employing a five-orbital Hubbard model, the structure of gap nodes tuned by the uniaxial strain was obtained, as illustrated in Fig. 2.17 [89]. Using the five-band Hubbard model and combining with random phase approximation (RPA), Kuroki *et al.* have shown that the effect of pnictogen height on the spin-fluctuation brought about the nodal or nodeless superconducting gap in the 1111 systems, such as LaFeAsO [75], NdFeAsO [21, 90], and LaFePO [91, 92]. This relationship can be observed in the phase diagram of pnictogen height versus lattice constants, in which the nodeless (high- $T_c$ ) and nodal (low- $T_c$ ) regions are separated, as shown in Fig. 2.18 [60].

When we compare the crystal structure of LaFeAsO [20] with that of LaFePO [93] (increased chemical pressure by P dopant), or compare the optimally doped NdFeAsO $_{1-y}$  with NdFeAsO $_{1-y}$  under pressure, it is obvious that the symmetry of superconducting gap is sensitive to the crystal structure. Considering that the

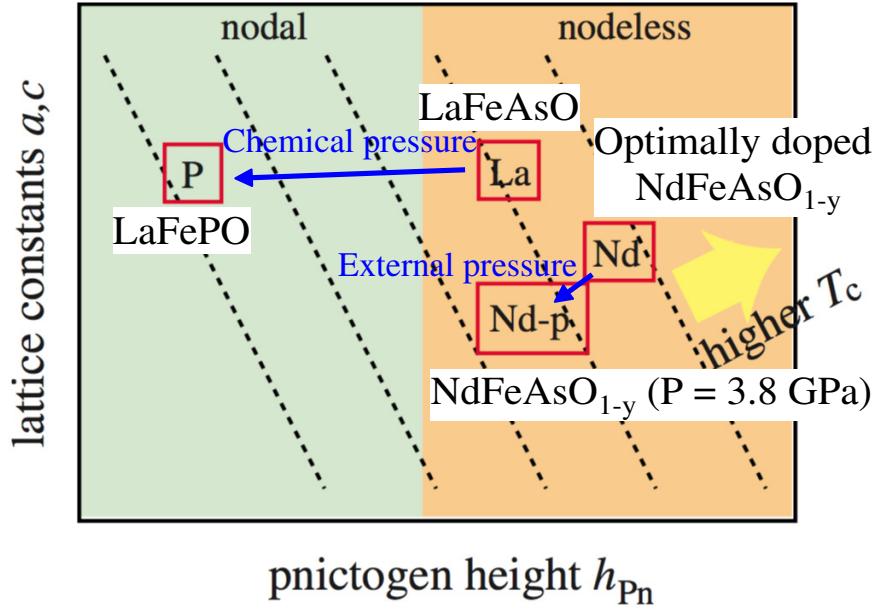


Figure 2.18: Schematic graph of the phase diagram on  $h_{Pn} - [a, c]$ , in which, La is LaFeAsO, Nd is optimally doped NdFeAsO<sub>1-y</sub>, Nd-p is NdFeAsO<sub>1-y</sub> under the pressure of 3.8 GPa, and P is LaFePO, respectively [60].

chemical pressure on LaFeAsO (by P doping) changes the lattice parameters  $a$  and  $c$  only by 2-3% while the pnictogen height changes by about 15%, the switch between nodeless and nodal gap structure in LaFeAsO and LaFeAsP may come from the change of pnictogen height. In other words, it can be concluded that the superconducting gap symmetry is sensitive to the pnictogen height. As a result, applying either external pressure or chemical pressure without charge dopant can probably change the properties of the high  $T_c$  iron-based superconductors, which shows great consistency with the experiments [75–78].

In the 1111 systems, the transition temperature  $T_c$  of LaFePO (node,  $T_c = 5$  K [93]) is much lower than that of LaFeAsO (nodeless,  $T_c = 26$  K [20]), while  $T_c$  is not lower in the 122 system BaFe<sub>2</sub>(As<sub>1-x</sub>P<sub>x</sub>)<sub>2</sub>, which also has a nodal gap [81]. It seems that the appearance of nodal gap does not significantly affect the  $T_c$  of BaFe<sub>2</sub>(As<sub>1-x</sub>P<sub>x</sub>)<sub>2</sub>, which is quite different from the situation in 1111 systems. Spin fluctuation was suggested as the origin of the line nodes in the 1111 systems [60], while the competition between spin and orbital fluctuations was proposed as the origin of the gap in the 122 systems [94, 95].

In addition, Suzuki *et al.* [63] calculated the structure of superconducting gap of BaFe<sub>2</sub>(As<sub>1-x</sub>P<sub>x</sub>)<sub>2</sub> by using the ten-orbital model and RPA under the spin-fluctuation-mediated pairing mechanism, suggesting a  $s_{\pm}$  superconducting gap with

nodal gap on the  $Z^2/XZ/YZ$  ( $X, Y, Z$  refer to the folded unit cell as shown in Fig. 2.9) hole Fermi surfaces around the  $Z$  points, and nodeless gap on the electron pockets, as shown in Fig. 2.19 [63].

On the other hand, Saito *et al.* [67] also calculated the superconducting gap of  $\text{BaFe}_2(\text{As}_{1-x}\text{P}_x)_2$  using the ten-orbital Hubbard model through changing the parameters, the appearance of anisotropy or even the line nodes could be observed. Line nodes appears or vanishes on the hole Fermi surfaces depending on the competition between spin and orbital fluctuations, as shown in Figs. 2.21(c) and 2.22(c) [67].

In Figs. 2.20-2.24,  $x, y,$  and  $z$  refer to the unfolded unit cell, as shown in Fig. 2.9; the relationship of colour lines and orbitals is shown in Figs. 2.21;  $U$  (in eV) is the Coulomb interaction; and  $g$  (in eV) is the quadrupole interaction reflecting the orbital polarization, respectively. The quadrupole interaction comes from the electron-phonon interaction of the iron ion oscillations, which was demonstrated by the shear modulus softening experiments [70, 96, 97], as expressed by [98]

$$V_{\text{quad}} = -g_1(\omega_l) \sum_i^{\text{site}} (\hat{O}_{yz}^i \cdot \hat{O}_{yz}^i + \hat{O}_{xz}^i \cdot \hat{O}_{xz}^i) - g_2(\omega_l) \sum_i^{\text{site}} (\hat{O}_{xy}^i \cdot \hat{O}_{xy}^i), \quad (2.3)$$

where  $\hat{O}_{\text{orbit}}^i$  is the quadrupole operator.

Assumption was made that  $g_1 = g_2 = g$  in Figs. 2.21-2.23, while  $g_1 = g$  and  $g_2 = 0$  in Fig. 2.24. Focusing on Fig. 2.9(V.i)-(V.iii), the symmetry of the superconducting gap changed dramatically by slightly tuning the parameters, in which the quadrupole interaction term was fixed and only the Coulomb interaction  $U$  was varied slightly. The value of pairing order parameter  $\Delta$  became negative when increasing the spin-fluctuation on the electron pockets. By comparing Fig. 2.22 with Fig. 2.24, both of them are about the orbital-fluctuation-mediated pairing mechanism ( $U = 0$ ); the only difference is considering the  $d_{xy}$  orbital-fluctuation (setting  $g_2$  a nonzero value) or neglecting it ( $g_2 = 0$ ), respectively. The superconducting gap size of the  $d_{xy}$  orbital in the outer hole pocket around the  $Z$  point changed a lot by tuning the contribution of the  $d_{xy}$  orbital-fluctuation. The symmetry of the gap was also affected by the impurity concentration ratio  $n_{\text{imp}}$ , as shown in Fig. 2.25.

## 2.5 Physical properties of P doped $\text{BaFe}_2\text{As}_2$

Among plenty of modifications of the parent compound  $\text{BaFe}_2\text{As}_2$  through adding various dopants (hole, electron, isovalent) on one or more of Ba, Fe, and As sites [27–29], phosphorus-doping  $\text{BaFe}_2\text{As}_2$  or  $\text{BaFe}_2(\text{As}_{2-x}\text{P}_x)_2$  has gained particular attention since its first report in 2010 [81]. In this section a brief review of the previous studies on some special properties of P-BaFeAs is performed.

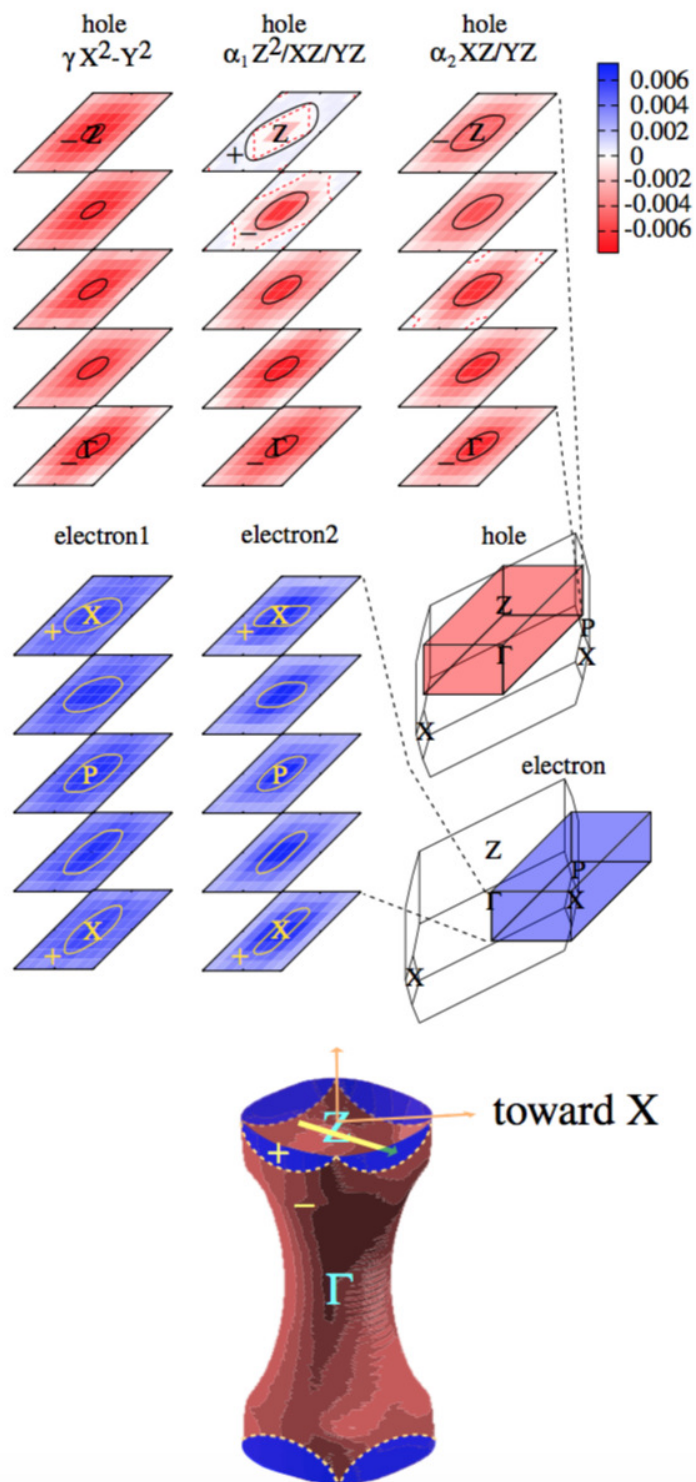


Figure 2.19: Structure of superconducting gap in  $\text{BaFe}_2(\text{As}_{1-x}\text{P}_x)_2$  given by ten-orbital model and random phase approximation (RPA) [63].

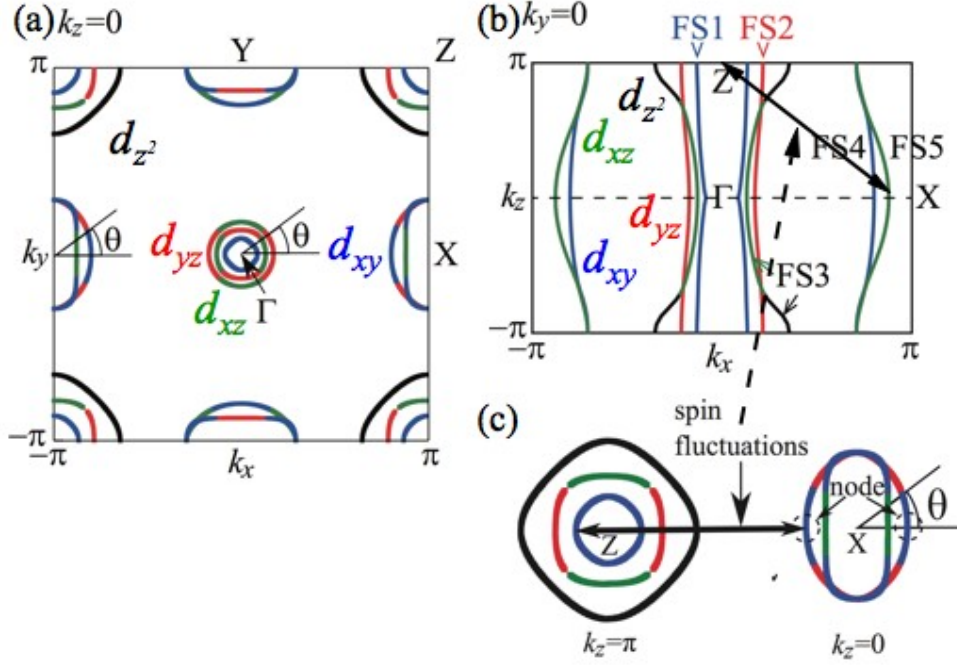


Figure 2.20: The Fermi surfaces of the iron-based superconductors in the (a)  $k_z = 0$  and (b)  $k_y = 0$  plane; (c) sketch of the competition of spin and orbital fluctuations [67].

$\text{BaFe}_2(\text{As}_{1-x}\text{P}_x)_2$  is a multiband superconductor, with five  $3d$  orbitals, the Fermi surfaces of which can be seen in Fig. 2.26. The doping concentration  $x$  of P affects the lattice constant  $a$ ,  $c$ , and pnictogen height, which have an approximate linear decrease [99], as shown in Fig. 2.27(a)-(b).

Hashimoto *et al.* reported a penetration phenomenon in  $\text{BaFe}_2(\text{As}_{1-x}\text{P}_x)_2$  [100]. As illustrated in Fig. 2.28, the quantum critical point appears at  $x = 0.30$ , which is optimally doped and corresponds to maximum critical temperature. The Fermi surface of  $\text{BaFe}_2(\text{As}_{1-x}\text{P}_x)_2$  has in total five quasi-cylindrical pockets in the Brillouin zone, including three hole pockets at the center and two electron pockets at the corner [100]. Figure 2.28(c) shows the dopant concentration-dependence of the squared in-plane London penetration length  $\lambda_L^2(0)$  in the zero-temperature limit. It is found that the concentration denoted by the sharp peak (about  $x = 0.30$ ), and the appearance of QCP at  $x = 0.30$  was believed to be the cause of the  $\lambda_L^2(0)$  peak [100].

It has been proposed that when correlations in one system are significant, its electronic states could become anisotropic, as classified into three phases: liquid phase (breaks no spatial symmetry), nematic phase (breaks four-fold rotation symmetry), and smectic phase (breaks translational symmetry in one direction) [101], as shown in Fig. 2.29.

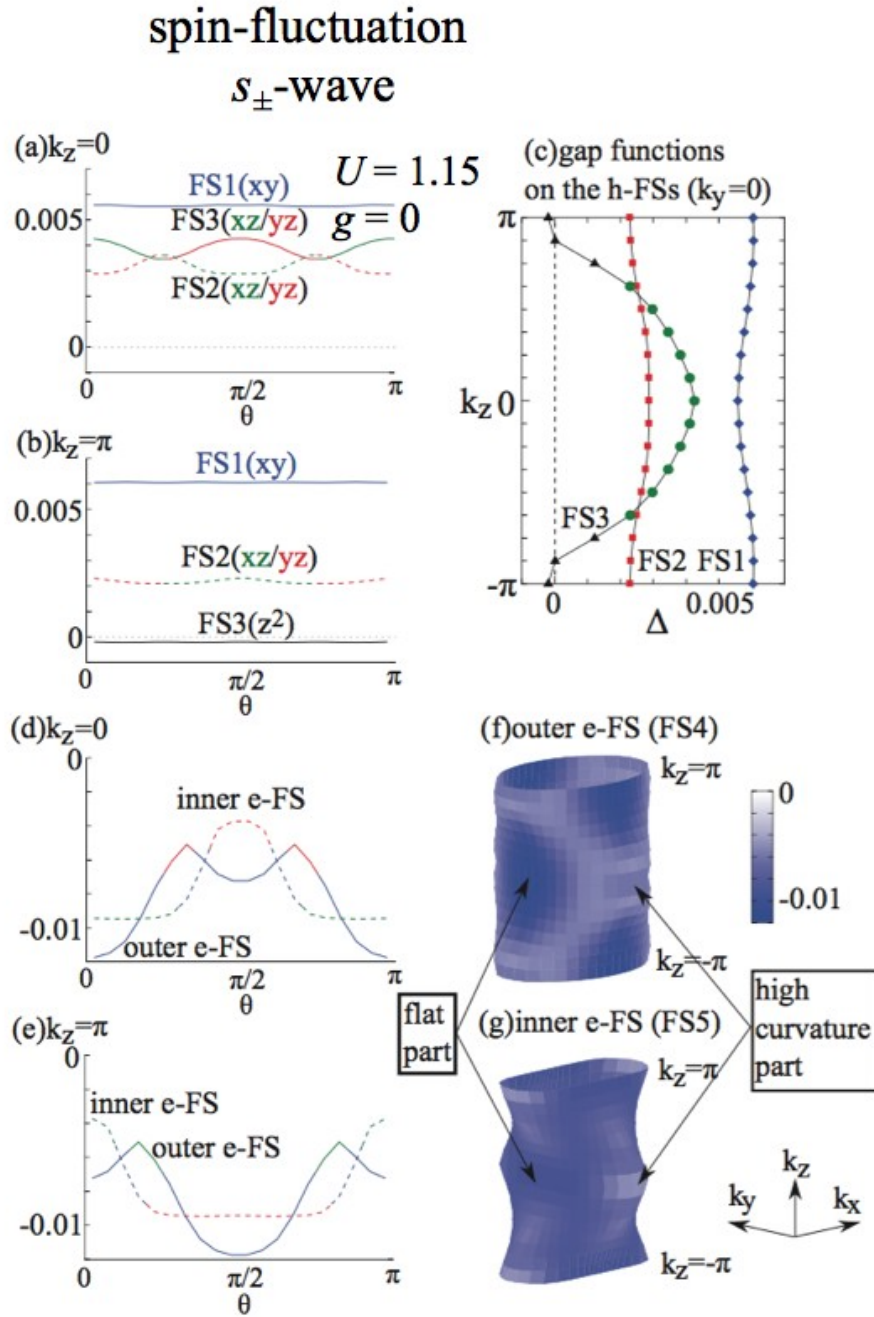


Figure 2.21: Superconducting gap functions in the presence of spin fluctuation pairing mechanism with  $U = 1.15$  and  $g_1 = g_2 = g = 0$  [67].

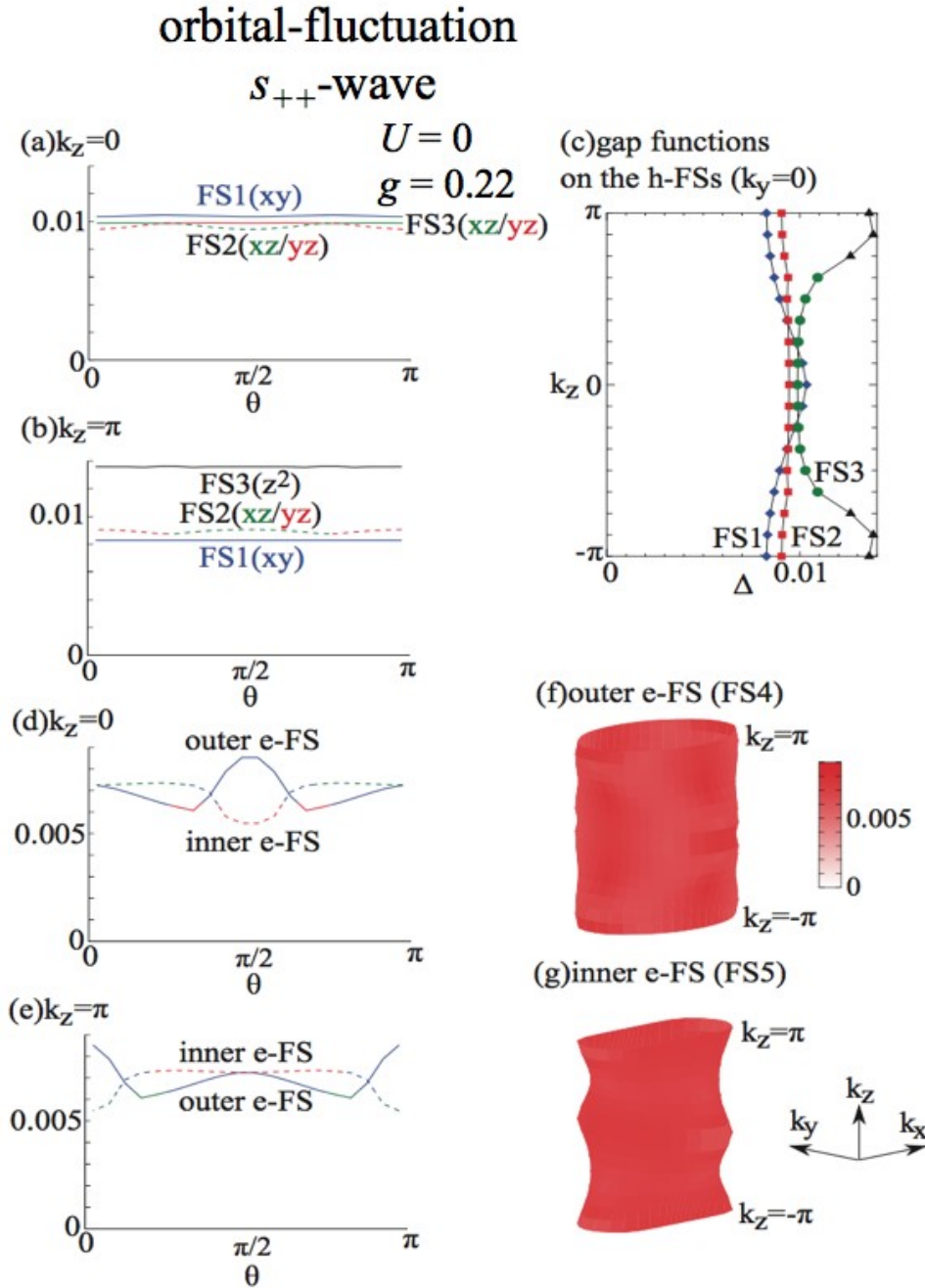


Figure 2.22: Superconducting gap functions in the presence of orbital fluctuation pairing mechanism with  $U = 0$  and  $g_1 = g_2 = g = 0.22$  [67].

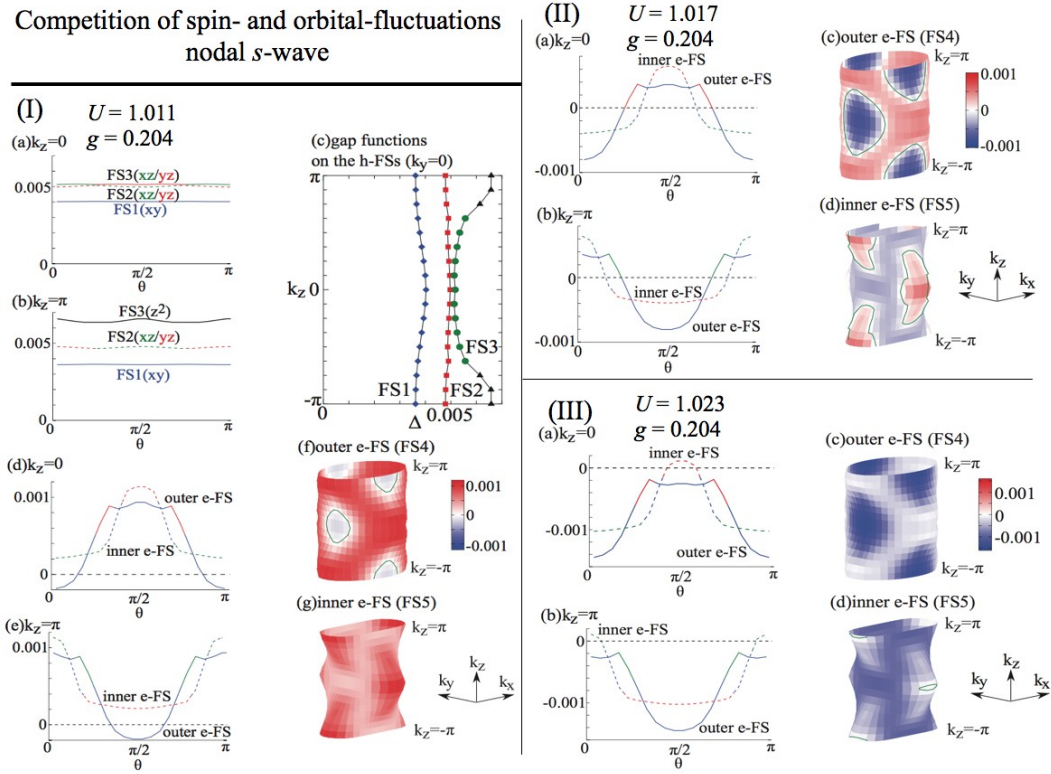
Competition of spin- and orbital-fluctuations  
nodal  $s$ -wave

Figure 2.23: Superconducting gap functions in the presence of competition between spin and orbital fluctuations-mediated pairing mechanism with (I)  $U = 1.011$ , (II)  $U = 1.017$ , (III)  $U = 1.023$ , and  $g_1 = g_2 = g = 0.204$  [67].

An electronic nematic phase was observed by magnetic torque measurements in  $\text{BaFe}_2(\text{As}_{1-x}\text{P}_x)_2$  [71]. In Fig. 2.30(c) there are four phases: antiferromagnetic phase, superconducting phase, nematic phase, and paramagnetic phase [71]. When  $T > T^*$  susceptibility tensor  $\chi$  is tetragonal symmetry; while  $T < T^*$  the nematic phase appears [71]. In Fig. 2.30(d) the torque  $\tau = \mu_0 V \mathbf{M} \times \mathbf{H}$  is a thermodynamic quantity, which is a periodic function of azimuthal angle  $\phi$ .  $\tau$  can be decomposed into two- and four-fold symmetric components. When  $T < T^*$  the two-fold term  $\tau_{2\phi}$  has a nonzero value, indicating the appearance of two-fold rotational symmetry; that is to say in this case the material is in the nematic phase which breaks four-fold rotation symmetry.

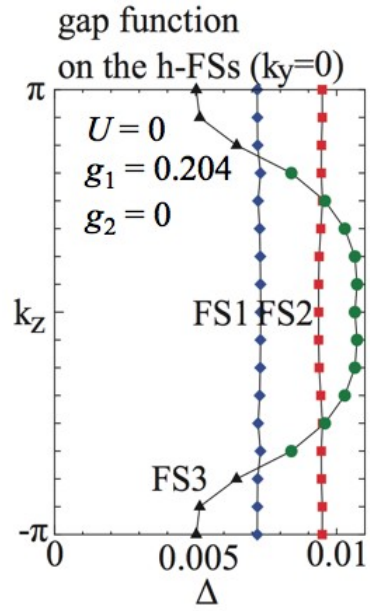


Figure 2.24: Gap functions on the hole Fermi surfaces with  $g_1 = g$ ,  $g_2 = 0$ , and  $U = 0$  [67].

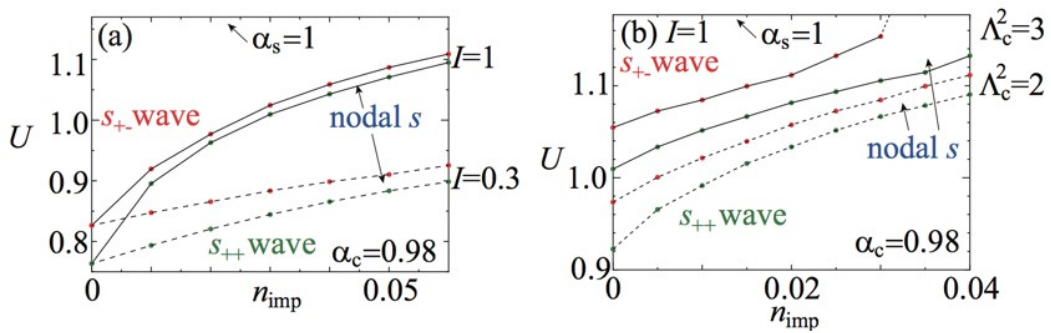


Figure 2.25:  $U$ - $n_{imp}$  phase diagram of pairing mechanism [67].

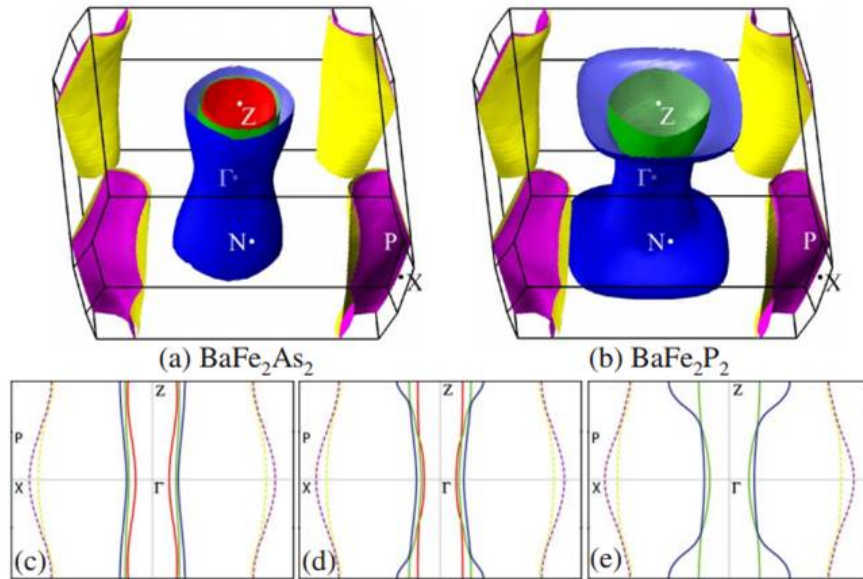


Figure 2.26: Fermi surfaces of (a)  $\text{BaFe}_2\text{As}_2$  and (b)  $\text{BaFe}_2\text{P}_2$ ; (c)-(e) are cross-section view along  $(110)$  plane for  $x = 0, 0.3,$  and  $1$ , respectively [99].

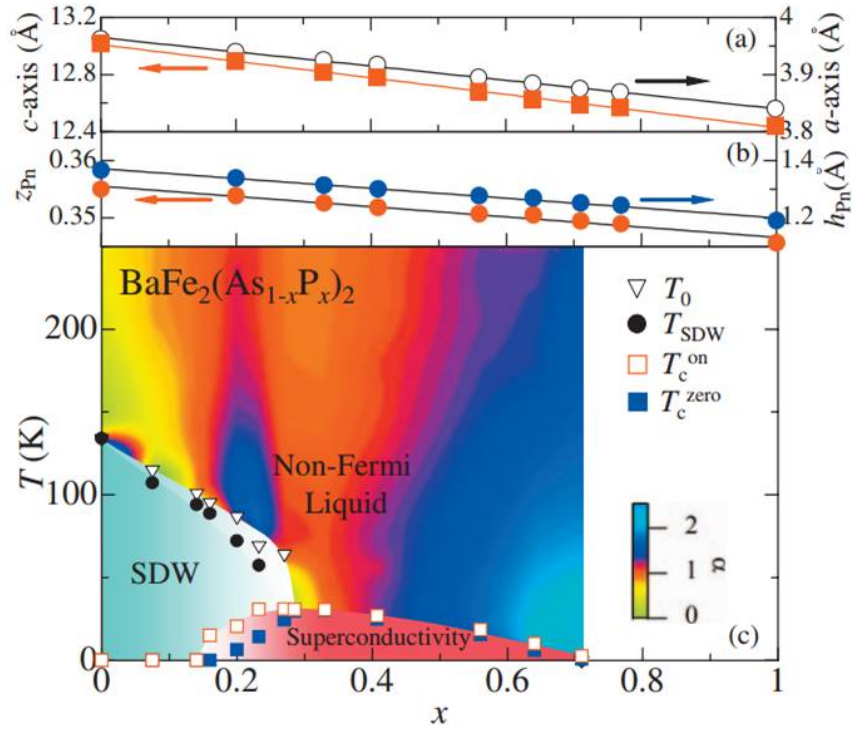


Figure 2.27: (a) Lattice constants  $a$  and  $c$ , (b)  $z$  coordinate of pnictogen atoms in the unit cell  $z_{P_n}$  and pnictogen height from the iron plane  $h_{P_n} = (z_{P_n} - 0.25) \times c$ , as well as the phase diagram of  $\text{BaFe}_2(\text{As}_{1-x}\text{P}_x)_2$  as functions of the doping concentration  $x$  [99].

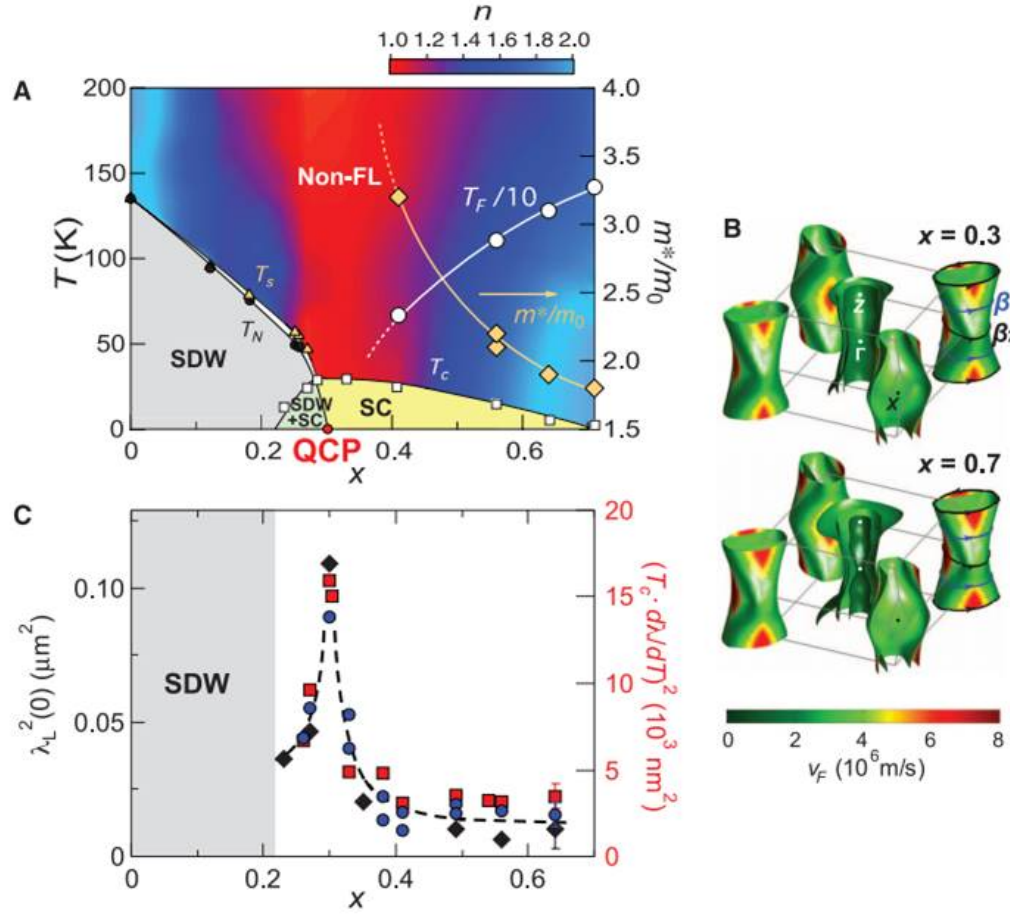


Figure 2.28: (a) Phase diagram of  $\text{BaFe}_2(\text{As}_{1-x}\text{P}_x)_2$ , in which QCP appears at  $x = 0.30$ . (b) Fermi surface of  $\text{BaFe}_2(\text{As}_{1-x}\text{P}_x)_2$ , which consists of five quasi-cylindrical pockets (three hole pockets at the center of Brillouin zone and two electron pockets at the corner). The shading represents the in-plane Fermi velocity ( $v_F$ ). (c) London penetration depth  $\lambda_L^2(0)$  in the zero-temperature limit [100].

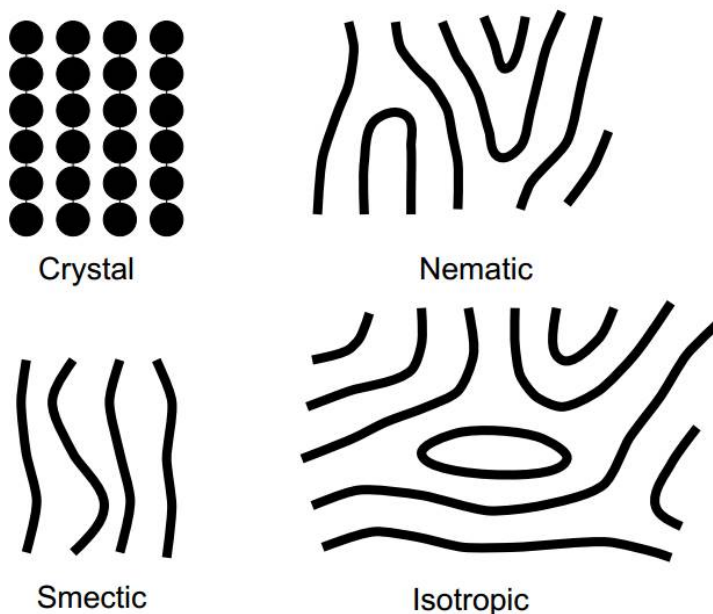


Figure 2.29: Schematic image of the local stripe order in four different phases [101].

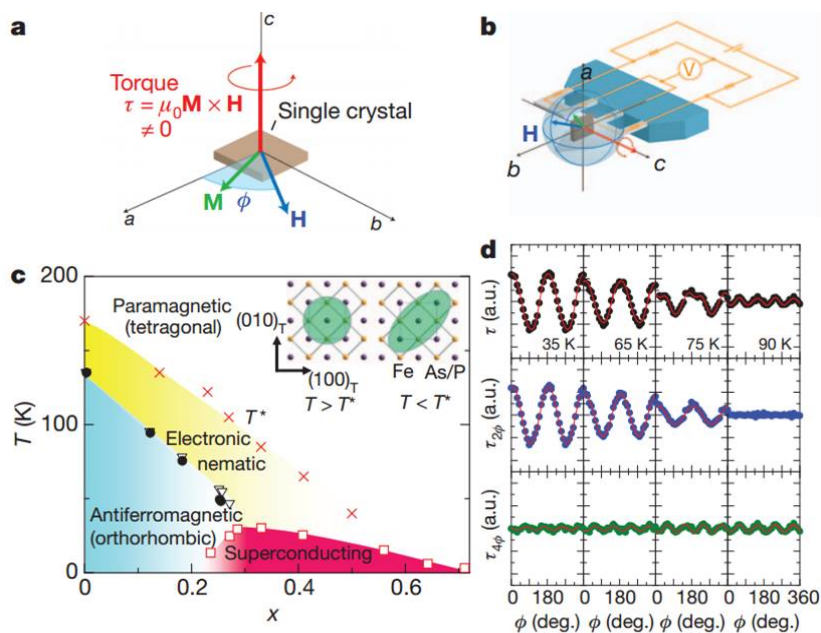


Figure 2.30: (a)-(b) Schematic diagram of the configuration of magnetic torque measurement. (c) Phase diagram of  $\text{BaFe}_2(\text{As}_{1-x}\text{P}_x)_2$ ;  $T^*$  is the nematic transition temperature. (d) Upper panels depict the temperature evolution of the raw torque; the middle and lower panel are the two- and four-fold components from the Fourier analysis of upper panel [71].

# Chapter 3

## Experimental methods

This chapter briefly describes the principle of photoemission spectroscopy and especially angle-resolved photoemission spectroscopy (ARPES). We describe the information available from ARPES measurement, and the experimental setup at Photon-Factory (PF) beamline 28A (BL28A) and Stanford Synchrotron Radiation Lightsource (SSRL) beamline 5-4 (BL5-4).

### 3.1 Principles of photoemission spectroscopy

Photoemission spectroscopy (PES) is a widely adopted technique, which enables us to detect excited electrons emitted from various samples, based on the photoelectric effect. Its main purpose is to determine the binding energies of electrons in the materials. A sketch of instrument is shown in Fig. 3.1.

#### 3.1.1 Photoemission spectroscopy

A schematic diagram of the principle of photoemission spectroscopy is illustrated in Fig. 3.2. As shown in Fig. 3.2, when an electron in the specimen absorbs an incident photon of sufficiently high energy  $\hbar\omega$  ( $h\nu$ ), it is emitted as a photoelectron. According to the energy conservation law,

$$\hbar\omega = E_f - E_i, \quad (3.1)$$

where  $E_f$  and  $E_i$  are final- and initial-state energies of electrons, and indices  $i$  and  $f$  indicate the initial and final states, respectively. The binding energy is given by  $E_B = E_F - E_i$ , where  $E_F$  is Fermi energy. The kinetic energy is given by  $E_{\text{kin}}^v = E_f - E_{\text{vac}}$ , where  $E_{\text{vac}}$  is the vacuum level. Using the work function  $\Phi$ , which is the energy separation between vacuum level and Fermi energy ( $\Phi = E_{\text{vac}} - E_F$ ), the

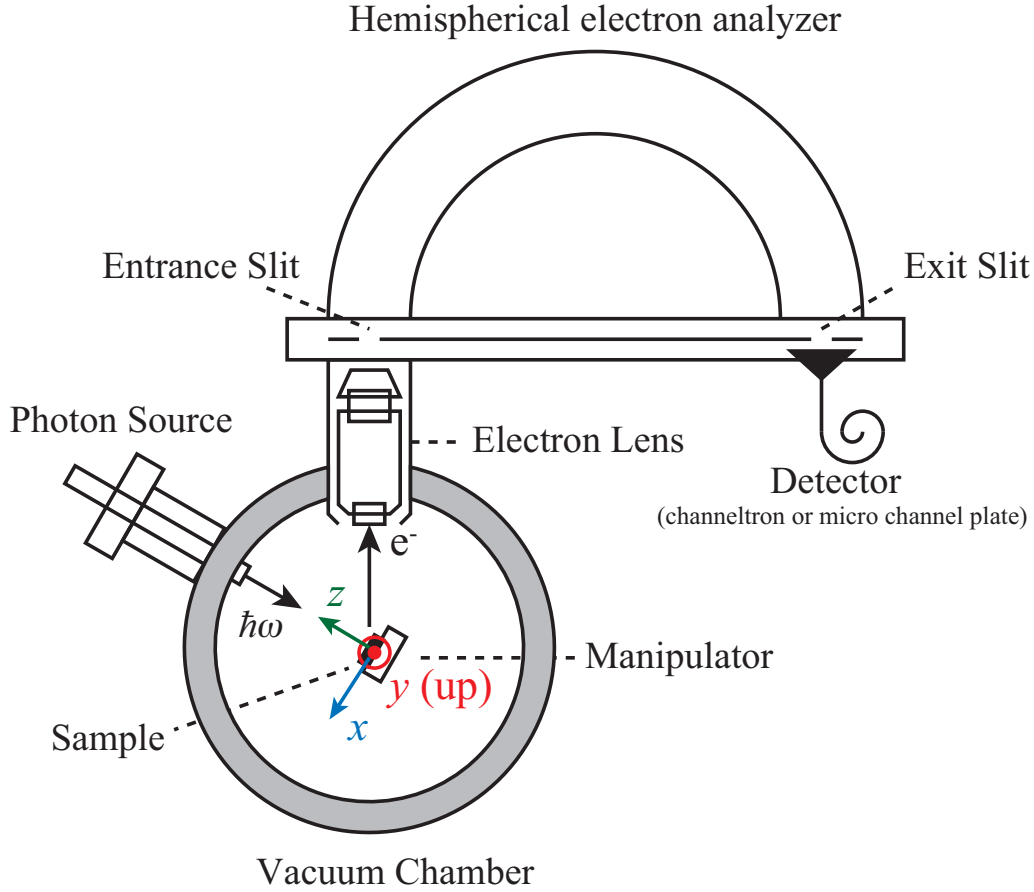


Figure 3.1: Sketch of photoemission spectroscopy (PES), in which  $x$ ,  $y$  and  $z$  axis is coordinate in sample system which will be used in section 4.4; the  $z$  axis is vertical to the sample and the  $y$  axis vertical to the ground.

kinetic energy can be expressed by

$$E_{\text{kin}}^{\text{v}} = \hbar\omega - \Phi - E_{\text{B}}, \quad (3.2)$$

Although in practical experiments, the kinetic energy measured from the Fermi energy ( $E_{\text{kin}} = E_{\text{kin}}^{\text{v}} + \Phi$ ) is a more convenient physical quantity that  $E_{\text{kin}}^{\text{v}}$  and Eq. 3.2 can be rewritten as

$$E_{\text{kin}} = \hbar\omega - E_{\text{B}}. \quad (3.3)$$

According to Koopmans' theorem,  $E_{\text{B}}$  equals the negative Hartree-Fock orbital energy  $\epsilon_k$  measured from  $E_{\text{F}}$ , as expressed by

$$E_{\text{B}} = E_{\text{F}} - \epsilon_k. \quad (3.4)$$

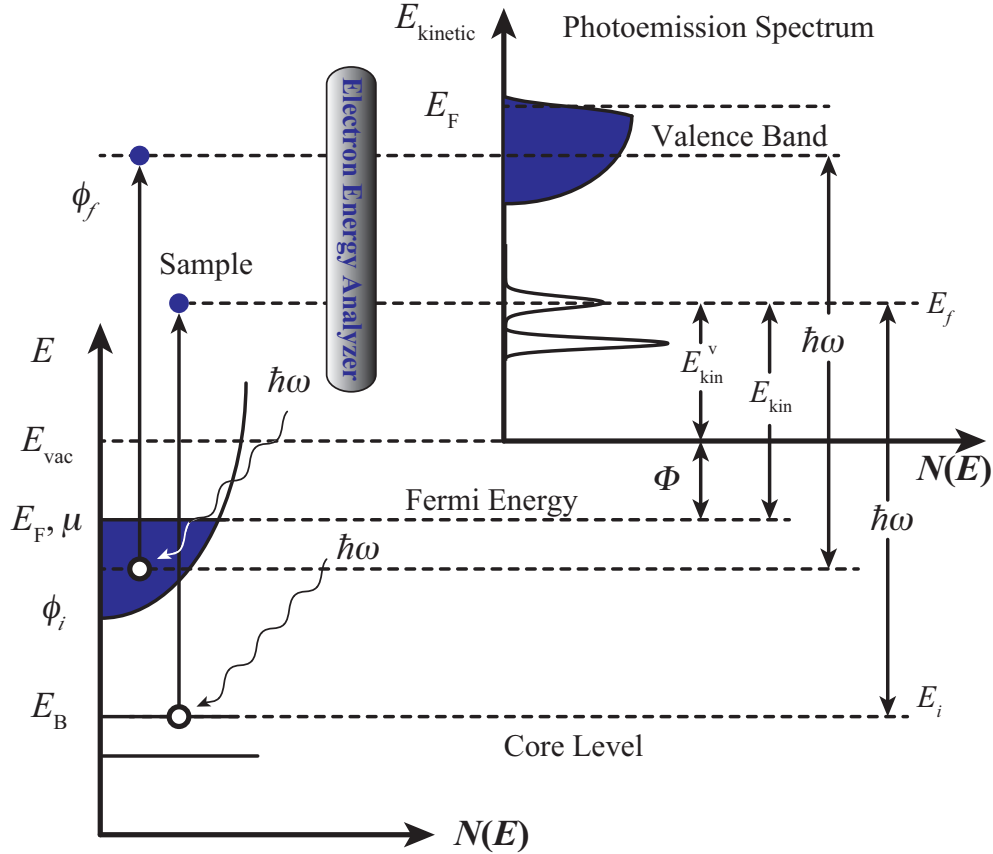


Figure 3.2: Schematic diagram of the principle of photoemission spectroscopy (PES). The left half and right half are the electronic structure of the sample and the photoemission spectroscopy spectrum, respectively. Through the electron energy analyzer, the information of electronic structure can be expressed by the photoemission spectrum.

Under this condition, the photoemission spectrum  $I(E_B)$  is proportional to the density of states (DOS) or  $N(E)$ , as

$$I(E_B) \propto \sum_k \delta(E_B - E_F + \epsilon_k) \propto N(E_F - E_B). \quad (3.5)$$

Therefore, through an electron energy analyzer, the information about the electronic structure can be expressed by a photoemission spectrum, as shown in Fig. 3.2.

### 3.1.2 Angle-resolved photoemission spectroscopy (ARPES)

Among various types of photoemission spectroscopies the angle-resolved photoemission spectroscopy (ARPES) is unique because it's the only tool in determining the band structure of solid materials. In ARPES measurement, the obtained spectrum

gives not only the energy distribution but also the momentum distribution of the electrons in the solid. Schematic diagram of the principle of hemispherical electron analyzer of ARPES is illustrated in Fig. 3.3.

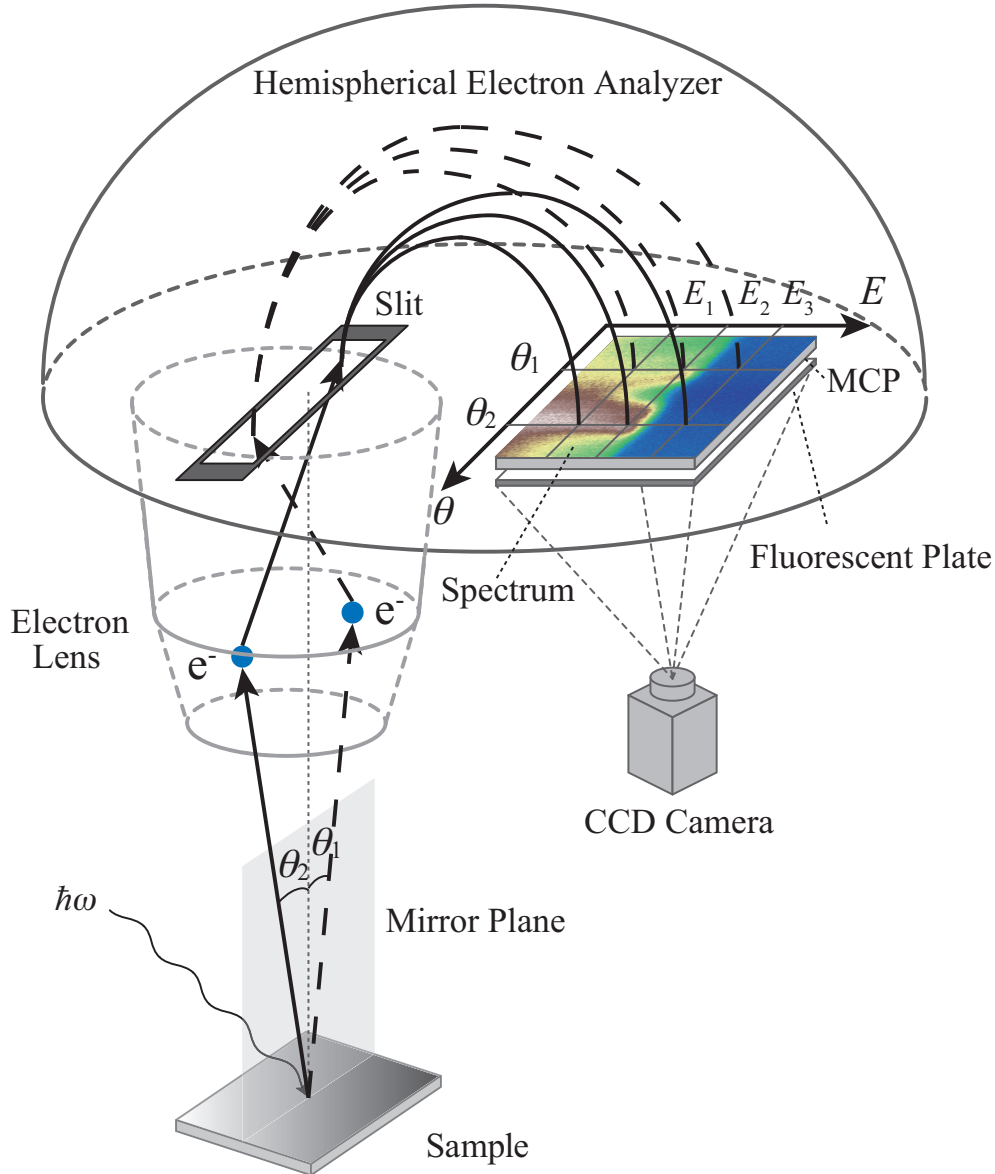


Figure 3.3: Schematic diagram of the principle of hemispherical electron analyzer.

The incident light from a certain angle energizes electrons to different angles from the specimen located at the focus of the electron lens. The energized electrons carry the dispersion relation of energy band in the detected sample. After deflected by electrical or magnetic fields in the analyzer chamber, the electrons move in a semicircle track and reach different locations of CCD camera, corresponding to the electronic momentum and energy.

In the photoexcitation process, the wave vector of an electron should satisfy the momentum conservation law before and after the photoexcitation except for the reciprocal lattice vector, as expressed by

$$\mathbf{k}_f = \mathbf{k}_i + \mathbf{k}_l + \mathbf{G}, \quad (3.6)$$

where  $\mathbf{k}_f$  and  $\mathbf{k}_i$  are the wave vector of the electron in initial state and final state,  $\mathbf{k}_l$  is the wave vector of the incident photon, and  $\mathbf{G} = (2\pi/a, 2\pi/b, 2\pi/c)$  is an arbitrary reciprocal lattice vector, respectively. Since the wave vector of the ultraviolet light  $k_l$  is negligible comparing with the size of the Brillouin zone. Approximatively we have

$$\mathbf{k}_f = \mathbf{k}_i + \mathbf{G}. \quad (3.7)$$

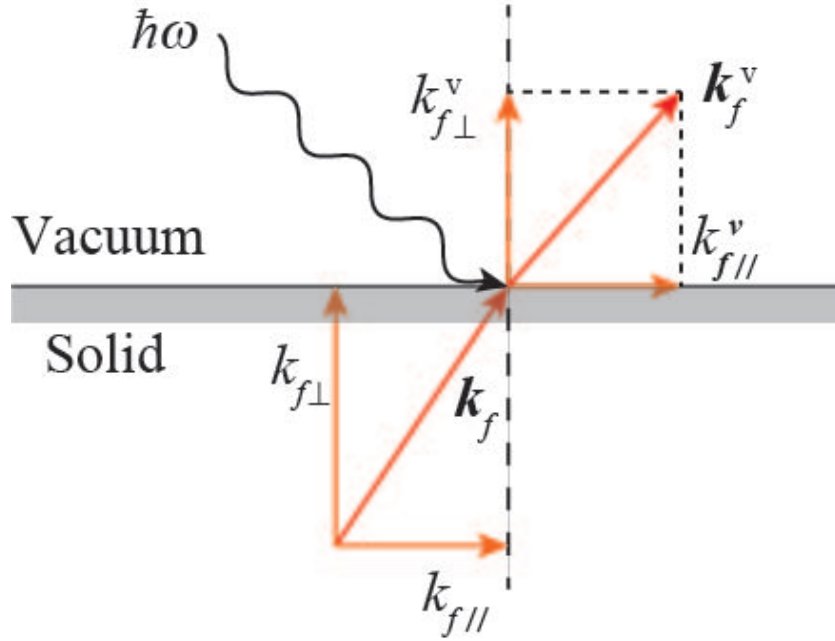


Figure 3.4: Schematic diagram of the photoelectron emission near the boundary between a solid medium and the vacuum; the parallel component of the wave vector keeps unchanged while the perpendicular one does not.

When the photoelectron is emitted from the material to the vacuum, the perpendicular component of its wave vector changes owing to the potential barrier of the inner potential; and the parallel component of the wave vector keeps the same due to the translational symmetry along the material surface. The schematic diagram of this process is illustrated in Fig. 3.4.

$$k_{f||}^v = k_{f||} + G_{||}, \quad (3.8)$$

where  $k_{f\parallel}^v$  is the parallel component of  $\mathbf{k}_f^v$ , which is the wave vector of an excited electron in vacuum.

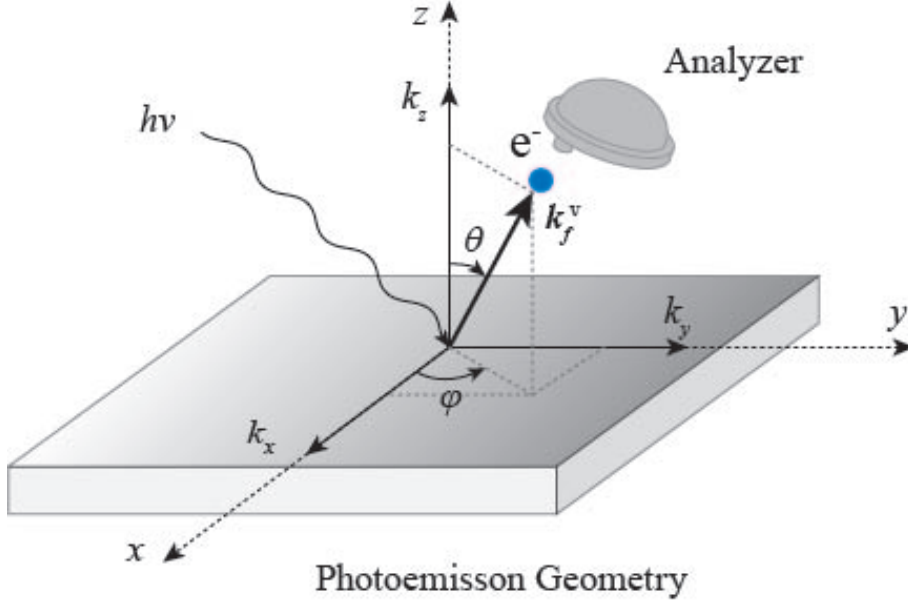


Figure 3.5: Schematic diagram and definition of parameters in ARPES.

In the ARPES measurement, as shown in Fig. 3.5, an electron energy analyzer is employed to detect the kinetic energy  $E_{\text{kin}}^v$  and the momentum  $\mathbf{k}_f^v$ , and the angle  $\theta$ ,  $\phi$  of the photoelectron momentum. According to Fig. 3.5, the momentum  $k_{f\parallel}^v$  and  $k_{f\perp}^v$ , which parallel and vertical to the plane, respectively, is given by

$$k_{f\parallel}^v = \frac{\sqrt{2m_e E_{\text{kin}}^v}}{\hbar} \sin \theta \quad (3.9)$$

and

$$k_{f\perp}^v = \frac{\sqrt{2m_e E_{\text{kin}}^v}}{\hbar} \cos \theta; \quad (3.10)$$

$k_x^v$  and  $k_y^v$  are two components of the in-plane momentum  $k_{f\parallel}^v$ ; and it is easy to obtain

$$k_x^v = \frac{\sqrt{2m_e E_{\text{kin}}^v}}{\hbar} \cos \phi \sin \theta, \quad (3.11)$$

$$k_y^v = \frac{\sqrt{2m_e E_{\text{kin}}^v}}{\hbar} \sin \phi \sin \theta. \quad (3.12)$$

In the photoemission process, both the energy  $E \equiv -E_B$  and the parallel momentum  $k_{\parallel}$  of the electron can be determined by ARPES. Now taking the

reciprocal lattice vector into account, the above equations can be revised as

$$k_x = \frac{\sqrt{2m_e E_{\text{kin}}^{\text{v}}}}{\hbar} \cos \phi \sin \theta + \frac{2\pi n_x}{a}, \quad (3.13)$$

$$k_y = \frac{\sqrt{2m_e E_{\text{kin}}^{\text{v}}}}{\hbar} \sin \phi \sin \theta + \frac{2\pi n_y}{b}, \quad (3.14)$$

where  $n_x$  and  $n_y$  are arbitrary integers. The relationship the energy (in Fig. 3.2) can be rewritten as

$$\begin{aligned} E &= E_{\text{kin}} - \hbar\omega, \\ E_{\text{kin}} &= E_{\text{kin}}^{\text{v}} + \Phi, \end{aligned} \quad (3.15)$$

where

$$E_{\text{kin}} = \frac{\hbar^2(k_{f\parallel}^2 + k_{f\perp}^2)}{2m_e} - E_0. \quad (3.16)$$

Considering  $k_{f\parallel}^{\text{v}} = k_{f\parallel}$ , and Eq. 3.9, 3.10, 3.15, and 3.16,

$$\begin{aligned} k_{f\perp} &= \frac{\sqrt{2m_e(E_{\text{kin}}^{\text{v}} \cos^2 \theta + E_0 + \Phi)}}{\hbar} \\ &= \frac{\sqrt{2m_e[(E + \hbar\omega - \Phi) \cos^2 \theta + V_0]}}{\hbar}, \end{aligned} \quad (3.17)$$

where inner potential is given by  $V_0 = E_0 + \Phi$ .

Figure 3.6 schematically illustrates the procedure for mapping band dispersion from the ARPES spectrum. For a two-dimensional system (e.g., high  $T_c$  superconductors),  $E$  and  $k_{f\parallel}^{\text{v}}$  are sufficient to map the energy-momentum dispersion of the band structure. For the record, since iron-based superconductors are quasi-three dimensional systems, an additional term  $k_{f\perp}$  should also be taken into account; which will be discussed in chapter 4.

### 3.1.3 Spectral function and self-energy

Last subsection is based on the one-electron approximation; however, many-body effect should also be taken into account. Considering a system with  $N$  electrons and energy  $E_g^N$ , the photoemission process is regarded as the removal of a peripheral electron from a ground state  $|\Psi_g^N\rangle$ , leaving the new  $(N - 1)$ -electron system in an excited state  $|\Psi_i^{N-1}\rangle$  with energy  $E_i^{(N-1)}$ . The photoemission spectrum  $A(k, \omega)$  of the system, corresponding to the single-electron excitation spectrum of the system, can be expressed by

$$A(k, \omega) = \sum_i |\langle \Psi_i^{N-1} | c_k | \Psi_g^N \rangle|^2 \delta(\omega + E_i^{N-1} - E_g^N), \quad (3.18)$$

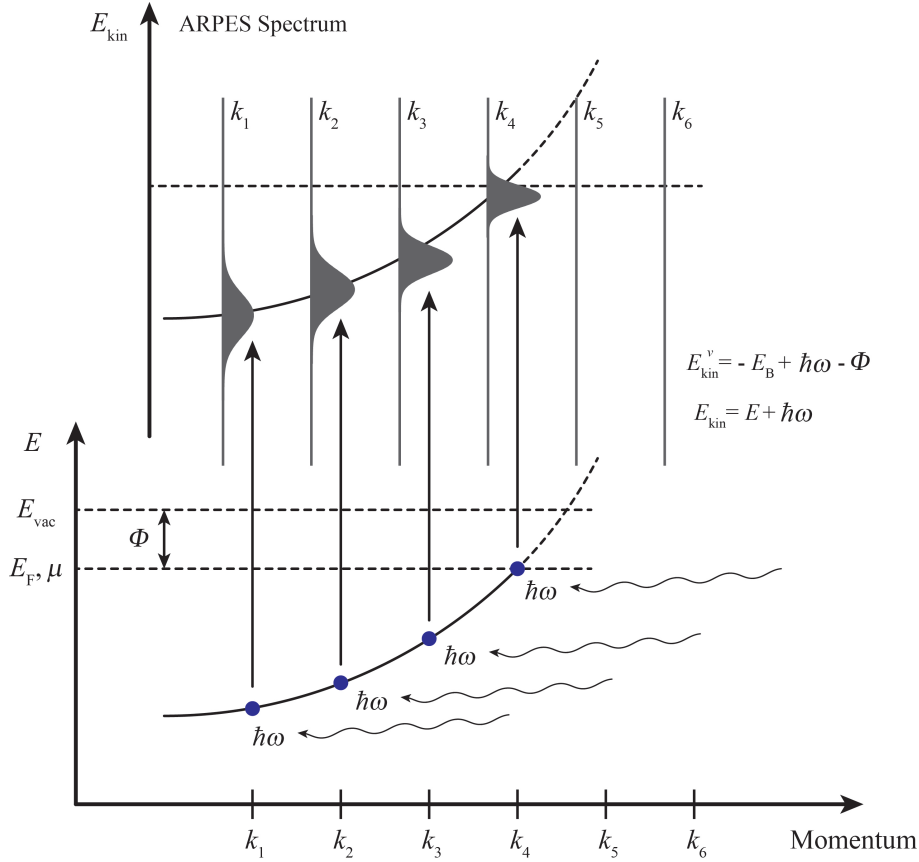


Figure 3.6: Schematic diagram of the procedure for mapping band dispersion from the ARPES spectrum.

where  $c_k$  is the annihilation operator of an electron whose momentum is  $k$ . Define Green's function  $G(\mathbf{k}, t)$  as

$$G(\mathbf{k}, t) \equiv -i\theta(t)\langle\Psi_g^N|\{c_{\mathbf{k}}(t), c_{\mathbf{k}}^\dagger(0)\}|\Psi_g^N\rangle, \quad (3.19)$$

where  $c_k^\dagger$  is the creation operator of the same electron, as expressed by

$$c_k(t) \equiv e^{iHt}c_k e^{-iHt}. \quad (3.20)$$

Then derive the Fourier transformation of  $G(k, t)$  as the following equations:

$$\begin{aligned}
G(k, \omega) &= \int_0^\infty dt G(k, t) e^{i\omega t - 0^+ t} \\
&= -i \int_0^\infty dt \langle \Psi_g^N | c_k(t) c_k^\dagger + c_k^\dagger c_k(t) | \Psi_g^N \rangle e^{i\omega t - 0^+ t} \\
&= -i \int_0^\infty dt \left( \langle \Psi_g^N | e^{iHt} c_k e^{-iHt} \sum_i |\Psi_i^{N+1}\rangle \langle \Psi_i^{N+1} | c_k^\dagger | \Psi_g^N \rangle \right. \\
&\quad \left. + \langle \Psi_g^N | c_k^\dagger \sum_i |\Psi_i^{N-1}\rangle \langle \Psi_i^{N-1} | e^{iHt} c_k e^{-iHt} | \Psi_g^N \rangle \right) e^{i\omega t - 0^+ t} \\
&= -i \int_0^\infty dt \left( \sum_i e^{iE_g^N t} e^{-iE_i^{N+1} t} e^{i\omega t - 0^+ t} \left| \langle \Psi_i^{N+1} | c_k^\dagger | \Psi_g^N \rangle \right|^2 \right. \\
&\quad \left. + \sum_i e^{iE_i^{N-1} t} e^{-iE_g^N t} e^{i\omega t - 0^+ t} \left| \langle \Psi_i^{N-1} | c_k | \Psi_g^N \rangle \right|^2 \right) \\
&= \sum_i \frac{i}{iE_g^N - iE_i^{N+1} + i\omega - 0^+} \left| \langle \Psi_i^{N+1} | c_k^\dagger | \Psi_g^N \rangle \right|^2 \\
&\quad + \sum_i \frac{i}{iE_i^{N-1} - iE_g^N + i\omega - 0^+} \left| \langle \Psi_i^{N-1} | c_k | \Psi_g^N \rangle \right|^2 \\
&= \sum_i \frac{1}{\omega - E_i^{N+1} + E_g^N + i0^+} \left| \langle \Psi_i^{N+1} | c_k^\dagger | \Psi_g^N \rangle \right|^2 \\
&\quad + \sum_i \frac{1}{\omega + E_i^{N-1} - E_g^N + i0^+} \left| \langle \Psi_i^{N-1} | c_k | \Psi_g^N \rangle \right|^2 \\
&= \sum_i \left| \langle \Psi_i^{N+1} | c_k^\dagger | \Psi_g^N \rangle \right|^2 \left[ \frac{P}{\omega - E_i^{N+1} + E_g^N} - i\pi \delta(\omega - E_i^{N+1} + E_g^N) \right] \\
&\quad + \sum_i \left| \langle \Psi_i^{N-1} | c_k | \Psi_g^N \rangle \right|^2 \left[ \frac{P}{\omega + E_i^{N-1} - E_g^N} - i\pi \delta(\omega + E_i^{N-1} - E_g^N) \right], \tag{3.21}
\end{aligned}$$

where  $H$  is the Hamilton of the system and  $P$  is the principal value of the integral.

When  $\omega \leq \mu$ , the spectral function  $A(k, \omega)$  is given by

$$\begin{aligned}
A(\mathbf{k}, \omega) &= -\frac{1}{\pi} \text{Im} G(\mathbf{k}, \omega) \\
&= \sum_i \left| \langle \Psi_i^{N-1} | c_k | \Psi_g^N \rangle \right|^2 \delta(\omega + E_i^{N-1} - E_g^N). \tag{3.22}
\end{aligned}$$

Thus in this case ( $\omega \leq \mu$ ), we have

$$I(\omega) = -\frac{1}{\pi} \text{Im} G(\mathbf{k}, \omega). \tag{3.23}$$

The Green's function  $G(\mathbf{k}, \omega)$  can be expressed using the self-energy  $\Sigma(\mathbf{k}, \omega)$ , in which the renormalization of particle interactions has been carried out,

$$G(\mathbf{k}, \omega) = \frac{1}{\omega - \epsilon_{\mathbf{k}}^0 - \Sigma(\mathbf{k}, \omega)}. \quad (3.24)$$

Hence, Eq. 3.22 can be revised as

$$\begin{aligned} A(\mathbf{k}, \omega) &= -\frac{1}{\pi} \text{Im}G(\mathbf{k}, \omega) \\ &= -\frac{1}{\pi} \frac{\text{Im}\Sigma(\mathbf{k}, \omega)}{\left(\omega - \epsilon_{\mathbf{k}}^0 - \text{Re}\Sigma(\mathbf{k}, \omega)\right)^2 + \left(\text{Im}\Sigma(\mathbf{k}, \omega)\right)^2}. \end{aligned} \quad (3.25)$$

The real part of the pole of  $G(\mathbf{k}, \omega)$ ,  $\omega = E_{\mathbf{k}}^*$  is determined by the following equation:

$$E_{\mathbf{k}}^* - \epsilon_{\mathbf{k}}^0 - \text{Re}\Sigma(\mathbf{k}, \omega) = 0; \quad (3.26)$$

and the residue of the pole  $Z_{\mathbf{k}}$  is given by

$$Z_{\mathbf{k}} = \left(1 - \frac{\partial \text{Re}\Sigma(\mathbf{k}, \omega)}{\partial \omega} \Big|_{\omega=E_{\mathbf{k}}^*}\right)^{-1}. \quad (3.27)$$

Near  $\omega = E_{\mathbf{k}}^*$ , we can expand Eq. 3.26 as follows,

$$\omega - \epsilon_{\mathbf{k}}^0 - \text{Re}\Sigma(\mathbf{k}, \omega) \cong \frac{1}{Z_{\mathbf{k}}} (\omega - E_{\mathbf{k}}^*). \quad (3.28)$$

Therefore, Eq. 3.25 can be revised as

$$A(\mathbf{k}, \omega) = -\frac{Z_{\mathbf{k}}}{\pi} \frac{Z_{\mathbf{k}} \text{Im}\Sigma(\mathbf{k}, \omega)}{\left(\omega - E_{\mathbf{k}}^*\right)^2 + \left(Z_{\mathbf{k}} \text{Im}\Sigma(\mathbf{k}, \omega)\right)^2}. \quad (3.29)$$

In the vicinity of  $E_{\text{F}}$ ,  $E_{\mathbf{k}}$  can be written as  $E_{\mathbf{k}} = v_{\mathbf{k}}^*(k - k_{\text{F}})$ , where  $v_{\mathbf{k}}^* \equiv |\nabla E_{\mathbf{k}}^*|$  is the renormalized Fermi velocity and  $k$  is taken perpendicular to the Fermi surface. Then, the momentum distribution curve (MDC) at the Fermi level ( $\omega=0$ ) is given by

$$A(\mathbf{k}, 0) = -\frac{Z_{\mathbf{k}}/v_{\mathbf{k}}^*}{\pi} \frac{Z_{\mathbf{k}} \text{Im}\Sigma(\mathbf{k}, \omega)/v_{\mathbf{k}}^*}{\left(k - k_{\text{F}}\right)^2 + \left(Z_{\mathbf{k}} \text{Im}\Sigma(\mathbf{k}, 0)/v_{\mathbf{k}}^*\right)^2}. \quad (3.30)$$

Thus, the MDC is given as a Lorentzian with a full width at half maximum (FWHM) of  $\Delta k = 2|Z_{\mathbf{k}} \text{Im}\Sigma(\mathbf{k}, \omega)/v_{\mathbf{k}}^*|$ , if the  $k$ -dependence of  $Z_{\mathbf{k}}$ ,  $\text{Im}\Sigma(\mathbf{k}, 0)$  and  $v_{\mathbf{k}}^*$  can be neglected. Since the inverse life time of the quasi-particle is given by  $1/\tau_{\mathbf{k}} = -2Z_{\mathbf{k}} \text{Im}\Sigma$ ,  $1/\Delta k$  represents the mean free path  $l_{\mathbf{k}}$ :

$$l_{\mathbf{k}} = v_{\mathbf{k}}^* \tau_{\mathbf{k}} = \frac{1}{\Delta k}. \quad (3.31)$$

Figure 3.7 summarizes the relationship between the obtained ARPES spectra and momentum distribution curve (MDC) and energy distribution curve (EDC).

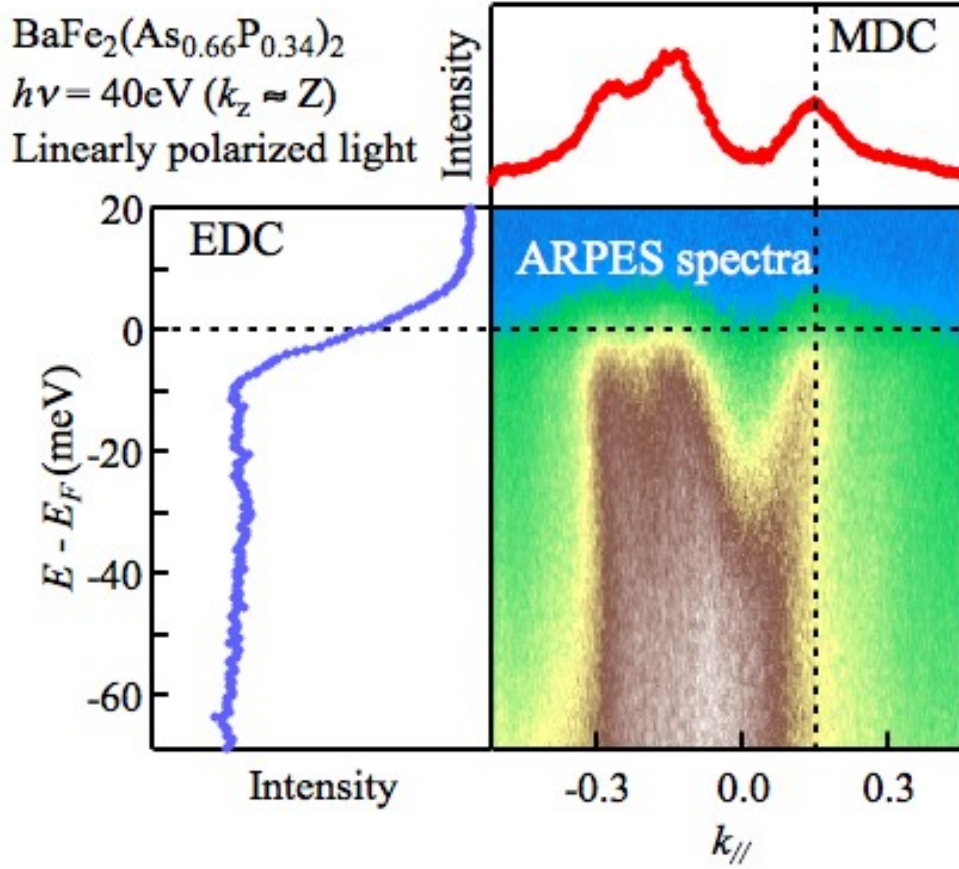


Figure 3.7: Relationship between the ARPES spectra, momentum distribution curve (MDC) and energy distribution curve (EDC).

### 3.1.4 Electron escape depth

Photoemission spectroscopy (PES) can only detect a surface layer (several angstroms to several nanometers) of the samples; thus, clean surface of the samples under the ultra-high vacuum (UHV) condition is necessary when we want to study the bulk properties. As shown in Fig. 3.8 [102], the electron mean free path  $\lambda$  gives the electron escape depth of photoelectrons, which is determined by electron-electron and electron-phonon collisions. Usually, electron-phonon scattering plays a role only at low energies, so the mean free path (escape depth) of an electron  $\lambda$  is determined mainly by electron-electron interaction in this case. The inverse of the average mean free path  $\lambda$  is proportional to the scattering cross-section, which means

$$\lambda^{-1} = N\sigma, \quad (3.32)$$

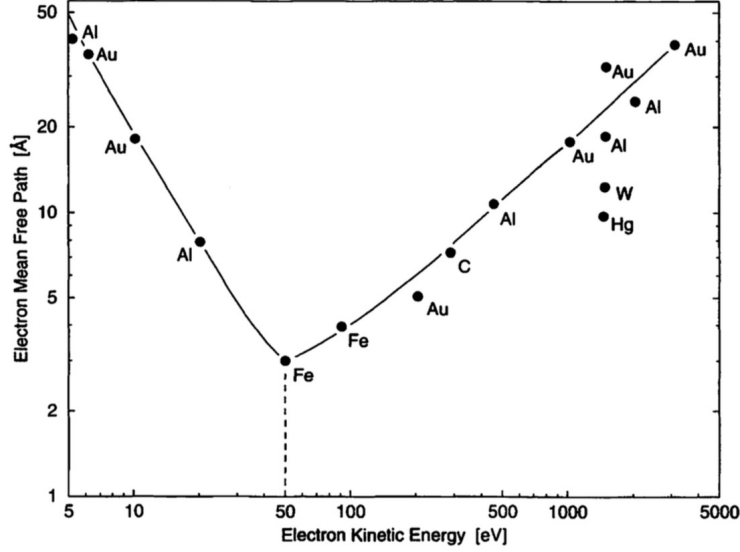


Figure 3.8: Experimental results of the electron mean free path  $\lambda$  as a function of the electron kinetic energy  $E_{\text{kin}}$  plotted on a logarithmic scale for several different metals [102]

where  $N$  is the electron number per unit volume,  $\sigma$  is the cross-section of electron-electron scattering, as expressed by

$$\frac{d\sigma}{d\Omega d\omega} = \frac{\hbar^2}{(\pi e a_0)^2} \frac{1}{q^2} \text{Im} \left[ -\frac{1}{\varepsilon(\mathbf{q}, \omega)} \right], \quad (3.33)$$

where  $\varepsilon(\mathbf{q}, \omega)$  is the dielectric function,  $\hbar\mathbf{q}$  is the momentum transfer,  $\omega$  is the energy loss of the electron,  $a_0$  is the Bohr radius ( $0.529 \text{ \AA}$ ), and  $\Omega$  is the angle of the scattered electron [102, 103].

According to Eqs. 3.32 and 3.33, the mean free path is determined by the loss function  $\text{Im}(-1/\varepsilon)$ . The loss function is small unless the energy transfer exceeds the gap energy in insulators and semiconductors. Thus, the mean free path  $\lambda$  is very large at small energies, as shown in the low energy range of Fig. 3.8. When the energy is not very small, the binding energies of electrons are negligible in the solid, which means that electrons can be roughly approximated as a free-electron gas. Under this condition,  $\text{Im}(-1/\varepsilon)$  is determined by the electron density (or the mean electron-electron distance  $r_s$ ). Therefore, even  $\varepsilon(\mathbf{q}, \omega)$  varies between different materials, the mean free path  $\lambda$  as a function of kinetic energy is roughly similar for all materials, as expressed by

$$\lambda^{-1} \cong \sqrt{3} \frac{a_0 R}{E_{\text{kin}}} r_s^{-\frac{3}{2}} \ln \left[ \left( \frac{4}{9\pi} \right)^{\frac{2}{3}} \frac{E_{\text{kin}} r_s^2}{R} \right], \quad (3.34)$$

where  $a_0 = 0.529 \text{ \AA}$ ,  $R = 13.6 \text{ eV}$ , and  $r_s$  is measured in units of the Bohr radius  $a_0$  [102] [103]. This gives the escape depth as a function of photoelectron kinetic energy  $E_{\text{kin}}$ , which is roughly “universal”. As shown in Fig. 3.8, the electron mean free paths in some metals measured at the kinetic energy of 1480 eV have deviation from Eq. 3.34; yet the function is still roughly valid. Different from the above-mentioned qualitative results (Eq. 3.34), some other quantitative theoretical research on the inelastic mean free path (IMFP) has been reported [104].

## 3.2 Experimental setup

### 3.2.1 PF BL-28A

Here a brief introduction to the beamline 28A (BL-28A) of Photon-Factory (PF), High Energy accelerator Research Organization (KEK) and the related measurement system is presented. BL-28A is an undulator beamline with a Spherical Grating Monochromator (SGM). Both linearly polarized light and circularly polarized light as well as a wide range of photon energy from 30 to 800 eV are available in BL-28A. The endstation BL-28A mainly consists of a preparation chamber and an ARPES measurement chamber (main chamber), as shown in Fig. 3.9(a).

Employing an arm it is convenient to transfer the samples from one chamber to another so as to conduct the characterization or angle-resolved photoemission measurement. The samples are cleaved in the main chamber (*in situ*) so that a clean surface is available for the test. In the ARPES chamber, a hemispherical analyzer (Gamma-data Scienta 2002) is equipped, connecting a 2-dimensional multichannel plate detection system. In the measurement, the sample motion is controlled by a manipulator with five degrees of freedom: three translational degrees and two rotational ones. Measurement temperature has a range from about 9 K to room temperature.

The schematic diagram of experimental geometry in the measurement of the sample surface and the electron energy analyzer can be seen in Fig. 3.9(b). The emission angle can be adjusted by rotating the sample with two axes  $\theta$  and  $\phi$  while the position of the analyzer itself is fixed.

The main conditions adopted in the experiments are listed in Table 3.1.

### 3.2.2 SSRL BL-5-4

Following is a brief introduction to the beamline 5-4 (BL5-4) of Stanford Synchrotron Radiation Laboratory (SSRL) and the related measurement system. Same as abovementioned BL-28A in PF, beamline 5-4 is also an undulator beamline, yet

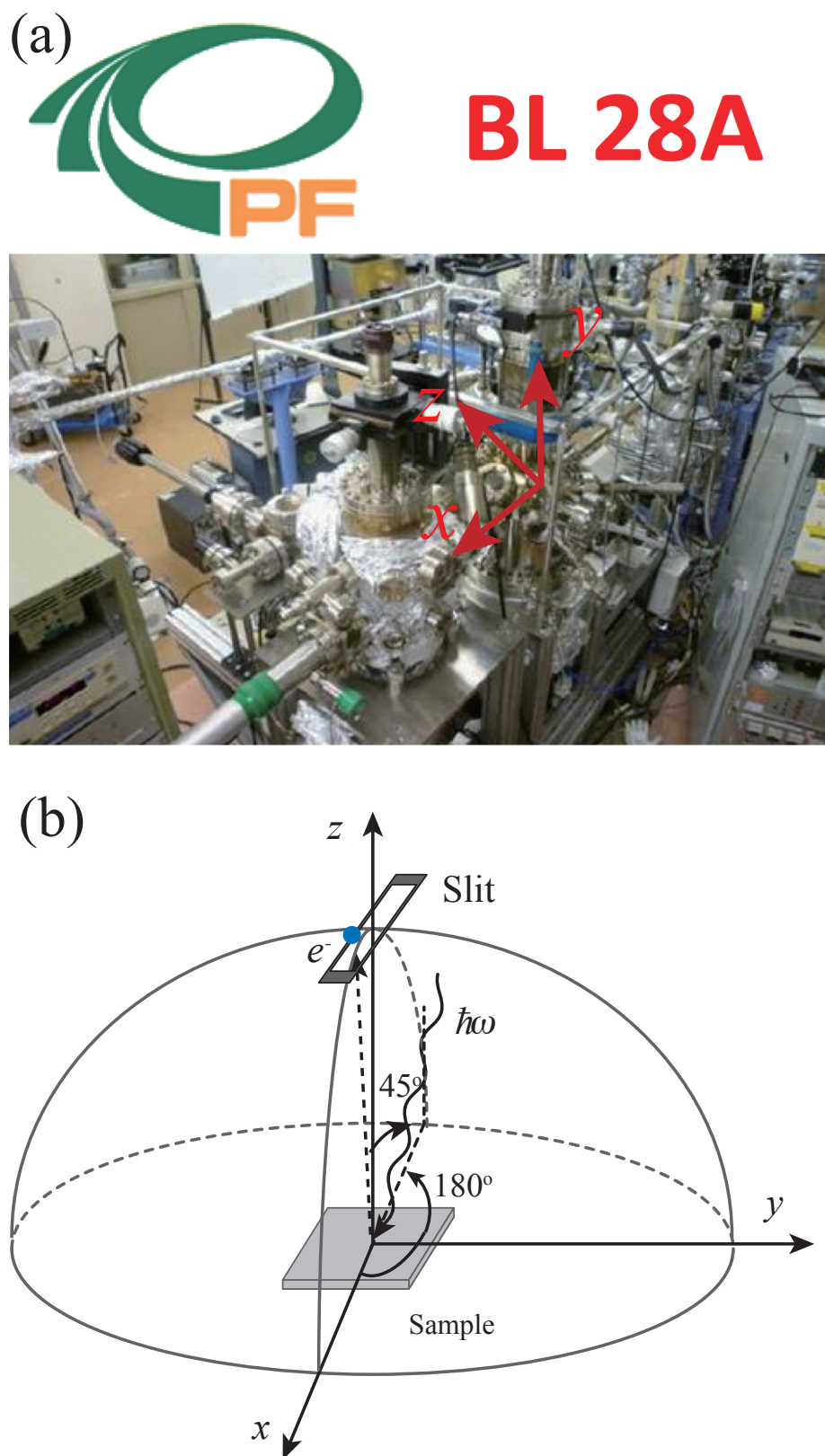


Figure 3.9: Overview of the measurement system at BL-28A.

Table 3.1: Main measurement conditions used in BL28A of PF.

$\text{BaFe}_2(\text{As}_{1-x}\text{P}_x)_2$	$x = 0.3$	$x = 0.34$	$x = 0.38$
$T_c$	30 K	27 K	24 K
Measurement temperature	10 K, 35 K	10 K, 30 K	10 K, 30 K
$h\nu$	40 eV		
Polarization	Linearly; circularly		
$\Delta E$	$\approx 10$ meV		
Pressure	$\approx 10^{-8}$ Pa		
Analyzer	SCIENTA SES2002		

with a normal incidence monochromator (NIM). NIM is advantageous for photons in the vacuum ultraviolet (VUV) range and NIM monochromators have much higher throughput for low energy photons. Therefore, the NIM monochromator in beamline 5-4 is limited to a photon energy range of 15-32 eV. This is beneficial for most high- $T_c$  superconductors owing to their large photo-ionization cross-sections of photons (in the magnitude order of a few meV).

The endstation of beamline 5-4 also has a preparation chamber and an ARPES measurement chamber as shown in Fig. 3.10(b). The samples are transferred to the chamber for angle-resolved photoemission measurement and then cleaved *in situ* as to ensure an available clean surface for the measurement. The sample motion can be easily controlled by a manipulator with five degrees of freedom: three translational degrees and two rotational ones. In the ARPES chamber, a hemispherical analyzer (Gamma-data Scienta SES200 and 4000) is equipped, connecting a 2-dimensional multichannel plate detection system. The experimental geometry used in the present measurements is the same as that of PF BL-28A. Despite the abundant similarities between SSRL BL-5-4 and PF BL-28A, it should be emphasized that several variations also exists. The measurement temperature range is from about 5 K to room temperature as well as the energy range. In addition, as shown in Fig. 3.10(b) and Fig. 3.9(b), the orientation of the slit are different.

The main conditions adopted in the experiments are listed in Table 3.2.

Table 3.2: Main measurement conditions used in BL5-4 of SSRL.

$\text{BaFe}_2(\text{As}_{1-x}\text{P}_x)_2$	$x = 0.3$	$x = 0.45$
$T_c$	30 K	20 K
Measurement temperature	5 K, 35 K	5 K, 30 K
$h\nu$	28 eV	18 eV
Polarization	Linearly; circularly	
$\Delta E$	$\approx 8$ meV	
Pressure	$\approx 10^{-9}$ Pa	
Analyzer	SCIANTA R4000	

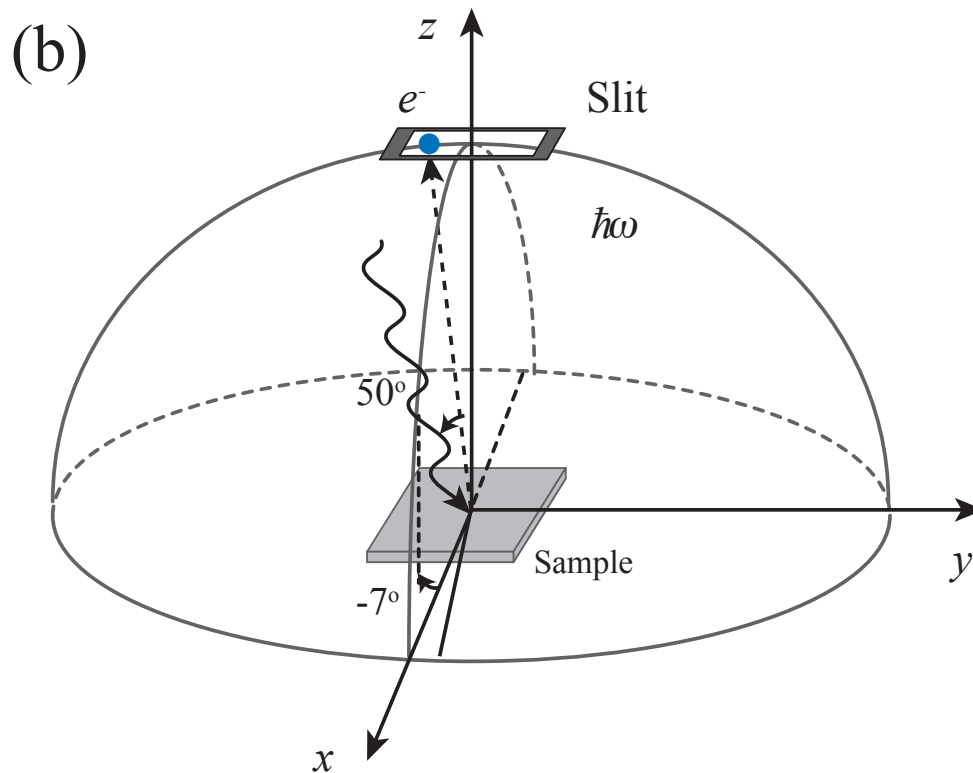
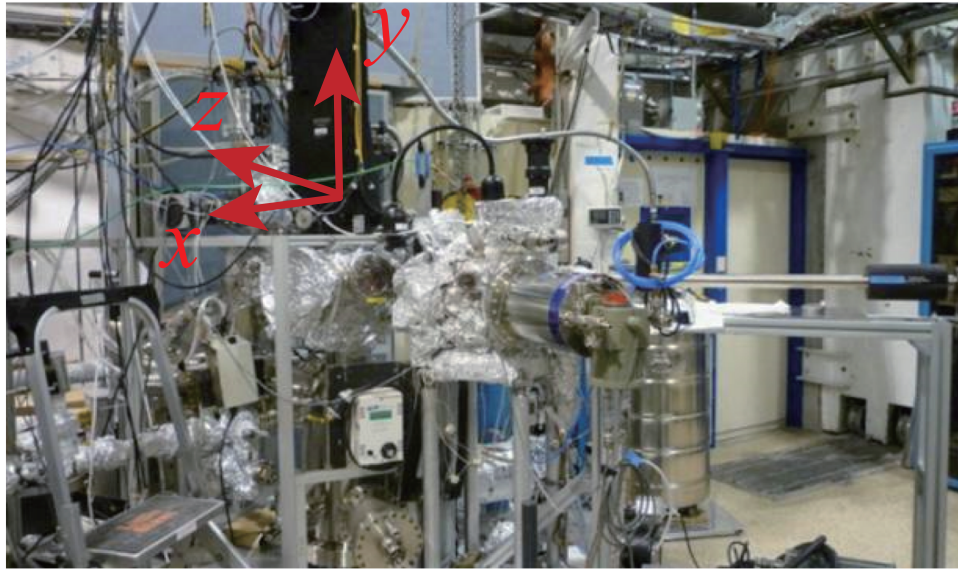


Figure 3.10: Overview of the measurement system at BL-5-4.



# Chapter 4

## Analysis of ARPES spectra

### 4.1 Electric dipole approximation and selection rules

According to the electric dipole approximation and selection rules, the total decay rate of atoms absorbing a photon can be expressed by

$$\Gamma_{\text{tot}} = \frac{e^2 (E_i - E_n)}{2\pi\hbar^2 m^2 c^3} \sum_{\lambda} \int d\Omega_{\gamma} \left| \frac{im(E_n - E_i)}{\hbar} \langle \phi_n | \hat{\mathbf{e}} \cdot \mathbf{r} | \phi_i \rangle \right|^2, \quad (4.1)$$

in which  $\hat{\mathbf{e}}$  is the unit vector in the direction of light polarization,  $\phi_i$  is the initial state, and  $\phi_n$  is the final state of electron, respectively. Equation 4.1 can be rewritten in polar coordinates, as

$$\begin{aligned} \langle \phi_n | \hat{\mathbf{e}} \cdot \mathbf{r} | \phi_i \rangle &= \int_0^{\infty} r^2 dr R_{n_n l_n}^* R_{n_i l_i} \int d\Omega Y_{l_n m_n}^* \hat{\mathbf{e}} \cdot \mathbf{r} Y_{l_i m_i} \\ &= \int_0^{\infty} r^3 dr R_{n_n l_n}^* R_{n_i l_i} \int d\Omega Y_{l_n m_n}^* \hat{\mathbf{e}} \cdot \hat{\mathbf{r}} Y_{l_i m_i}, \end{aligned} \quad (4.2)$$

where indices  $n$  and  $i$  are those of final and initial states,  $R_{lm}(r)$  is the radial wave function,  $Y_{lm}(\theta, \phi)$  is the spherical harmonic,  $n$  is principal quantum number,  $l$  is azimuthal quantum number,  $m$  is magnetic quantum number, and  $\hat{\mathbf{r}}$  is the unit vector in the radial direction, respectively.  $\hat{\mathbf{e}} \cdot \hat{\mathbf{r}}$  can be rewritten to the spherical harmonic form, as expressed by:

$$\begin{aligned} \hat{\mathbf{e}} \cdot \hat{\mathbf{r}} &= \epsilon_x \sin \theta \cos \phi + \epsilon_y \sin \theta \sin \phi + \epsilon_z \cos \theta \\ &= \frac{4\pi}{3} \left( \epsilon_z Y_{10} + \frac{-\epsilon_x + i\epsilon_y}{\sqrt{2}} Y_{11} + \frac{\epsilon_x + i\epsilon_y}{\sqrt{2}} Y_{1-1} \right). \end{aligned} \quad (4.3)$$

And the spectral weight can be expressed by:

$$\begin{aligned} \Gamma_{\text{tot}} &= \frac{e^2 (E_i - E_n)}{2\pi\hbar^2 m^2 c^3} \sum_{\lambda} \int d\Omega_{\gamma} \left| \sqrt{\frac{4\pi}{3}} \int_0^{\infty} r^3 dr R_{n_n l_n}^* R_{n_i l_i} \int d\Omega Y_{l_n m_n}^* \right. \\ &\quad \left. \left( \epsilon_z Y_{10} + \frac{-\epsilon_x + i\epsilon_y}{\sqrt{2}} Y_{11} + \frac{\epsilon_x + i\epsilon_y}{\sqrt{2}} Y_{1-1} \right) Y_{l_i m_i} \right|^2, \end{aligned} \quad (4.4)$$

where

$$\begin{aligned}
& \int d\Omega Y_{l_n m_n}^* \left( \epsilon_z Y_{10} + \frac{-\epsilon_x + i\epsilon_y}{\sqrt{2}} Y_{11} + \frac{\epsilon_x + i\epsilon_y}{\sqrt{2}} Y_{1-1} \right) Y_{l_i m_i} \\
&= \sqrt{\frac{2l_i + 1}{2l_n + 1}} \langle l_n 0 | l_i 100 \rangle \left( \epsilon_z \langle l_n m_n | l_i 1 m_i 0 \rangle + \frac{-\epsilon_x + i\epsilon_y}{\sqrt{2}} \langle l_n m_n | l_i 1 m_i 1 \rangle + \right. \\
& \quad \left. \frac{\epsilon_x + i\epsilon_y}{\sqrt{2}} \langle l_n m_n | l_i 1 m_i - 1 \rangle \right), \tag{4.5}
\end{aligned}$$

where  $|l_i - l_n| = \Delta l = 0, \pm 1$ , which is selection rules.

As the final state in ARPES experiment is plane wave,  $\phi_n = \exp(i\mathbf{k}_f \cdot \mathbf{r})$ , where  $\mathbf{k}_f$  is the momentum of the final state of the electron. The spectral weight can also be expressed by:

$$\begin{aligned}
\Gamma_{\text{tot}} &= \frac{e^2 (E_i - E_n)}{2\pi \hbar^2 m^2 c^3} \sum_{\lambda} \int d\Omega_{\gamma} \left| \sqrt{\frac{4\pi}{3}} \int_0^{\infty} r^3 dr e^{-i\mathbf{k}_f \cdot \mathbf{r}} R_{n_i l_i} \right. \\
& \quad \left. \int d\Omega \left( \epsilon_z Y_{10} + \frac{-\epsilon_x + i\epsilon_y}{\sqrt{2}} Y_{11} + \frac{\epsilon_x + i\epsilon_y}{\sqrt{2}} Y_{1-1} \right) Y_{l_i m_i} \right|^2, \tag{4.6}
\end{aligned}$$

## 4.2 Polarization dependent photoemission response deduced from theoretical and experimental studies

Orbital character of bands in iron-based superconductors have been investigated by a series of experimental [69] and theoretical studies [67]. Results of the experiments do not necessarily agree with each other as mentioned in section 2.3.2. To solve this problem, calculation of detailed polarization dependent photoemission response was carried out employing the conditions used in the experiments.

### 4.2.1 Experimental measured and theoretical calculated spectra using linearly polarized light

In Fig. 4.1, we present the experimental and calculated results of spectra and polarization dependent photoemission response of different orbitals, in which  $x$ ,  $y$ , and  $z$  defined as shown in Fig. 2.9(a) and Fig. 3.9(a). We performed the experiments at BL28A of PF using  $p$  linearly polarized light, as defined in Fig. 2.11(c), with a photon energy  $h\nu = 40$  eV, by which one can probe the  $k_z = \pi$  plane of  $\text{BaFe}_2(\text{As}_{1-x}\text{P}_x)_2$ . Since the spectral weight of each orbital is not known, the relative weight of orbitals in the calculation is important, and the spectral weight should not be compared between different orbitals. Employing the electric dipole approximation and selection rules, the photoemission intensities of various orbitals in the periodic lattice structure was calculated.

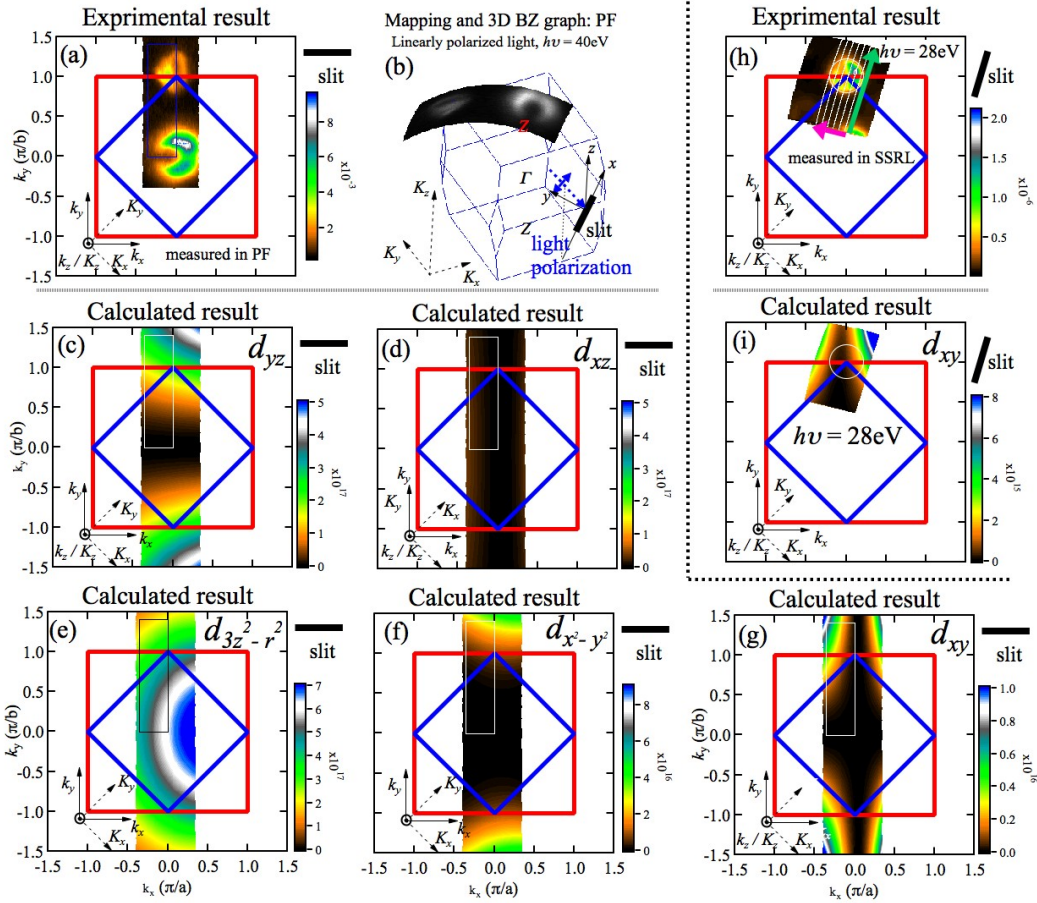


Figure 4.1: Experimental and calculated spectra: (a) Fermi surface near  $k_z = \pi$  ( $Z$  point) of  $\text{BaFe}_2(\text{As}_{1-x}\text{P}_x)_2$  ( $x = 0.38$ ) detected by  $p$  linearly polarized light with a  $h\nu = 40$  eV measured in BL28A of PF; the location of (a) in the Brillouin zone is shown in (b) from top view along the  $k_z$  direction; (c)-(g) are calculated spectra of polarization dependent photoemission response considering various  $3d$  orbitals: (c)  $d_{yz}$ , (d)  $d_{xz}$ , (e)  $d_{3z^2-r^2}$ , (f)  $d_{x^2-y^2}$ , and (g)  $d_{xy}$ , respectively, under the same condition with (a); (h) Fermi surface near  $k_z = 0$  ( $\Gamma$  point) of  $\text{BaFe}_2(\text{As}_{1-x}\text{P}_x)_2$  ( $x = 0.3$ ) measured at BL5-4 of SSRL and using photon energy of 18 eV; (i) calculated spectra of polarization dependent photoemission response of  $d_{xy}$  orbital under the same condition with (h).

### (i) Analysis of orbital character of the inner electron Fermi surfaces

The orbital character of the inner electron Fermi surface of the  $\text{BaFe}(\text{As}_{1-x}\text{P}_x)_2$  superconductor should be  $d_{xz}/d_{yz}$  orbitals as mentioned in section 2.3.2 [63] [69]. As shown in Fig. 4.1(a), in  $\text{BaFe}_2(\text{As}_{1-x}\text{P}_x)_2$  ( $x = 0.38$ ), the spectral intensity of the inner electron Fermi surface is weak on the two edges, indicating the existence of  $d_{xy}$  orbit; and the intensity has no significant variation around the middle part of the inner electron pocket, where the  $d_{yz}$  orbital is predominant, as shown in schematic diagram of Fig. 4.2(a). In another word, being observed by  $p$  linearly polarized

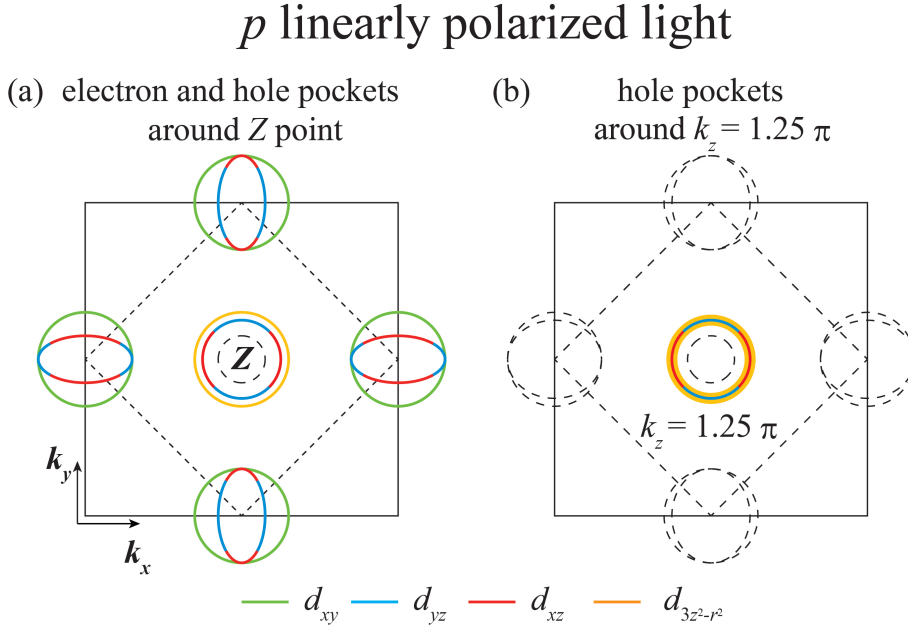


Figure 4.2: Schematic diagram of the orbital character of the (a) electron Fermi surfaces and hole Fermi surfaces around  $Z$  point ( $k_z = \pi$ ); and the (b) hole Fermi surfaces around  $k_z = 1.25\pi$  detected by  $p$  linearly polarized light with  $h\nu \approx 40$  eV; green, blue, red, and orange in the figure denote the  $d_{xy}$ ,  $d_{yz}$ ,  $d_{xz}$ , and  $d_{3z^2-r^2}$  orbitals, respectively.

light, the orbital character of the inner electron Fermi surface in  $\text{BaFe}_2(\text{As}_{1-x}\text{P}_x)_2$  ( $d_{yz}$  and  $d_{xz}$  around the middle and edges, respectively) is different from the experimental results on  $\text{Ba}(\text{Fe}_{1-x}\text{Co}_x)_2\text{As}_2$  [69] and theoretical results [68] [67] ( $d_{xz}$  and  $d_{yz}$  around the middle and edges, respectively) as described in section 2.3.2.

**(ii) Analysis of the orbital characters of the outer electron Fermi surfaces**

Given that  $d_{3z^2-r^2}$  orbital in Fig. 4.1(e),  $d_{x^2-y^2}$  orbital in Fig. 4.1(f), and  $d_{xy}$  orbital in Fig. 4.1(g), are candidates for the outer electron pocket, as shown in Fig. 2.20(a), (b) and Fig. 2.11(d), it is necessary to consider possible combinations of the three orbitals.

The spectral intensity of the outer electron Fermi surface in Fig. 4.1(a) is very weak in the right upper part, but intense in the left lower part, which does not correspond to the  $d_{x^2-y^2}$  orbital. In addition, the outer electron Fermi surface also cannot be observed on line  $(0,0)-(\pi,0)$ , as shown in Fig. 4.1(a), which does not correspond to the  $d_{3z^2-r^2}$  orbital. The calculation result of the  $d_{xy}$  orbital is weak at the upper and lower part at point  $(0,\pi)$  and weak at point  $(\pi,0)$ , indicating great consistency with the experimental results. The  $d_{3z^2-r^2}$  and the  $d_{x^2-y^2}$  orbitals are too weak to be observed or even absent. And besides, the experimental spectrum in Fig. 4.1(h) is also consistent with the  $d_{xy}$  orbital. The experimental spectrum is measured at BL5-4 of SSRL and using photon energy of 18 eV, which is around the  $(0,\pi)$  point and about  $20^\circ$  rotated. Calculated  $d_{xy}$  orbital photoemission response spectrum (e) is consistent with the experimental result in which the right part of the outer electron Fermi surface exhibits a strong spectral intensity around the  $(0, \pi)$  point.

In short, the orbital structure of the electron Fermi surfaces of  $\text{BaFe}_2(\text{As}_{1-x}\text{P}_x)_2$  is very similar to the theoretical results mentioned in section 2.3.2 [68] [67]; but  $d_{xz}$  orbital and  $d_{yz}$  orbital in the inner electron Fermi surface is precisely the opposite, when detected by a  $p$  linearly polarized light.

**(iii) Analysis of the orbital characters of the hole pockets**

It is difficult to make a definite conclusion on the orbital character on the hole Fermi surface here, because bands on the hole Fermi surfaces are not well separated as the bands on the electron Fermi surfaces do.

The spectrum measured with the photon energy of 40 eV is illustrated in Fig. 4.1(a) and (b); on the hole Fermi surface the value of  $k_z$  has slight deviation from  $Z$  point. Therefore, both  $d_{3z^2-r^2}$  and  $d_{xz}/d_{yz}$  are possible candidates. Comparing the spectral intensity on the hole Fermi surface in Fig. 4.1(a) and the calculated spectrum Fig. 4.1(e) and Fig. 4.1(c)/(d), one can recognize that the experimental spectrum corresponds to the  $d_{3z^2-r^2}$  orbital shown in Fig. 4.1(e) the schematic diagram of which is given in Fig. 4.2(b). There are a big notch and a small notch on the left and right hole Fermi surface, respectively, which does not correspond to the  $d_{3z^2-r^2}$  orbital in Fig. 4.1(e) very well. Similar to the last subsection,  $d_{xy}/d_{yz}$  orbital is also a candidate of the middle hole Fermi surface around the  $Z$  point; the  $d_{yz}$  orbital can be observed on the upper and lower part of the hole Fermi surface

and the  $d_{xz}$  orbital exists cannot be observed on the left and right parts on the middle hole pocket. In addition, it is noticed that in Fig. 4.1(a) the intensity of the  $d_{3z^2-r^2}$  orbital varies with momentum; the left part is weak while the right part is strong; which exactly corresponds to the calculated  $d_{xy}/d_{yz}$  and  $d_{3z^2-r^2}$  orbital, as shown in Fig. 4.2(b).

### 4.3 Method of spectral analysis

We will introduce the photoemission spectrum of  $\text{BaFe}_2(\text{As}_{1-x}\text{P}_x)_2$  ( $x = 0.38$ ) detected by circularly polarized light with photon energy of 40 eV here.

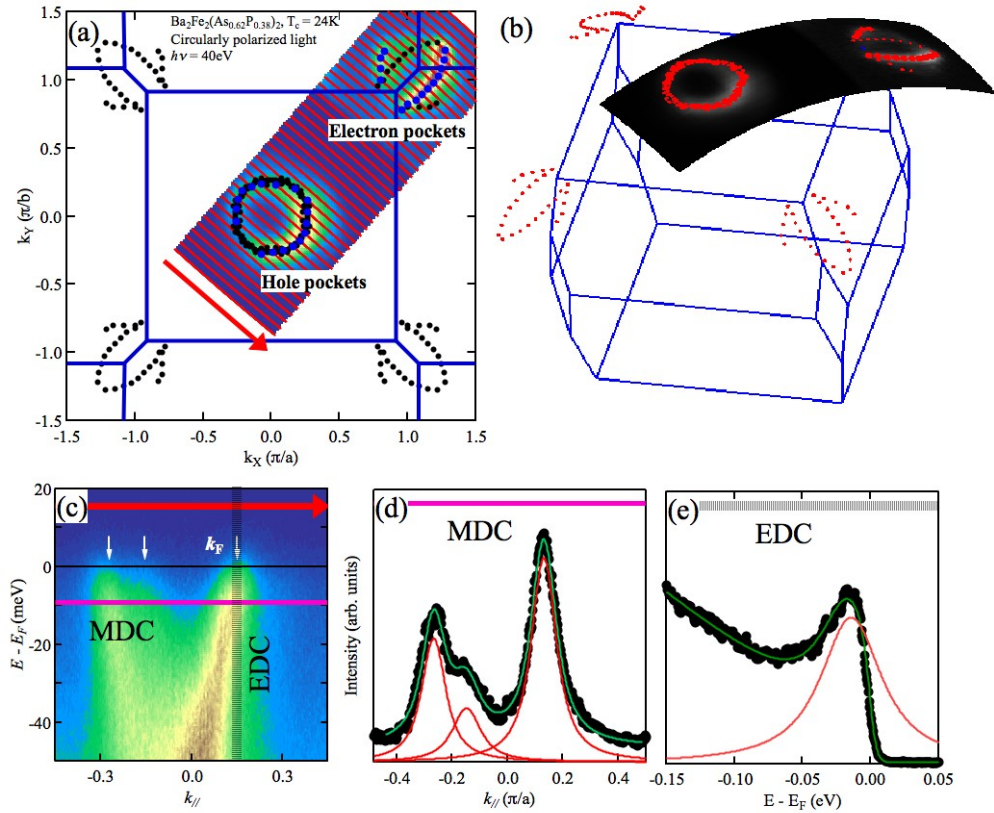


Figure 4.3: Mapping graph of the (a) two- and (b) three-dimensional Fermi surface in the Brillion zone; (c)  $E$ - $k_{||}$  plot of spectrum; Lorenz fitting results of (d) MDC and (e)EDC, respectively.

Fig. 4.3(a) shows the two-dimensional mapping Fermi surface of hole and electron Fermi surfaces in the Brillouin zone of  $\text{BaFe}_2(\text{As}_{1-x}\text{P}_x)_2$  ( $x = 0.38$ ) detected by circularly polarized light with photon energy of 40 eV. In which, the

blue line is the Brillouin zone, red lines are all the cuts, blue points are  $k_{FS}$ , and black points are symmetrized  $k_{FS}$ . Figure 4.3 (b) is the Fermi surface from the mapping of 3D Brillouin zone, respectively; larger red points denote  $k_F$  while smaller red points are symmetrized  $k_F$ .

Figure 4.3 (c) shows the energy-momentum plot of one selected electron surface, in which the position of  $k_F$  is marked by the white arrow. The curves horizontally extracted from photoemission spectra at fixed energies are momentum distribution curves (MDCs). The MDCs along the pink solid line and the black dotted line can be seen in Fig. 4.3 (c) and Fig. 4.3 (d), respectively. Each MDC was fitted using the convolution of superimposed Lorenz functions and Gaussian function, as expressed below:

$$\begin{aligned} h(x) &= \int_{-\infty}^{+\infty} f(x')g(x-x')dx' + bg. \\ &= \int_{-\infty}^{+\infty} dx' \sum_i \frac{A_i}{(x' - x'_{0i})^2 + B_i} \exp \left[ -\frac{(x-x')^2}{2\sigma^2} \right] + bg., \end{aligned} \quad (4.7)$$

where  $x'_{0i}$  is the position of the  $i$ th peak in MDC, and  $2\sigma\sqrt{2\ln 2}$  is the full width at half maximum (FWHM), constant  $bg.$  is the background. In Fig. 4.3 (d), the horizontal axis is the momentum  $k_{\parallel}$  parallel to the  $k_x$ - $k_y$  Fermi surface and vertical axis is the intensity; black points are measured datapoints in MDC, and green line is the fitting result using Eq. 4.7, red lines are the Lorenz functions that synthesize the green line. As seen in Fig. 4.3 (d), the fitting turns to be successful.

The vertically extracted ones at fixed momentums are energy distribution curves (EDCs). The EDCs along the black dash line and the black dotted line can be seen in Fig. 4.3 (c) and Fig. 4.3 (e), respectively. Each EDC was fitted using the similar procedure for MDC, except that a Fermi-Dirac distribution term was multiplied and that a different background was obtained, which included a constant and a quadratic term, as:

$$\begin{aligned} h(\epsilon') &= \int_{-\infty}^{+\infty} F(\epsilon)f(\epsilon')g(\epsilon-\epsilon')d\epsilon' + bg. \\ &= \int_{-\infty}^{+\infty} \sum_i \frac{1}{e^{(\epsilon'-\mu)/kT} + 1} \cdot \frac{A_i}{(\epsilon' - \epsilon'_{0i})^2 + B_i} \exp \left[ -\frac{(x-\epsilon')^2}{2\sigma^2} \right] d\epsilon' + bg., \end{aligned} \quad (4.8)$$

where  $k$  is Boltzmann coefficient,  $T$  is absolute temperature (thermodynamic temperature). The obtained peaks in the Lorenz functions are the band. Figure 4.3 (e) is similar to Fig. 4.3(d), but it is EDC with an energy horizontal axis, and fitted by Eq. 4.8.

The photoemission intensities taken along the momentum cuts mentioned in Fig. 4.3(a) on the electron Fermi surface with 40 eV photons in Fig. 4.4. Each cut in

4.4(b)-(l) is along the red arrow shown in each figure as well as in 4.4(a), while cut 1 to cut 11 follow the order marked by the white arrow. The red points in 4.4(b)-(l) denote the obtained positions of Lorentz functions after fitting all the MDCs using Eq. XX, exhibiting the band structure observed in the spectrum. The cross of band and Fermi surface ( $E_F = 0$ ) is  $k_F$ , as marked by solid points in 4.4(a). As illustrated in 4.4(c) and 4.4(e), we performed the gap analysis of EDCs at  $k_F$ .

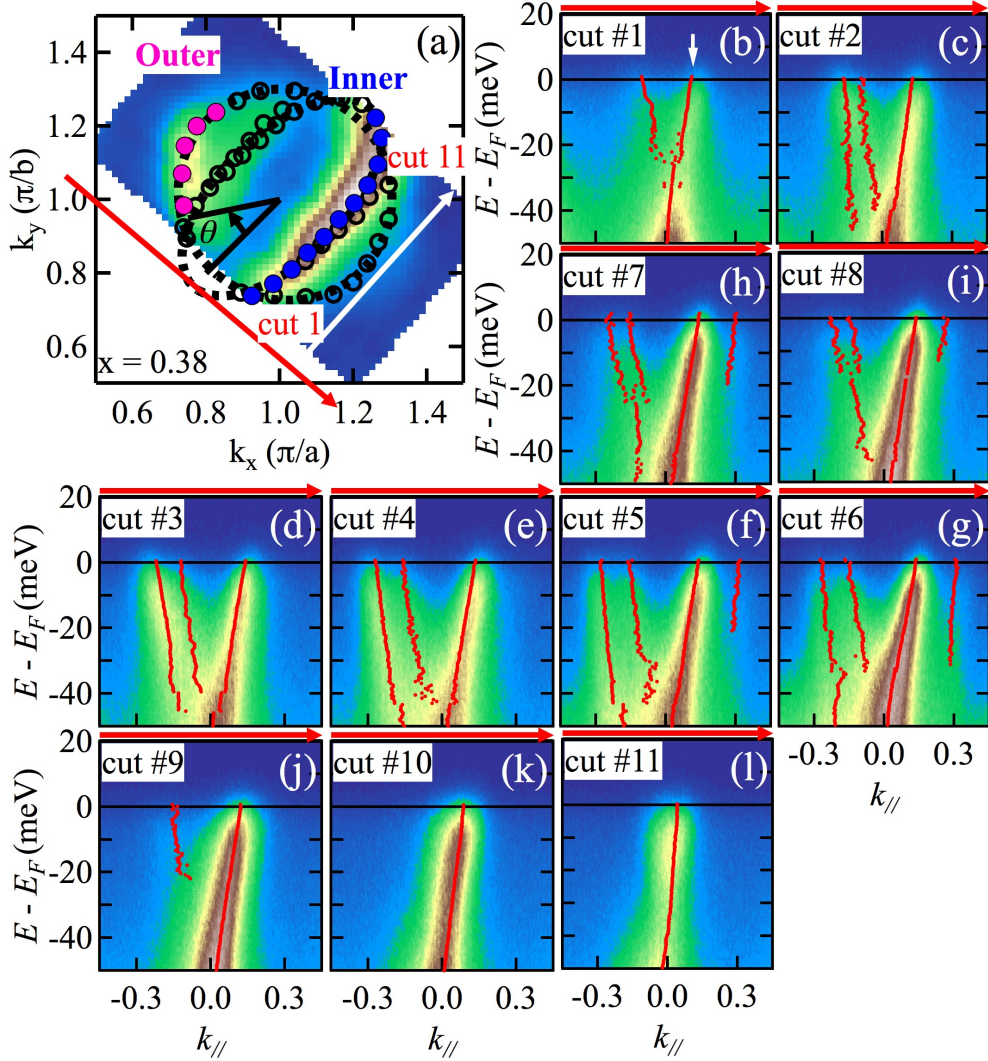


Figure 4.4: (a) mapping graph of the Fermi surface and (b)-(l) each spectral cuts in Fig. (a). Red points in (b)-(c) are fitting results of the MDCs.

## 4.4 Method of gap estimation

In the spectrum we can obtain the band-Fermi surface crosses  $k_F$ , which are momenta on the Fermi surface. Then the gap analysis can be performed using the energy distribution curves (EDCs) at  $k_F$ .

The EDCs at  $k_F$  point can be expressed by the following formula:

$$A(\mathbf{k}_F, \omega) = -\frac{1}{\pi} \text{Im}G(\mathbf{k}_F, \omega) = -\frac{1}{\pi} \text{Im} \frac{1}{\omega - \Sigma(\mathbf{k}_F, \omega)}, \quad (4.9)$$

where  $\Sigma(\mathbf{k}_F, \omega)$  is the self-energy [105], which can be expressed by:

$$\Sigma(\mathbf{k}_F, \omega) = -i\Gamma_1 + \frac{\Delta^2}{\omega + i\Gamma_0}, \quad (4.10)$$

where  $\Gamma_1$  is the single-particle scattering rate, and  $\Gamma_0$  is the inverse pair lifetime determined by  $\Gamma_0(T) = 8(T - T_c)/\pi$ , which turns to zero when temperature is lower than the critical temperature  $T_c$ ,  $\Gamma_0 = 0$  when  $T < T_c$ .

Symmetrized spectra can be fitted to the convolution of Eq. 4.9 and Gaussian resolution function, as expressed by

$$\text{Sym. EDC} = \int_{-\infty}^{+\infty} d\omega' \frac{1}{\sigma\sqrt{2\pi}} \exp \left[ -\frac{(\omega - \omega')^2}{2\sigma^2} \right] A(\mathbf{k}_F, \omega') + bg., \quad (4.11)$$

where  $bg.$  is the background including a constant and a quadratic term. Figure 4.5 is one example of symmetrized EDCs and the fitting results below and above  $T_c$ , respectively. In photoemission experiments the energy resolution, full width at half maximum (FWHM), can be derived to be  $2\sigma\sqrt{2\ln 2}$ .

Sometimes, a large background can be a problem, which may result in inaccurate fitting; some uncorrelated bands below yet close to the  $k_F$  may lead to the appearance of certain fake structure (resembles the pseudogap structure) in the symmetrized EDCs near the Fermi level. Besides, the pseudogap will bring about a consequence that the pairing order parameter  $|\Delta|$  determined in the fitting cannot reflect the superconducting gap size. For solving those problems, the superconducting information is extracted by subtracting the high temperature EDC ( $T > T_c$ ) from low temperature EDC ( $T < T_c$ ). Then, the subtracted spectrum can be fitted using

$$\text{Sub. EDC} = \text{Sym. EDC} (T < T_c) - \text{Sym. EDC} (T > T_c), \quad (4.12)$$

in which the fitting equation EDC is given by Eq. 4.11. Detailed fitting results will be presented in section 5.2.

We fit the gap size vs Fermi surface angle  $\theta$  by

$$\Delta(\theta) = A + B\cos(2\theta) + C\cos(4\theta), \quad (4.13)$$

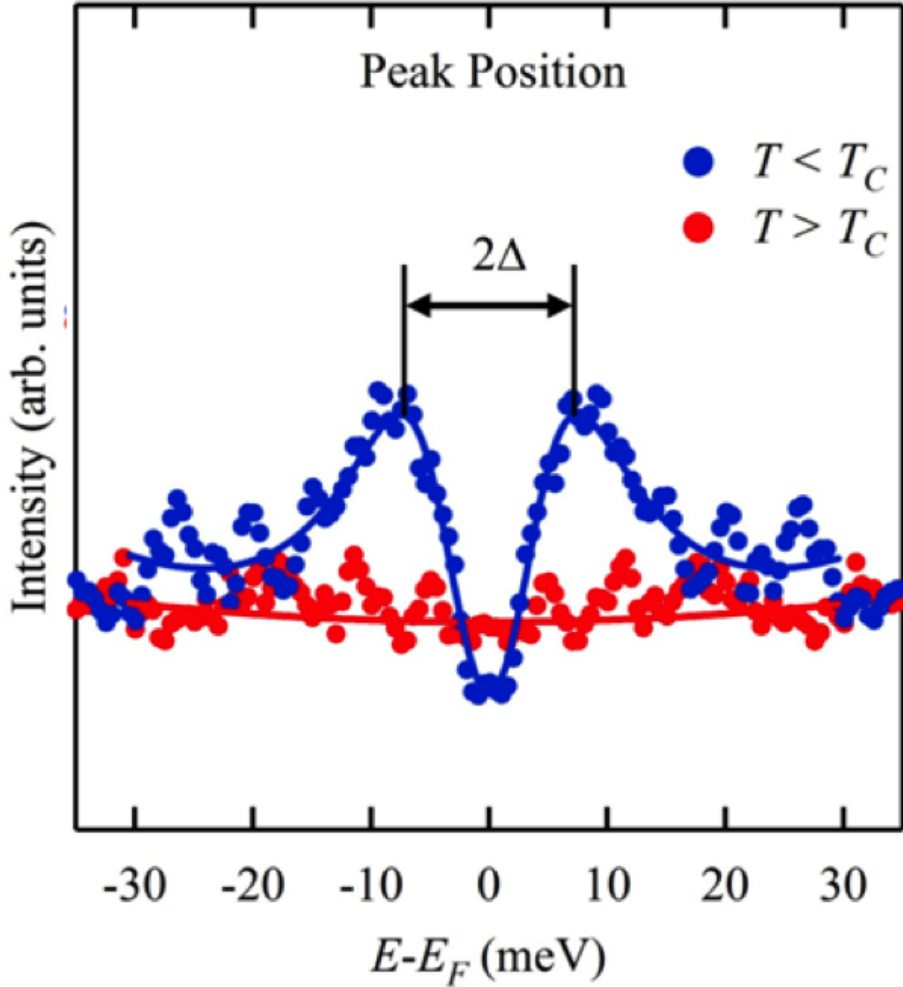


Figure 4.5: Measured symmetrized EDCs at the temperature over (red points) and below (blue points)  $T_c$ , respectively; solid lines are fitting results using Eq. 4.11.

where A, B, and C are parameters of average value, two- and four-fold anisotropic of superconducting gap, respectively. And estimate the anisotropic of superconducting symmetry quantitatively by those parameters.

## 4.5 Summary

In this chapter, we presented the electric dipole approximation and selection rules, which are usually employed to analyze the electron orbital properties in ARPES

experiments along with the symmetry. We also presented the method of spectral analysis and gap estimation.

Since in most of ARPES experiments the photoelectrons are detected by rotating the specimens, the required deflection angle to measure the electron surfaces is quite large when the photon energy is not significantly high, which results in the deviation of the incident light from the symmetry plane. Consequently, the analysis of symmetry based on such results could lack rigour. Thus, we numerically calculated the photoemission spectroscopy of different electron orbitals, and carried out experiments at PF and SSRL as well as theoretical calculation. The main results are as follows:

(1) Theoretically available photoemission spectra were calculated.

(2) Through comparison between calculated spectra and detected ones, the experimental measured spectra of  $\text{BaFe}_2(\text{As}_{1-x}\text{P}_x)_2$  were analyzed and possible corresponding electronic orbitals were determined.  $d_{xz}/d_{yz}$  orbital and  $d_{xy}$  orbital correspond to the inner and outer electron Fermi surface, respectively;  $d_{z^2}$  and  $d_{xz}/d_{yz}$  orbital on the hole Fermi surface near the  $Z$  point in the Brillouin zone; and  $d_{xz}/d_{yz}$  orbital on the hole Fermi surface near the  $\Gamma$  point in the Brillouin zone in the  $\text{BaFe}_2(\text{As}_{1-x}\text{P}_x)_2$  ( $x = 0.38$ ).

(3) Orbital character of bands in iron-based superconductors can be analyzed by polarization dependent photoemission response. The  $d_{xz}/d_{yz}$  and the  $d_{xy}$  orbitals are on the inner electron and outer Fermi surface, respectively.



# Chapter 5

## Superconducting gap

### 5.1 Introduction

Since 2008 until now, a series of iron-based superconductors have been discovered, and a number of theoretical and experimental works have made progress. However, the pairing mechanism still remains controversial. Complex structures of Fermi surfaces (FSs) and superconducting gaps have been reported for those iron-based superconductors. Amounts of NMR Knight-shift experiments [25, 106–111] indicated that a number of iron-based superconductors have spin-singlet pairing and various gap symmetries such as  $s_{++}$ -wave,  $s_{\pm}$ -wave [112] and  $d$ -wave pairing has been proposed. ARPES experiment [113] and LDA+DMFT calculation [114] of LiFeAs suggested nodeless superconducting gap on the hole and electron FSs. Penetration depth experiments on SmFeAsO $_{1-x}$ F $_x$  [115] and Ba(Fe $_{0.93}$ Co $_{0.07}$ ) $_2$ As $_2$  [116] indicate nodeless gap. On the other hand, penetration depth experiments and thermal conductivity measurements on P-doped Ba122 [81], LaOFeP [76] [77] [78] and KFe $_2$ As $_2$  [84] indicated line nodes in the superconducting gap or gap minima. Theoretical studies which consider spin fluctuations suggested that larger Pn-Fe-Pn band angle lead to anisotropic [117].

Different from cuprate superconductors which have a universal  $d$ -wave pairing symmetry  $\Delta_{\mathbf{k}} \propto \cos k_x - \cos k_y$ ,  $\mathbf{k}$  is momentum on the Fermi surface, iron-based superconductors exhibit complex pairing mechanism. Several kinds of pairing were proposed, such as  $s_{\pm}$ -wave, nodal  $s_{\pm}$ -wave,  $s + id$ -wave pairing and so on.  $S_{\pm}$ -wave pairing gives fully gapped order parameter with opposite sign between hole and electron FSs. Another pairing which looks similar to  $s_{\pm}$ -wave pairing, called nodal  $s_{\pm}$ -wave pairing, nodes on electron FSs was also suggested. A time-reversal symmetry breaking state called  $s + id$  pairing state, which focus on the competition between  $s_{\pm}$ -wave and  $d_{x^2-y^2}$ -wave [118], is also a novel candidate for intricate pairing mechanism on iron-based superconductivity.

The iron-based superconductor BaFe $_2$ (As $_{1-x}$ P $_x$ ) $_2$  has attracted much attention

since the presence of superconducting gap nodes, which was introduced in section 2.4.1.

As properties of iron-based superconductors are sensitive to doping, detailed research on simple samples is necessary. Isovalent doping, which provides chemical pressure in materials and slightly modulating the structure parameter, is beneficial for understanding and exploring the physical properties of materials. Phosphorus doping  $\text{BaFe}_2\text{As}_2$  is one example of isovalent doping, which changes the pnictogen height from the Fe-Fe plane [99] and gives a highest  $T_c = 30$  K in optimal doping stoichiometric ratio. We studied the superconducting gap structure on the electron Fermi surface in  $\text{BaFe}_2(\text{As}_{1-x}\text{P}_x)_2$  via ARPES. ARPES experiment is a powerful experimental method, which can be used to observe the superconducting gap on the  $k_F$  straightly. The ARPES result and related analysis will be presented in the following sections.

## 5.2 Experimental results of ARPES

As mentioned in subsection 2.3.1, different superconducting gap structures were reported by Zhang *et al.* [87] and Yoshida *et al.* [88]; therefore, further confirmation is necessary for solving the problem. We systematically measured the superconducting gaps in  $\text{BaFe}_2(\text{As}_{1-x}\text{P}_x)_2$  with different doping concentrations ( $x = 0.3, 0.34, 0.38$  and  $0.45$ ) by ARPES. Physical properties of  $\text{BaFe}_2(\text{As}_{1-x}\text{P}_x)_2$  were introduced in section 2.5. Experiments were carried out at BL28A of PF and BL5-4 of SSRL which were introduced in chapter 3.2. We will estimate the gap sizes using Norman function which was introduced in section 4.4.

### 5.2.1 $k_z$ mapping on the Fermi surfaces

Because of the great disparity of spectrum intensities detected under different photon energies, in order to observe obvious band structure, when performing the mapping the MDC intensities under different photon energies were normalized so as to obtain the Fermi surface mapping images with various  $k_z$  crossing the center of BZ, as shown in Fig.5.1.

### 5.2.2 Superconducting gap on the electron Fermi surfaces

In this subsection we present the superconducting gap on the electron Fermi surface in  $\text{BaFe}_2(\text{As}_{1-x}\text{P}_x)_2$  with different doping concentrations ( $x = 0.3, 0.34, 0.38$ , and  $0.45$ ) measured by ARPES.

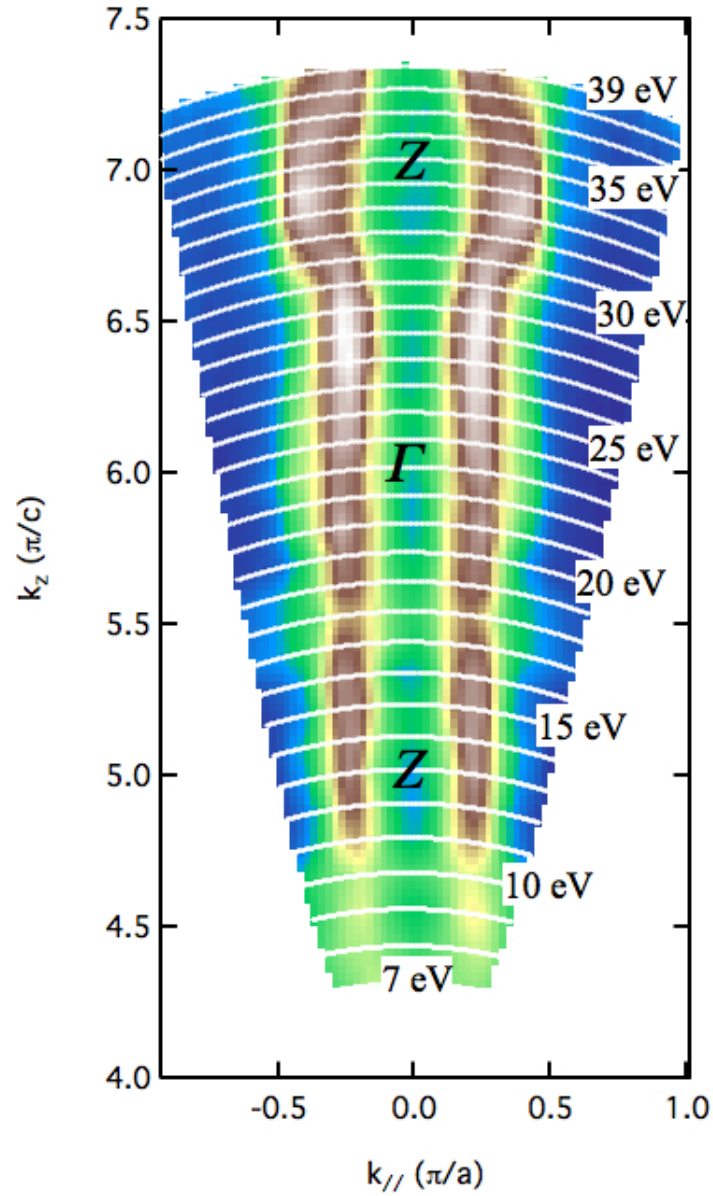


Figure 5.1:  $k_z$  mapping of  $\text{BaFe}_2(\text{As}_{1-x}\text{P}_x)_2$  ( $x = 0.38$ ) measured using photon energies from 7 eV to 39 eV with inner potential  $V_0 = 14\text{eV}$ .

**(i)  $x = 0.3$** 

The electron surface of the sample with  $x = 0.3$  is measured at BL5-4 of SSRL. The employed photon energy was 28 eV with which one can detect the electron Fermi surface on the  $\Gamma$  plane instead of the those on the  $Z$  plane, as shown in Fig. 5.2. Different from the other experimental conditions, the spectra on the outer electron Fermi surfaces can be observed this experimental condition because of the polarization dependent photoemission response, as mentioned in section 4.2. The gap size is shown in Fig. 5.2(b), in which the gap on the outer Fermi surface exhibits the feature of small gap around the center and large gap around the ends. The same procedure was performed to analyze the data of composition  $x = 0.3$  by Yoshida *et al.* [88]. As shown in Fig. 5.3, at  $x = 0.3$ , the gap size is slight larger ( $\approx 10$  meV) than  $x = 0.34$  (Figs. 5.4 and 5.5). Moreover, it seems that the center is larger and two ends are smaller. Since the experiments in Fig. 5.3 ( $x = 0.3$ ) used circularly polarized light with photon energy of 40 eV, the spectrum intensity of outer surface is weak and is insufficient to observe its change.

**(ii)  $x = 0.34$** 

Figures 5.4 and 5.5 are the result of  $\text{BaFe}_2(\text{As}_{1-x}\text{P}_x)_2$  ( $x = 0.34$ ) detected by  $p$  linearly polarized light with photon energy of 40 eV at BL28A of PF. Panel 5.4(a) and 5.5(a) are the electron Fermi surfaces on the Fermi surface for  $k_z = \pi$ . The  $k_F$  on the inner and outer electron Fermi surfaces are marked by blue and red points, respectively. The Fermi angle  $\theta$  is the angle between  $k_F$ - $X$  and  $X$ - $Z$ . EDCs at each  $k_F$  are shown in Figs. 5.4(c), (f) and 5.5(d), (g), (j); the symmetrized EDCs are shown in Figs. 5.4(d), (g) and 5.5(e), (h), (k); the subtracted EDCs are obtained by subtracting the EDCs above  $T_c$  from the ones below  $T_c$ , as shown in Figs. 5.4(e), (h) and 5.5(f), (i), (l). Using the method introduced in section 4.4, the fitting was carried out for the symmetrized (subtracted) EDCs; the obtained value of gap size ( $\Delta$ ) is shown in Fig. 5.4(b) and Fig. 5.5(b)-(c). In the figures, solid blue, red and pink circles are the  $\Delta$  from the fitting of symmetrized EDCs using Eq. 4.11; while open blue, red and pink open squares denote those  $\Delta$  obtained from the fitting of the subtracted EDCs using Eq. 4.12. Also it is noticed that the superconducting gap size of  $\text{BaFe}_2(\text{As}_{0.66}\text{P}_{0.34})_2$  shows fluctuations with Fermi angle  $\theta$ . Blue, red and pink solid and dash lines are the curves obtained from the fitting of the  $\Delta$  from symmetrized and subtracted EDCs using Eq. 4.13. It is found that for the superconducting gap on either the inner or outer electron Fermi surface, the  $\Delta$  deduced using both methods has the same tendency with  $\theta_{k_F}$ . Comparing with Figs. 5.4(b) and 5.5(b), (c), the change of the gap size is rather small, and the gap can be considered slightly anisotropic.

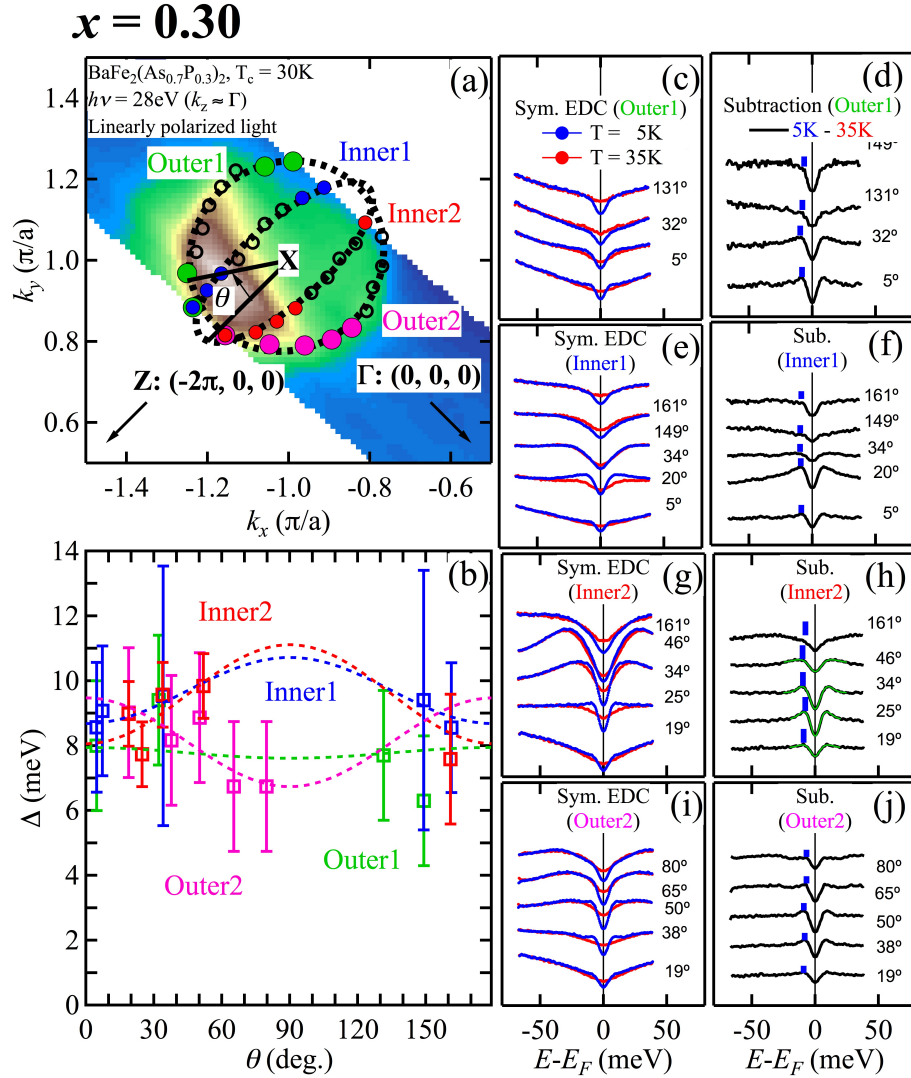


Figure 5.2: (a) Fermi surface mapping of the electron Fermi surface for  $x = 0.30$  taken using linearly light with  $h\nu = 28\text{ eV}$  corresponding to  $k_z = \Gamma$ ; blue, red and yellow, pink filled circles are  $k_F$  points on the inner and outer electron Fermi surfaces, respectively; black open circles are  $k_F$  and symmetrized  $k_F$  on the Fermi surface; (b) gap size vs FS angle for the inner and outer electron Fermi surfaces; Fermi surface angle  $\theta$  is the angle between the X-Z and X- $k_F$  direction; black dashed ellipses are fitting results of  $k_F$  on the inner and outer electron Fermi surfaces, respectively; (c)-(d), (e)-(f), (g)-(h) and (i)-(j) symmetrized EDCs and subtraction of  $T > T_c$  EDCs from  $T < T_c$  EDCs at  $k_F$  points on the inner and outer electron Fermi surfaces; blue sticks mark the gaps size, which have been obtained by fitting the EDCs to the Norman function introduced in section 4.4.

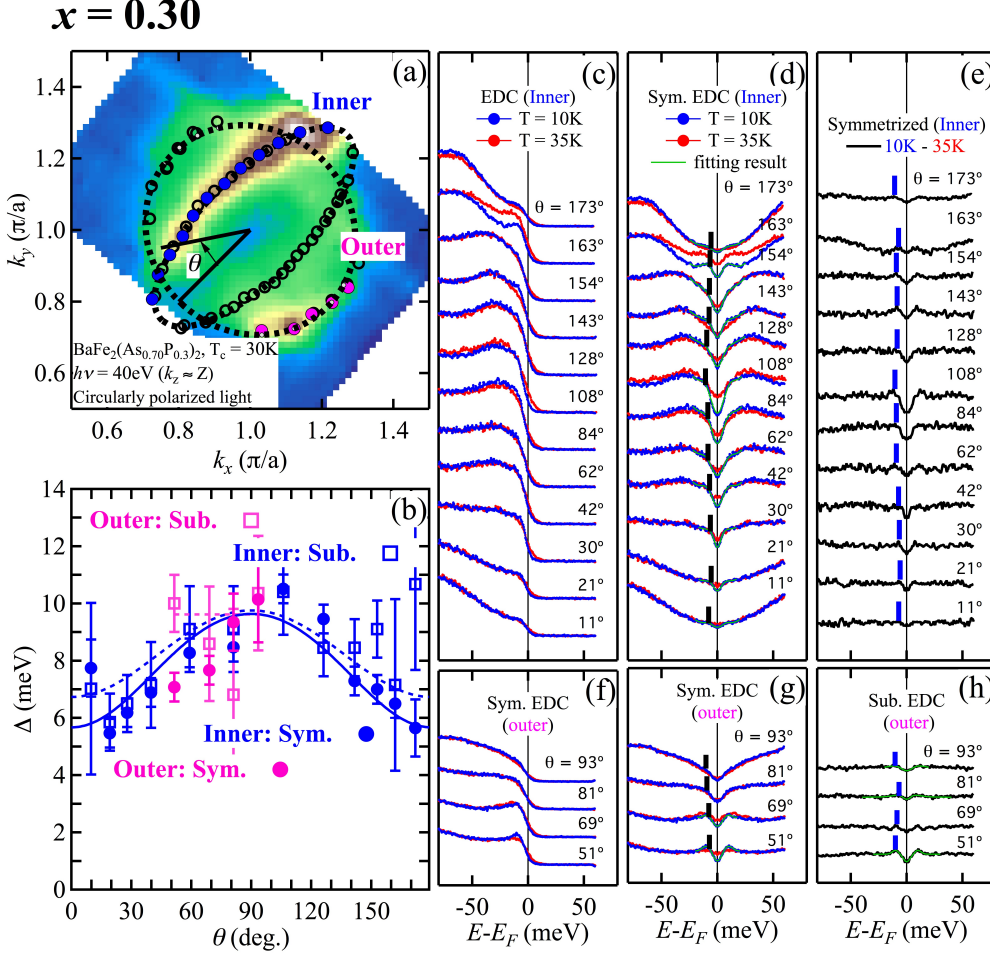


Figure 5.3: (a) Fermi surface mapping of the electron Fermi surface for  $x = 0.30$  taken using right-handed circularly polarized light with  $h\nu = 40$  eV corresponding to  $k_z = Z$ ; blue and pink filled circles are  $k_F$  points on the inner and outer electron Fermi surfaces, respectively; black open circles are  $k_F$  and symmetrized  $k_F$  on the Fermi surface; (b) gap size vs FS angle for the inner and outer electron Fermi surfaces; Fermi surface angle  $\theta$  is the angle between the X-Z and X- $k_F$  direction; black dashed ellipses are fitting results of  $k_F$  on the inner and outer electron Fermi surfaces, respectively; (c)-(e) and (f)-(h) EDCs, symmetrized EDCs, and subtraction of  $T > T_c$  EDCs from  $T < T_c$  EDCs at  $k_F$  points on the inner and outer electron Fermi surfaces; black (blue) sticks mark the gaps size, which have been obtained by fitting the EDCs to the Norman function introduced in section 4.4 [88].

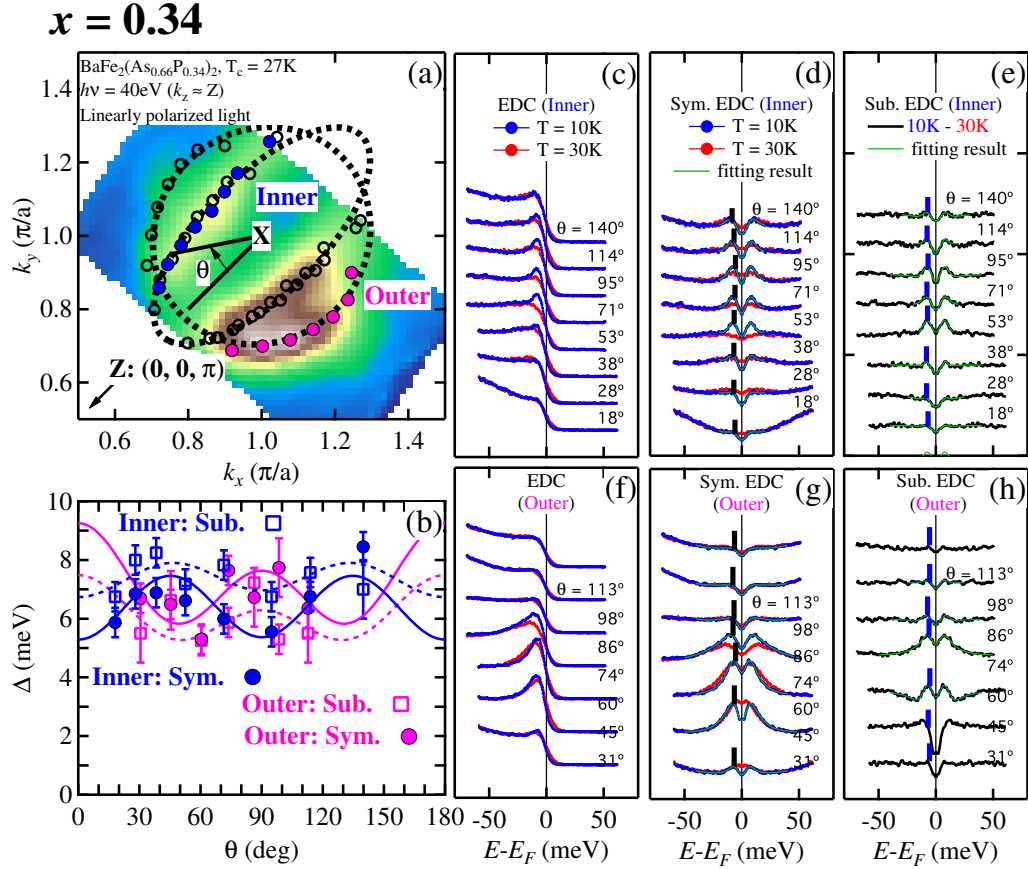


Figure 5.4: (a) Fermi surface mapping of the electron Fermi surface for  $x = 0.34$  taken using linearly polarized light with  $h\nu = 40$  eV corresponding to  $k_z = Z$ ; blue and pink filled circles are  $k_F$  points on the inner and outer electron Fermi surfaces, respectively; black open circles are  $k_F$  and symmetrized  $k_F$  on the Fermi surface; Fermi surface angle  $\theta$  is the angle between the X-Z and X- $k_F$  direction; black dashed ellipses are fitting results of  $k_F$  on the inner and outer electron Fermi surfaces, respectively; (b) gap size vs FS angle of the inner and outer electron Fermi surfaces; (c)-(e) and (f)-(h) EDCs, symmetrized EDCs, and difference EDCs between of  $T > T_c$  and at  $T < T_c$  EDCs at  $k_F$  points on the inner and outer electron Fermi surfaces, respectively; black (blue) sticks mark the gaps size, which have been obtained by fitting the EDCs to the Norman function introduced in section 4.4.

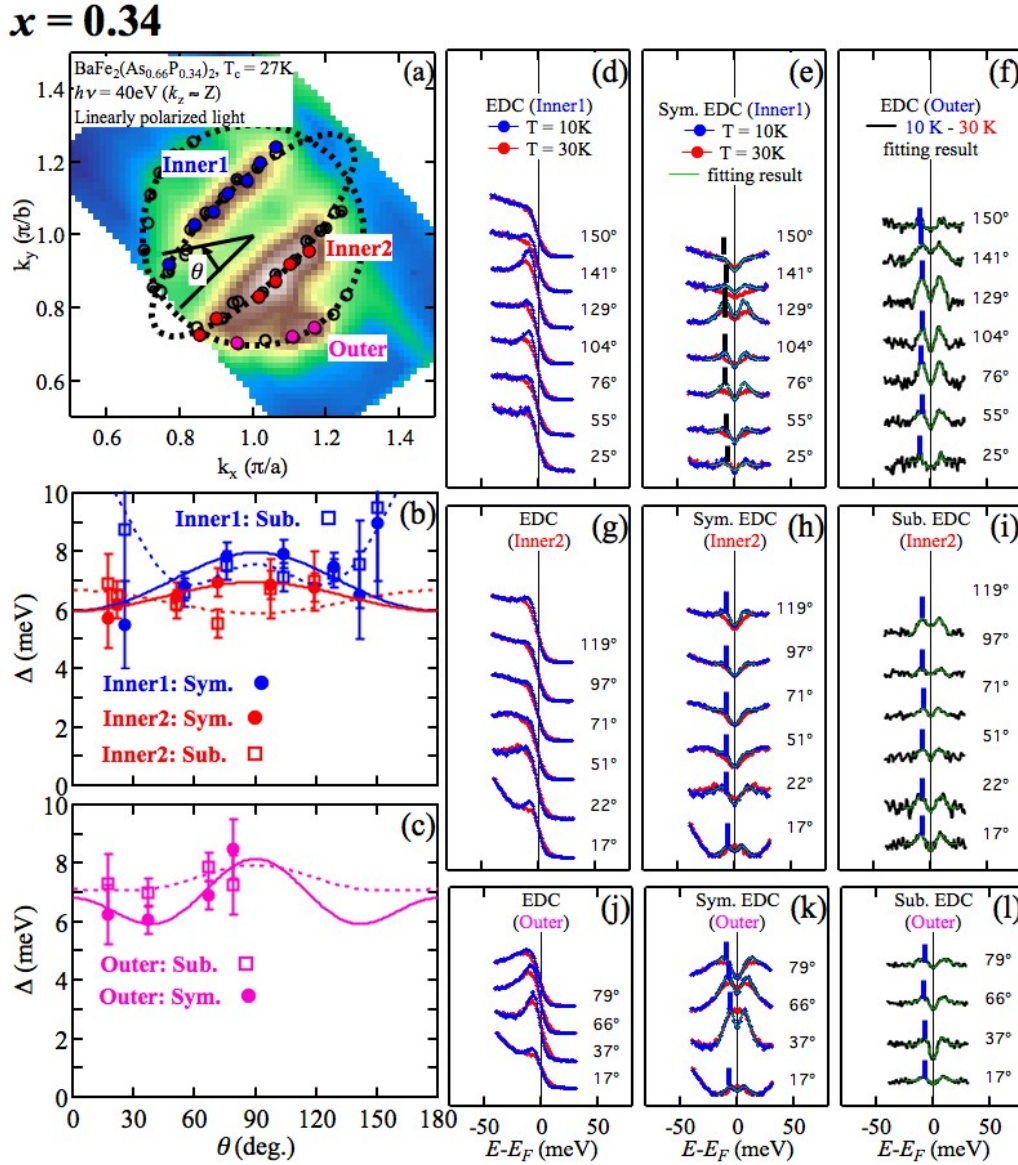


Figure 5.5: (a) Fermi surface mapping of the electron Fermi surface for  $x = 0.34$  taken using linearly polarized light with  $h\nu = 40$  eV corresponding to  $k_z = Z$ ; blue, red and pink filled circles are  $k_F$  points on the inner and outer electron Fermi surfaces, respectively; black open circles are  $k_F$  and symmetrized  $k_F$  on the Fermi surface; Fermi surface angle  $\theta$  is the angle between the X-Z and X- $k_F$  direction; black dashed ellipses are fitting results of  $k_F$  on the inner and outer electron Fermi surfaces, respectively; (b)-(c) gap size vs FS angle of the inner and outer electron Fermi surfaces, respectively; (d)-(f), (g)-(i) and (j)-(l) EDCs, symmetrized EDCs, and difference EDCs between of  $T > T_c$  and at  $T < T_c$  EDCs at  $k_F$  points on the inner and outer electron Fermi surfaces, respectively; black (blue) sticks mark the gaps size, which have been obtained by fitting the EDCs to the Norman function introduced in section 4.4.

**(iii)  $x = 0.38$** 

Figures 5.6-5.8 are the measurement results of  $\text{BaFe}_2(\text{As}_{1-x}\text{P}_x)_2$  samples of the same composition ( $x = 0.38$ ,  $T_c = 24$  K) using photon energy of 40 eV,  $p$  linearly polarized light was used for the results shown in Figs. 5.6- 5.7 while circularly polarized light was employed for the data shown in Fig. 5.8 (the same condition as that in Fig. 5.3 except for the composition). Repeating the analysis method applied to Fig. 5.4, it is found that, as compared with  $\text{BaFe}_2(\text{As}_{0.66}\text{P}_{0.34})_2$  ( $T_c = 27$  K),  $\text{BaFe}_2(\text{As}_{0.62}\text{P}_{0.38})_2$  ( $T_c = 24$  K) exhibits a smaller gap size by about 2 meV. Moreover, the gap on the inner electron Fermi surface in  $\text{BaFe}_2(\text{As}_{0.62}\text{P}_{0.38})_2$  has a feature of a larger gap around the center and a smaller gap at the ends of the ellipsoids; the gap on the outer electron Fermi surface has also a less obvious change with Fermi angle.

It should be noticed that, for the inner electron Fermi surface detected by circularly polarized light, the gap size from the fitting of symmetrized EDCs at  $\theta_{k_F} = 180^\circ$  seems a little too large. Comparison of symmetrized EDCs between above  $T_c$  and below  $T_c$  indicates that the EDCs at 30 K and 10 K did not have much difference. This may be one of the suprious gaps as mentioned in section 4.4 or it also has the possibility of the pseudogap. After subtracting the EDCs above  $T_c$  from the ones below  $T_c$ , the curve is similar to the result detected by  $p$  linearly polarized light, i.e., the inner electron Fermi surface also exhibits a feature of a larger gap around the center and a smaller gap at the ends of the ellipsoids. For the record, all the experiments above were performed at BL28A of PF.

**(iv)  $x = 0.45$** 

We measured the sample  $\text{BaFe}_2(\text{As}_{1-x}\text{P}_x)_2$  ( $x = 0.45$ ,  $T_c = 20$  K), as shown in Fig. 5.9. Because of the low  $T_c$ , we carried out this experiment at lower temperatures at BL5-4 of SSRL, where the temperature can be cooled down to as low as 5 K. We only fitted the subtracted EDCs owing to the relatively larger background in the results. No matter which figure we refer to, the fitting result in Fig. 5.9(b), symmetrized EDC, or subtracted EDC, it is found that the gap on the two ends of the inner electron Fermi surfaces is rather small, and that the symmetrized EDCs and subtracted EDCs all have a small peak, indicating the existence of nodes. Momentum  $k_\perp$  is decreasing when measured  $k_\parallel$  deviate from zero in the ARPES measurements because of the momentum conservation, as mentioned in section 3.1.2. Thus the deviation from the  $k_z = \pi$  ( $Z$  point) plane occurs in the observed spectra on the edges of the electron Fermi surface measured using 18 eV photon energy, as shown in Fig. 5.9(b) and (c). Therefore, although nodal gap structure of  $s_\pm$ -wave pairing mechanism is not observed, it is still possible that the loop node exists at the flat parts of the electron Fermi surface. In addition, the superconducting

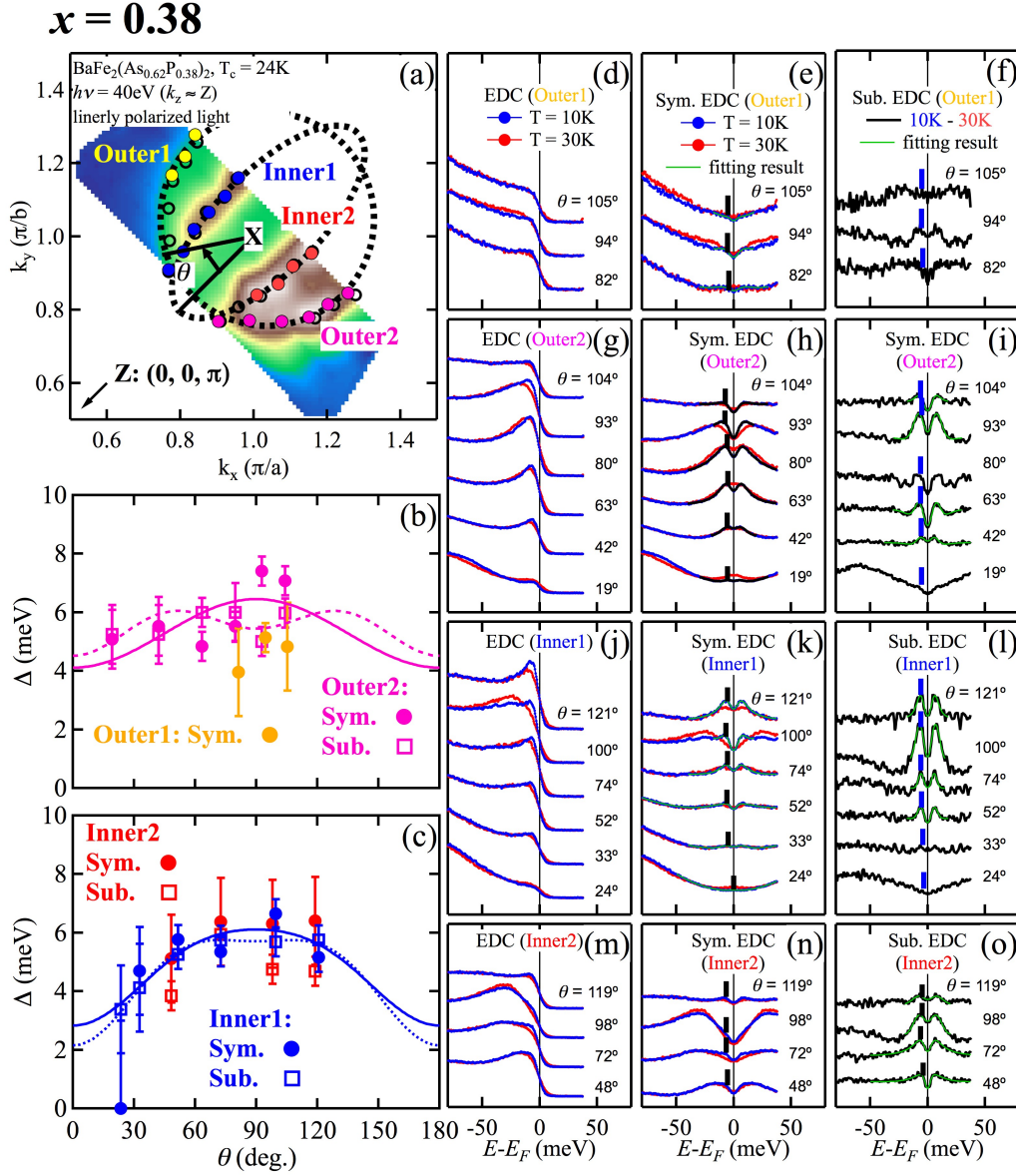


Figure 5.6: (a) Fermi surface mapping of the electron Fermi surface for  $x = 0.38$  taken using linearly polarized light with  $h\nu = 40$  eV corresponding to  $k_z = Z$ ; blue, red and yellow, pink filled circles are  $k_F$  points on the inner and outer electron Fermi surfaces, respectively; black open circles are  $k_F$  and symmetrized  $k_F$  on the Fermi surface; (b) gap size vs FS angle for the inner and outer electron Fermi surfaces; Fermi surface angle  $\theta$  is the angle between the X-Z and X- $k_F$  direction; black dashed ellipses are fitting results of  $k_F$  on the inner and outer electron Fermi surfaces, respectively; (c)-(e) and (f)-(h) EDCs, symmetrized EDCs, and subtraction of  $T > T_c$  EDCs from  $T < T_c$  EDCs at  $k_F$  points on the inner and outer electron Fermi surfaces; black (blue) sticks mark the gaps size, which have been obtained by fitting the EDCs to the Norman function introduced in section 4.4.

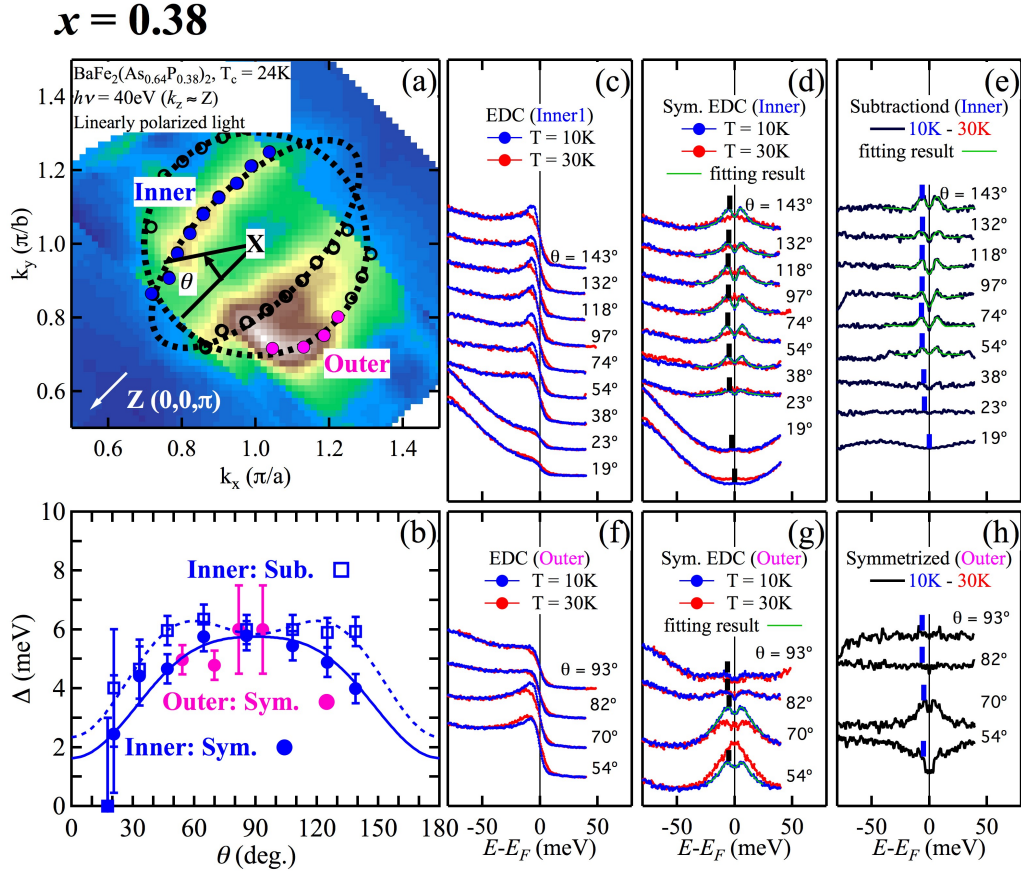


Figure 5.7: (a) Fermi surface mapping of the electron Fermi surface for  $x = 0.38$  taken using linearly polarized light with  $h\nu = 40$  eV corresponding to  $k_z = Z$ ; blue and pink filled circles are  $k_F$  points on the inner and outer electron Fermi surfaces, respectively; black open circles are  $k_F$  and symmetrized  $k_F$  on the Fermi surface; (b) gap size vs FS angle for the inner and outer electron Fermi surfaces; Fermi surface angle  $\theta$  is the angle between the  $X$ - $Z$  and  $X$ - $k_F$  direction; black dashed ellipses are fitting results of  $k_F$  on the inner and outer electron Fermi surfaces, respectively; (c)-(e) and (f)-(h) EDCs, symmetrized EDCs, and subtraction of  $T > T_c$  EDCs from  $T < T_c$  EDCs at  $k_F$  points on the inner and outer electron Fermi surfaces; black (blue) sticks mark the gaps size, which have been obtained by fitting the EDCs to the Norman function introduced in section 4.4.

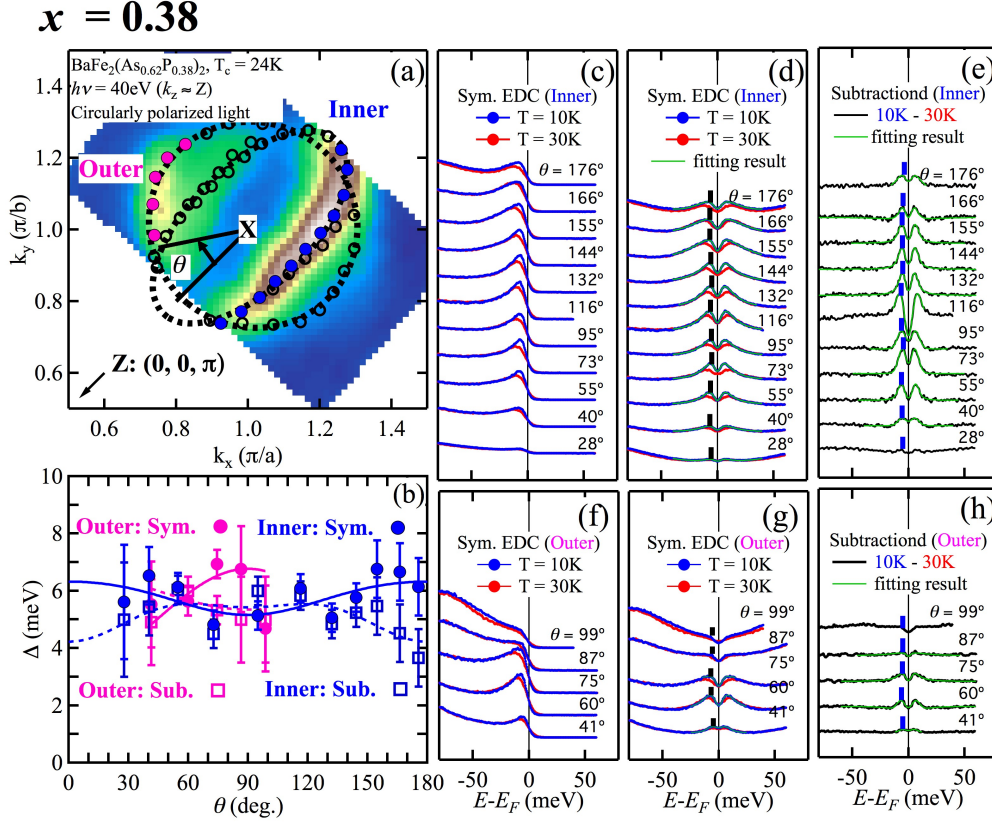


Figure 5.8: (a) Fermi surface mapping of the electron Fermi surface for  $x = 0.38$  taken using right-handed circularly polarized light with  $h\nu = 40\text{ eV}$  corresponding to  $k_z = Z$ ; blue and pink filled circles are  $k_F$  points on the inner and outer electron Fermi surfaces, respectively; black open circles are  $k_F$  and symmetrized  $k_F$  on the Fermi surface; (b) gap size vs FS angle for the inner and outer electron Fermi surfaces; Fermi surface angle  $\theta$  is the angle between the X-Z and X- $k_F$  direction; black dashed ellipses are fitting results of  $k_F$  on the inner and outer electron Fermi surfaces, respectively; (c)-(e) and (f)-(h) EDCs, symmetrized EDCs, and subtraction of  $T > T_c$  EDCs from  $T < T_c$  EDCs at  $k_F$  points on the inner and outer electron Fermi surfaces; black (blue) sticks mark the gaps size, which have been obtained by fitting the EDCs to the Norman function introduced in section 4.4.

gap structure of the sample with composition  $x = 0.45$  ( $T_c = 20$  K) is a little smaller than that of the sample with  $x = 0.38$  ( $T_c = 24$  K).

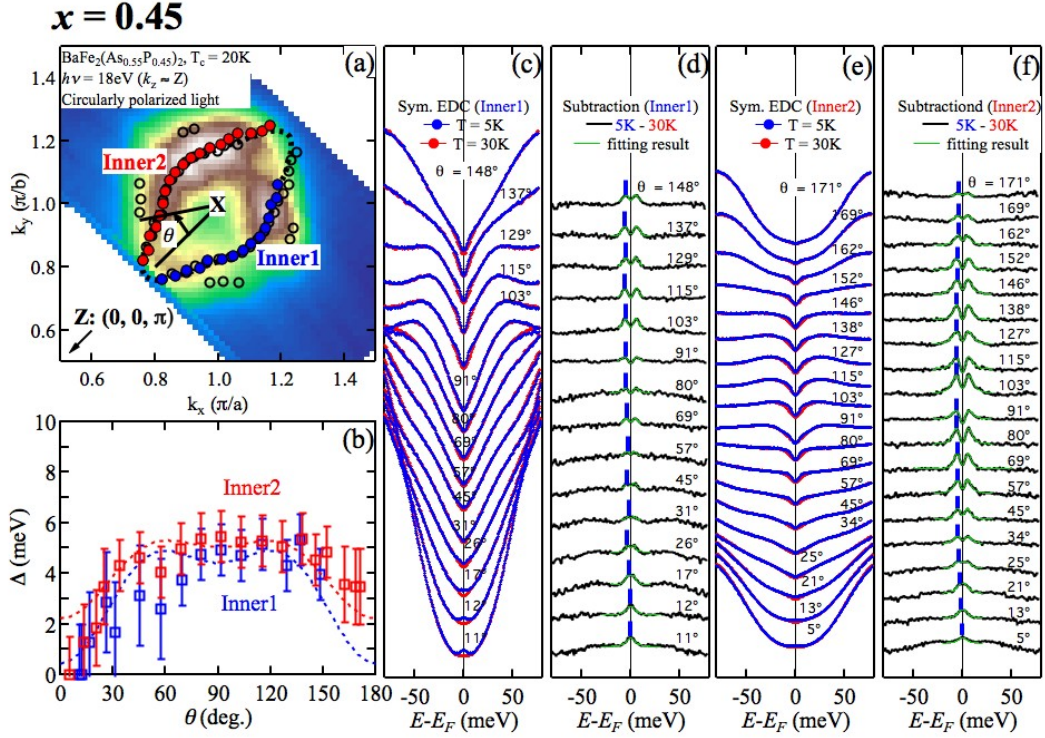


Figure 5.9: (a) Fermi surface mapping of the electron Fermi surface for  $x = 0.45$  taken using right-handed circularly polarized light with  $h\nu = 18$  eV corresponding to  $k_z = Z$ ; blue and red filled circles are  $k_F$  points on the inner and outer electron Fermi surfaces, respectively; black open circles are  $k_F$  and symmetrized  $k_F$  on the Fermi surface; (b) gap size vs FS angle for the inner and outer electron Fermi surfaces; Fermi surface angle  $\theta$  is the angle between the X-Z and X- $k_F$  direction; black dashed ellipses are fitting results of  $k_F$  on the inner and outer electron Fermi surfaces, respectively; (c)-(d) and (e)-(f) symmetrized EDCs and subtraction of  $T > T_c$  EDCs from  $T < T_c$  EDCs at  $k_F$  points on the inner and outer electron Fermi surfaces; blue sticks mark the gaps size, which have been obtained by fitting the EDCs to the Norman function introduced in section 4.4..

### (v) Summary

Through the analysis of superconducting gap on the electron Fermi surfaces of the different compositions of  $\text{BaFe}_2(\text{As}_{1-x}\text{P}_x)_2$  (including optimally doped and over doped ones), it is found that the gap size decreases with increasing doping concentration, which is consistent with the tendency of the superconducting

transition temperature  $T_c$ . Especially, when the doping concentration increases to  $x = 0.45$ , the gap size on the inner electron electron pocket exhibits minimum value (around zero) at  $\theta_{k_F} = 0^\circ$  and  $180^\circ$ , which indicating the existence of line nodes. Prior to that, for  $x = 0.34$  and  $0.38$ , the gap on the inner electron electron pocket has more complex features. The inner gap for  $x = 0.38$  is similar to that of  $x = 0.34$  except of the shrinking of the gap at the ends while expanding the gap at the center of the ellipsoid. The anisotropy of the outer gap is slight smaller than that of inner gap; only in the sample  $x = 0.3$  measured using  $h\nu = 28$  eV (shown in Fig. 5.2) anisotropy can be observed, while in other cases the anisotropy is difficult to observe.

Gap size vs FS angle for the inner electron Fermi surfaces with different doping concentrations ( $x = 0.3, 0.34, 0.38$  and  $0.45$ ) shown in Fig. 5.10(a). Fitting results A, B, and C are plotted in Fig. 5.10(b). Gap size are decreasing with the increasing of doping concentrations  $x$  from coefficient A. Notice that, coefficient the scale of B and C is right axis, and the value of B and C are minus. Then therefore anisotropy has a minimum around  $x = 0.34$ .

### 5.2.3 Superconducting gap on the hole Fermi surfaces

Superconducting gap studies of the same doping composition in  $\text{BaFe}_2(\text{As}_{1-x}\text{P}_x)_2$  ( $x = 0.3$ ) have been reported by Zhang *et al.* [87] and Yoshida *et al.* [88]. Loop nodes around the  $Z$  point on the outer hole Fermi surface were reported by Zhang *et al.* [87], however full gap was observed around the  $Z$  point in the same doping composition in ARPES measurement by Yoshida *et al.* [88]. The contradictory results may comes from that the real doping composition in those two experiments are not the same, or the experimental conditions are different as Zhang *et al.* measured the sample at BL5-4 of SSRL, while Yoshida *et al.* at BL-28A of PF. To solve this problem, we take the ARPES measurement in the the same samples with Yoshida *et al.* and carried out the experiment at BL5-4 of SSRL. Experimental results of superconducting gaps on hole Fermi surfaces cross the  $Z$  and  $\Gamma$  points are shown in Fig. 5.11.

A delicate gap occurs around the  $Z$  point with  $h\nu = 35$  eV as shown in right graph of Fig. 5.11(b). The gap looks not like superconducting gap, but also does not like nodal structure. Compare the spectrum measured using photon energy of 35 eV with the 23 eV one. It take us 5-6 times as long as the 23 eV one to measure the 35 eV one. However, the signal-to-noise ratio (S/N) of the spectrum measured using 35 eV is still worser than the S/N of the 23 eV one. Therefore, experimental condition may be one possibility which lead to that controversies. However, the strange gap in Fig. 5.11(b) is also different from the loop nodes mentioned above [87].

In fact, cuts crossing the  $\Gamma$  point also presented different numbers of bands as

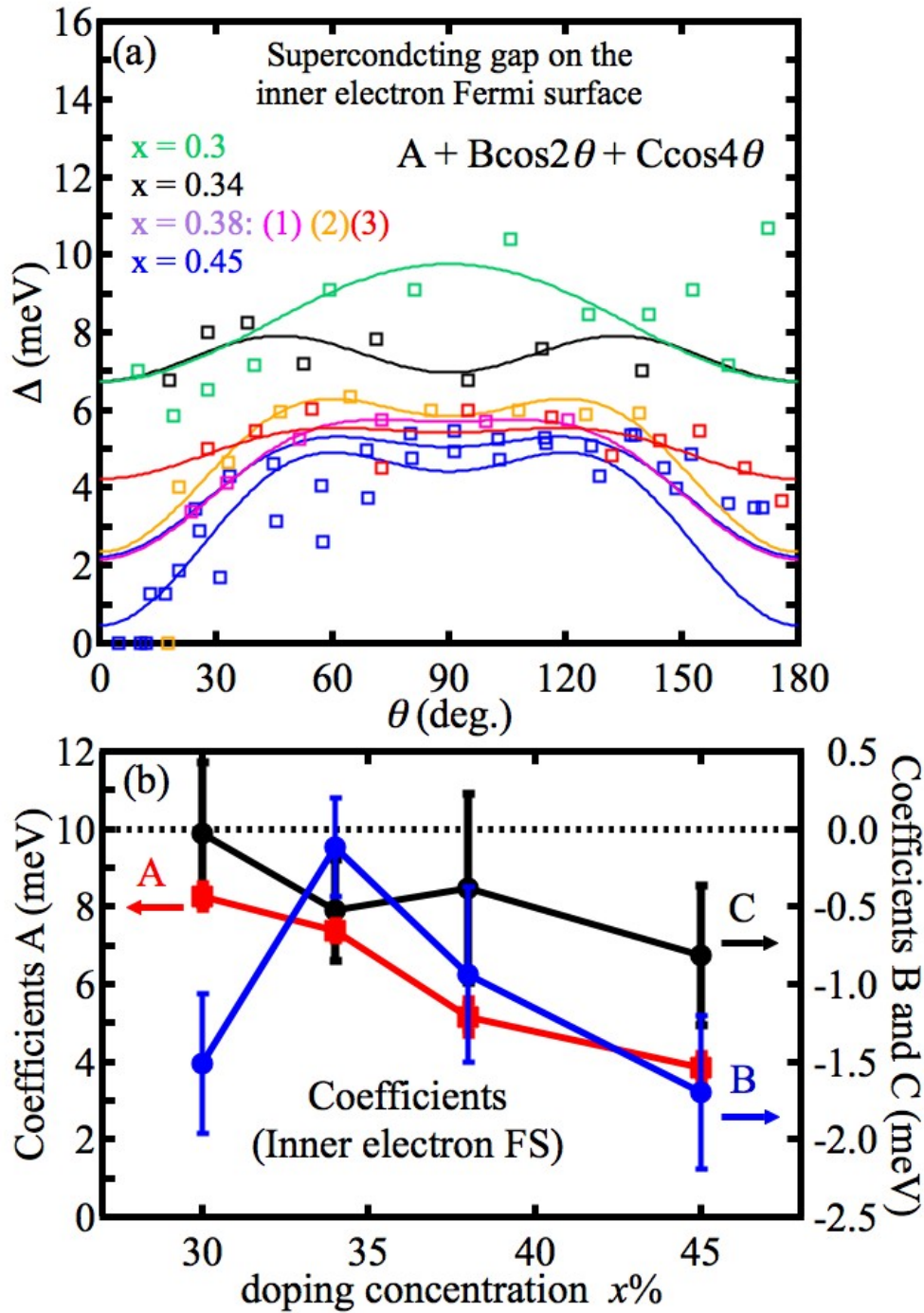


Figure 5.10: (a) gap size vs FS angle for the inner electron Fermi surfaces with different doping concentrations ( $x = 0.3, 0.34, 0.38$  and  $0.45$ ), in which open squares are gap size obtained by fitting the difference EDCs to the Eq. 4.11, solid lines are fitting results using Eq. 4.13, which is written in the graph. (b) Coefficients A, B, and C are parameters in Eq. 4.13, and notice that coefficient A seen in the left axis, coefficients B and C seen in the right axis.

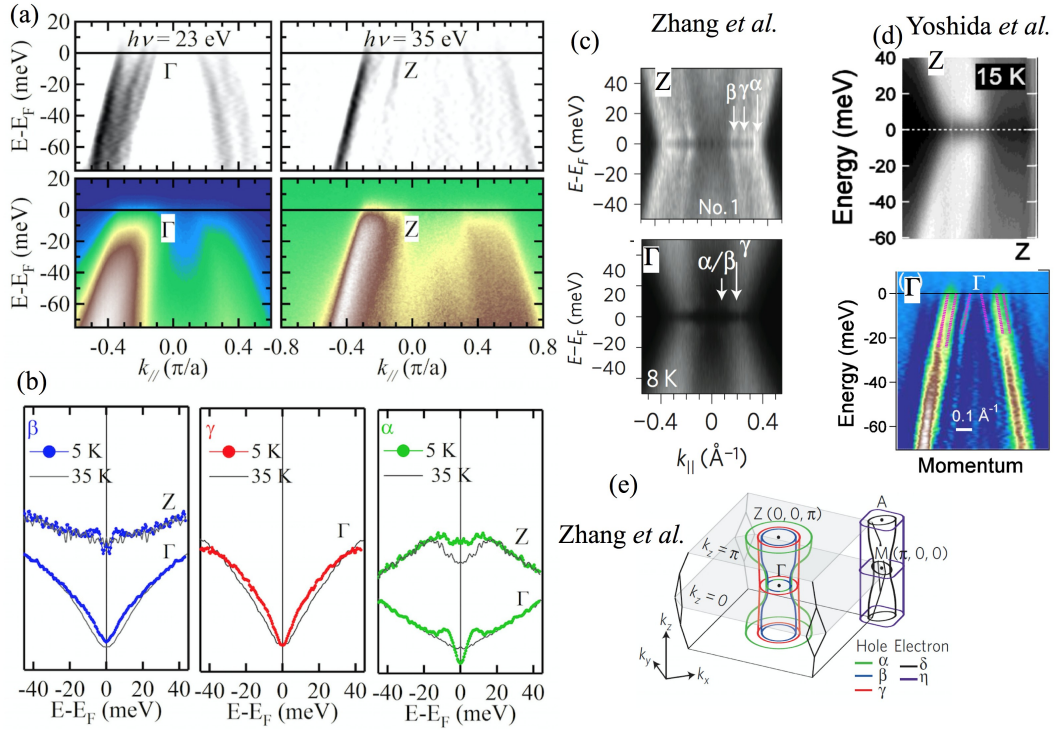


Figure 5.11: (a) ARPES spectra and second derivatives of the ARPES spectra of  $x=0.3$  around  $Z$  and  $\Gamma$  points measured by 23 eV and 35 eV photons, respectively, with right-handed circularly polarization. (b) Symmetrized EDCs at  $k_F$ s on the  $\alpha$  (green),  $\beta$  (blue), and  $\gamma$  (red) hole Fermi surfaces around the  $\Gamma$  and  $Z$  points, respectively, corresponding to the colour in Fig. (e) [87]. Spectra by Zhang *et al.*(c) [87] and Yoshida *et al.*(d) [88].

shown in Fig. 5.11(f) and (g) [87, 88]. Both of the two cuts were measured under the circular polarized light with the same photon energies; but one is measured in SSRL (Zhang *et al.*) and the other one was in PF (Yoshida *et al.*). For example, three bands are observed around  $Z$  point in Figs. 5.11(a) and (d), but only two bands are observed in Fig. 5.11(c). It seems possible that the cuts slowly deviate from the center cuts with the changing of the photon energies; or that weight of spectral are different in SSRL and PF, which was investigated in section 4.2; or the real doping composition are different in Zhang *et al.* [87] and Yoshida *et al.* [88].

Figures 5.12 and 5.13 are ARPES spectra of  $x = 0.38$  and  $0.45$  on the hole Fermi surfaces, respectively. Nodes appears around the  $k_z = 1.5\pi$  on the hole Fermi surfaces in  $x = 0.45$ , as shown in Fig. 5.13(e). The superconducting gap on the hole Fermi surface may give a clue to the pairing mechanism of the  $\text{BaFe}_2(\text{As}_{1-x}\text{P}_x)_2$ .

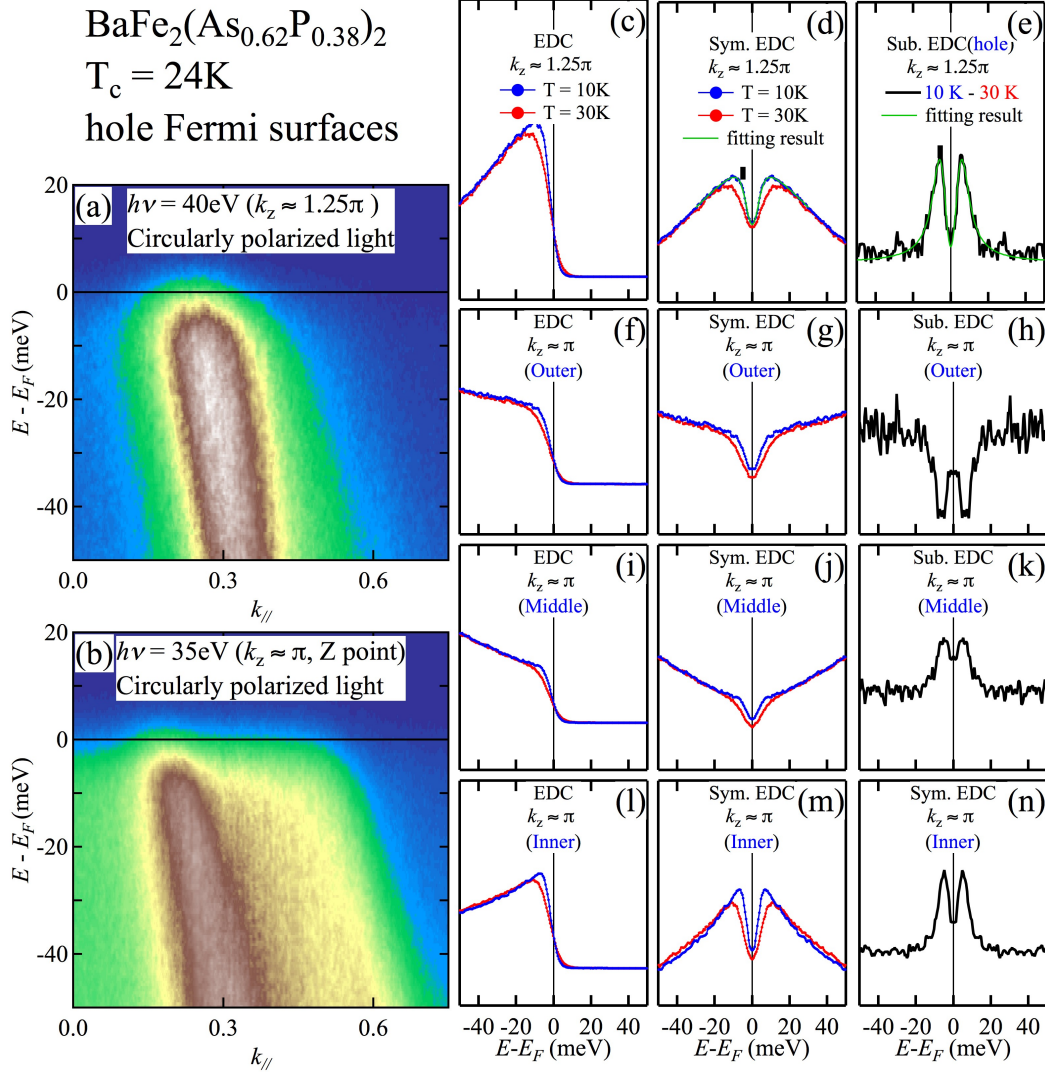


Figure 5.12: ARPES spectra of  $x = 0.38$  around (a)  $k_z = 1.25\pi$  and (b)  $k_z = \pi$  (Z point) measured by 40 eV and 35 eV photons, respectively, with right-handed circularly polarization. (c)-(e) EDCs, symmetrized EDCs, and difference EDCs between of  $T > T_c$  and at  $T < T_c$  EDCs at  $k_F$  point around the  $k_z = 1.25\pi$  on the hole Fermi surfaces; (f)-(h), (i)-(k) and (l)-(n) EDCs, symmetrized EDCs, and difference EDCs between of  $T > T_c$  and at  $T < T_c$  EDCs at  $k_F$  points around the  $k_z = \pi$  (Z point) on the inner, middle and outer hole Fermi surfaces, respectively.

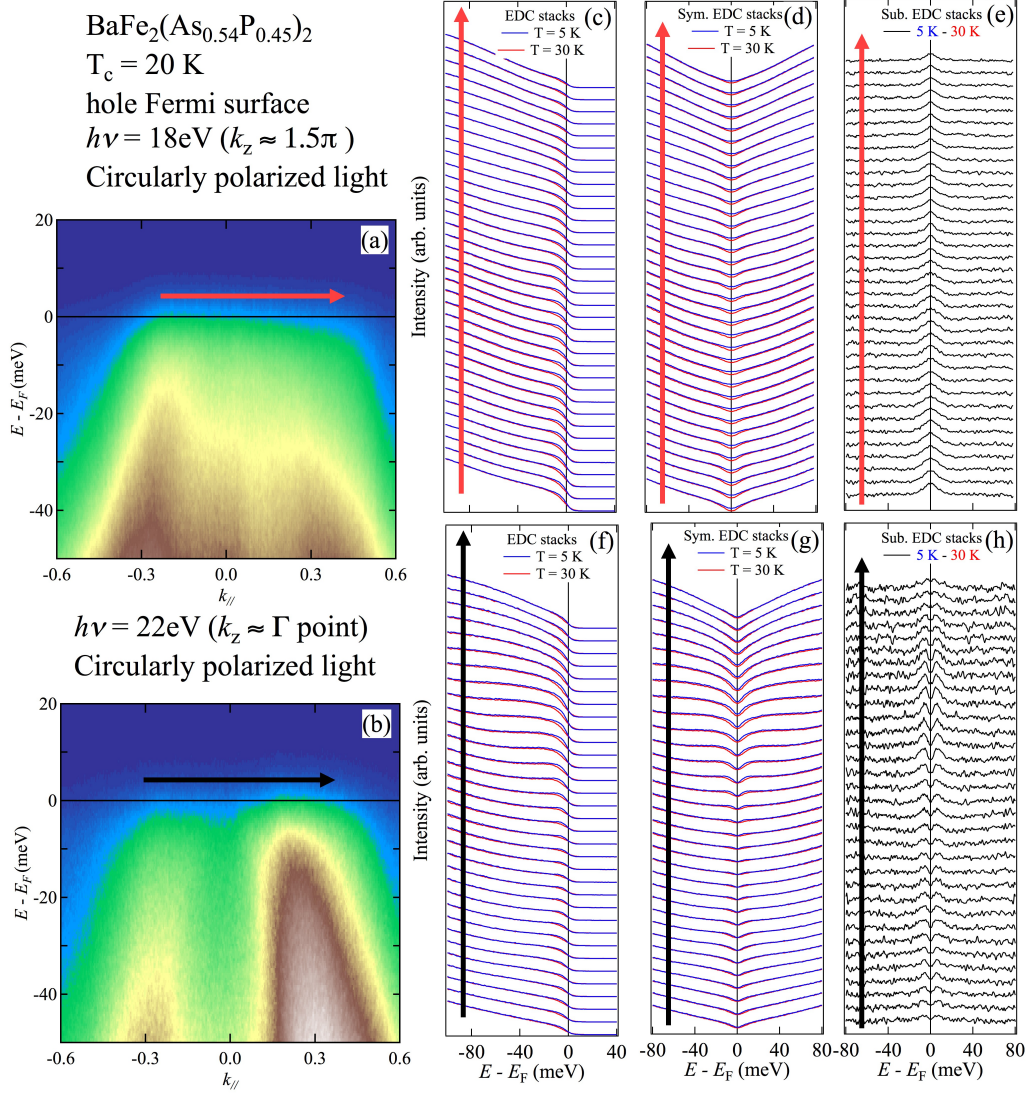


Figure 5.13: ARPES spectra of  $x=0.45$  around (a)  $k_z = 1.5\pi$  and (b)  $k_z = 0$  ( $\Gamma$  point) measured by 18 eV and 22 eV photons, respectively, with right-handed circular polarization. (c)-(e) and (f)-(h) EDC, symmetrized EDC, and difference EDC stacks along the red and black arrows around the  $k_z = 1.5\pi$  and  $k_z = 0$  on the hole Fermi surfaces, respectively.

## 5.3 Discussion about the superconducting gap on the electron Fermi surfaces

According to above-mentioned experiments on the superconducting gap on the electron Fermi surfaces in  $\text{BaFe}_2(\text{As}_{1-x}\text{P}_x)_2$ , it is found that in the optimal doping and over doping ranges, with increasing doping composition, the superconducting gap  $|\Delta|$  decreases and line nodes appear at  $x = 0.45$ . Comparison of the experimental results and the theoretical studies referred to in section 2.4.2 will be performed in the following. Theoretical results (Saito *et al.* [67], section 2.4.2) are organized in Figs. 5.14 and 5.16.

### 5.3.1 Orbital fluctuation

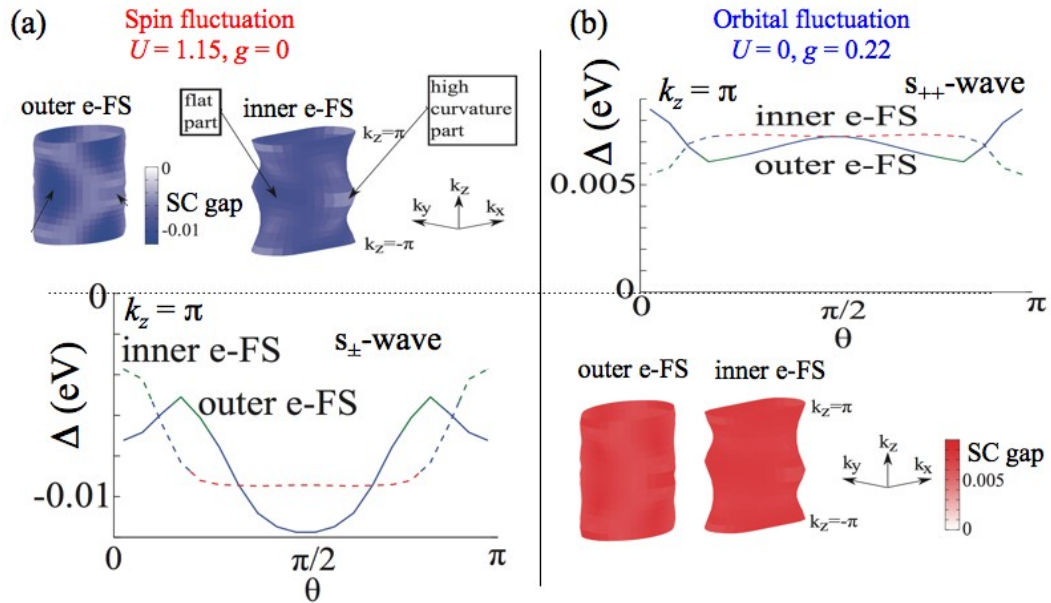


Figure 5.14: Superconducting gap functions in the presence of (a) spin and (b) orbital fluctuation pairing mechanism [67].

Through the comparison between different theoretical studies, e.g. by Saito *et al.* [67] introduced in section 2.4.2, and our experimental results, the gaps on the inner and outer electron Fermi surfaces shown in Fig. 5.14(b) are close to those of the composition  $x = 0.34$ , as shown in Figs. 5.4(b) and 5.5(b)-(c). In both cases, the inner and outer electron superconducting gaps exhibit slightly anisotropy. The gap size in Fig. 5.4(b) is consistent with the experimental result of  $\text{BaFe}_2(\text{As}_{1-x}\text{P}_x)_2$  with  $x = 0.34$  in Fig. 5.4(b) and 5.5(b)-(c). Therefore, for the composition with  $x =$

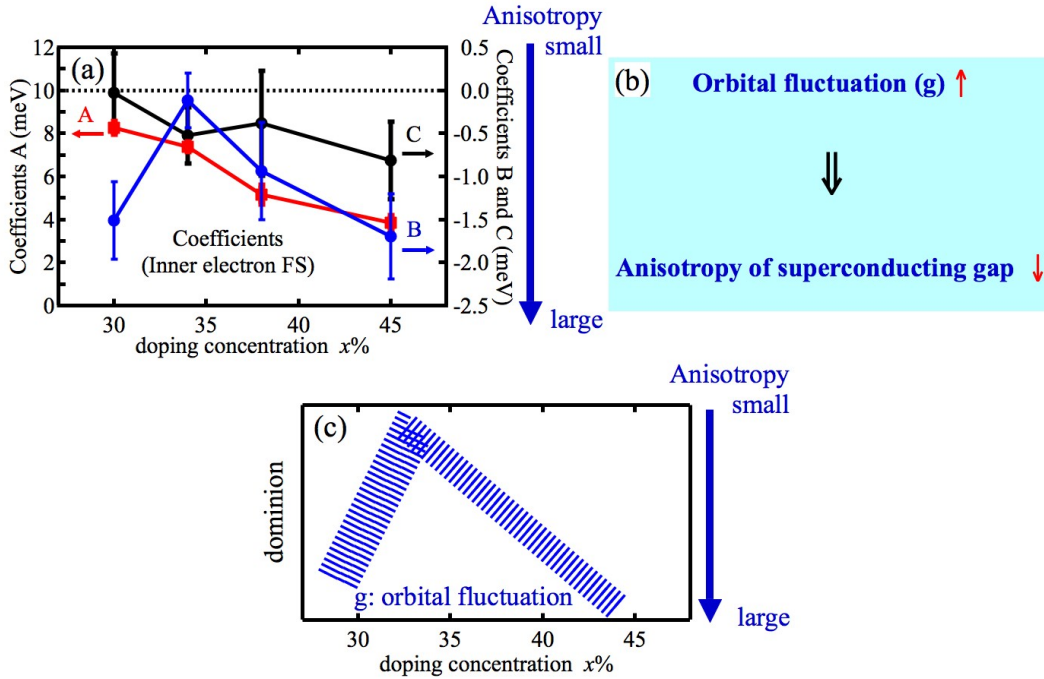


Figure 5.15: (a) Coefficients A, B, and C are parameters in Eq. 4.13 and Fig. 5.10; (b) relationship between orbital fluctuation ( $g$ ) and anisotropy of superconducting gap on the electron Fermi surfaces; (c) sketch map of dominion of orbital fluctuation with different doping concentrations.

0.34, the orbital fluctuation should be dominant, yet spin fluctuation also exists. Otherwise it would be difficult to explain the obvious gap anisotropy in other compositions and the appearance of minimum gap size around the edge on the inner electron Fermi surface for  $x = 0.45$ .

Comparison between Figs. 5.14(a) and (b) implies that the superconducting gap on the electron Fermi surfaces exhibits strong anisotropy ( $\approx 10$  meV) when spin fluctuation is overwhelming strong while it only has weak anisotropy ( $\approx 2$  meV) when orbital fluctuation is dominant. In combination with the theoretical calculation in Fig. 5.16, in which the anisotropy is only about 1 meV with strong spin and orbital fluctuation, one can infer that the gap anisotropy would attenuate with increasing orbital fluctuation  $g$ , as shown in 5.15. In addition, the previous experiments have demonstrated that the gap anisotropy has a slight increase with increasing doping concentration. Therefore, the orbital fluctuation  $g$  decreases with increasing doping concentration  $x$ .

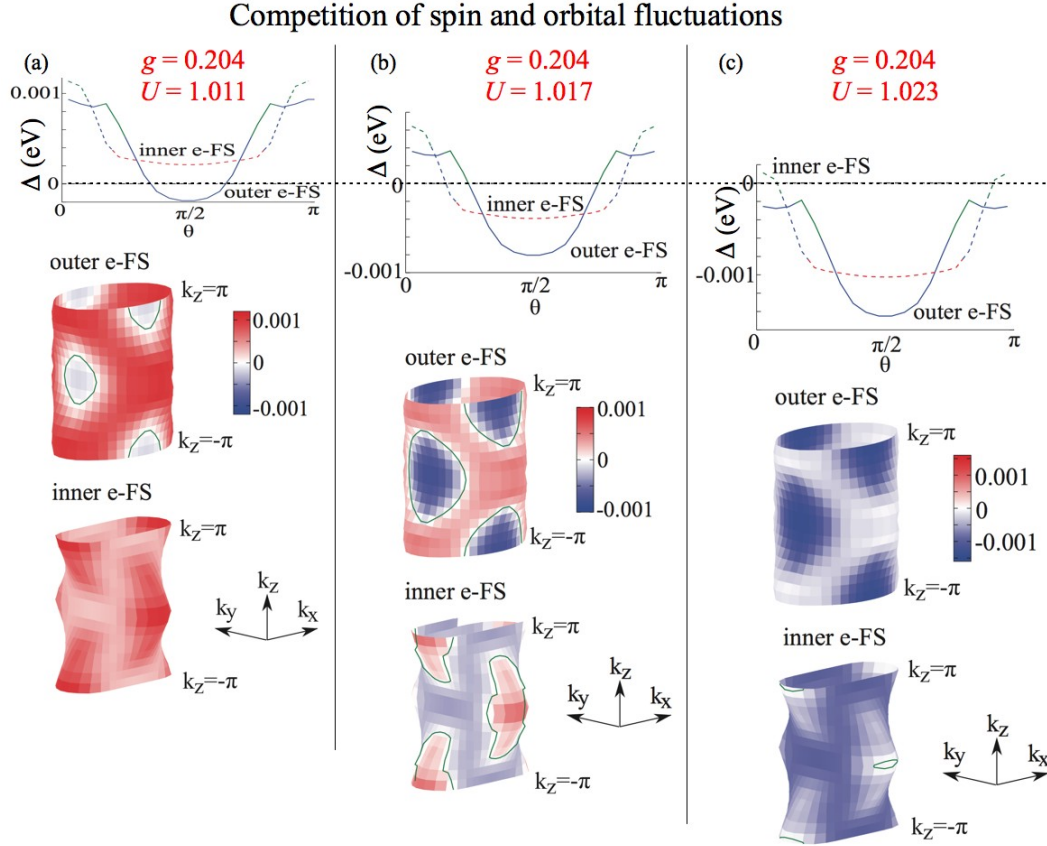


Figure 5.16: Superconducting gap functions in the presence of competition between spin and orbital fluctuations-mediated pairing mechanism with  $g = 0.204$ , (a)  $U = 1.011$ , (b)  $U = 1.017$ , and (c)  $U = 1.023$  [67].

### 5.3.2 Spin fluctuation

Other than above-mentioned anisotropy trends, in our results the superconducting order parameter  $\Delta$  has a tendency of shifting to negative value ( $|\Delta|$  is increasing when  $\Delta < 0$ ), which is consistent with the tendency of  $T_c$ . This effect is also consistent with the theory for competition of spin and orbital fluctuation suggested by Saito *et al.* [67], as shown in Fig. 5.16, in which the definition of Fermi angle  $\theta$  and the position of electron Fermi surfaces are the same as ours.

Figure 5.16 shows the theoretical calculation results of competition of spin and orbital fluctuation, with slightly increasing of parameter  $U$ , which indicating spin fluctuation. In the Fig. 5.16, the value of  $\Delta$  shifts to the negative direction; yet its absolute value  $|\Delta|$  has a decrease before increase. In comparison with the experimental results shown in Fig. 5.10, from  $x = 0.3$  to  $x = 0.45$ , the  $|\Delta|$  of the inner electron gaps tends to shift downward; the gap size on the edges ( $\theta =$

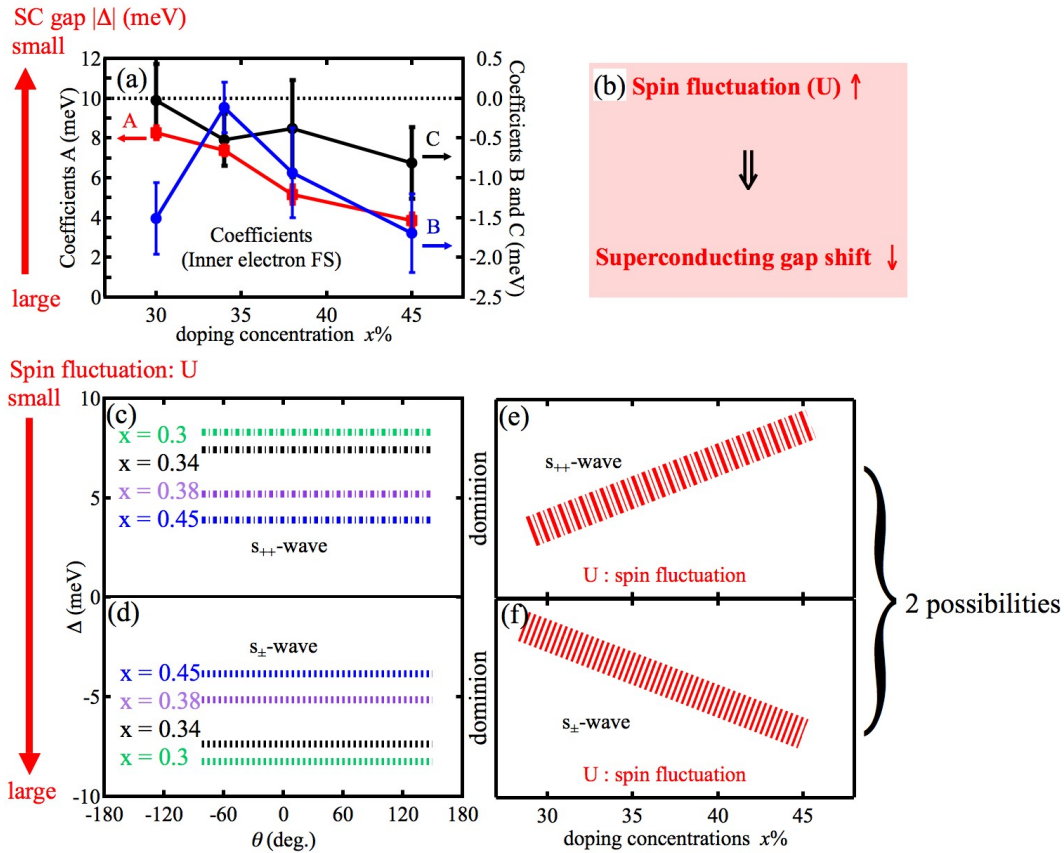


Figure 5.17: (a) Coefficients A, B, and C are parameters in Eq. 4.13 and Fig. 5.10; (b) relationship between spin fluctuation ( $U$ ) and shift of superconducting gap on the electron Fermi surfaces; sketch maps of two possibilities of (c), (d) size of superconducting gap and (e), (f) spin fluctuation on the electron Fermi surfaces with different doping concentrations.

$0^\circ$  and  $180^\circ$ ) is always small; and very small minimum gap (indicating the exists of line node) appear at  $x = 0.45$ . In the experiments, we are not sure about the sign of the gap values  $\Delta$ . Therefore, one can conclude that with increasing over doping concentration, the spin fluctuation is increasing with positive  $\Delta$  ( $s_{++}$ -wave), or decreasing with negative  $\Delta$  ( $s_{\pm}$ -wave) as shown in Fig. 5.17.

In other words, with increasing carrier concentration towards over doping, the spin fluctuation is either increasing or decreasing; but we donot know which of them is right. Compare experimental with theoretical results, we find that the minimum gap appears on the centre ( $\theta = 90^\circ$ ) of the electron Fermi surface in the  $s_{++}$ -wave case (Fig. 5.16(a)), which does not correspond to the experimental results. Otherwise, the experimental results correspond to the  $s_{\pm}$ -wave as shown in Fig. 5.16(c), which have minimum gap on the edge ( $\theta = 0^\circ$  and  $180^\circ$ ) of the electron Fermi surface. Therefore, the pairing mechanism in the optimally doped and over doped  $\text{BaFe}_2(\text{As}_{1-x}\text{P}_x)_2$  superconductors is  $s_{\pm}$ -wave, as shown in Fig. 5.17(d) and (f).

Moreover, which one is more dominant in the system, spin fluctuation or orbital fluctuation? That question will be discussed in the following sections.

### 5.3.3 Competition between spin and orbital fluctuations

In the experimental results of the superconducting gaps on electron Fermi surfaces at  $x = 0.45$ , the gap is the largest for  $\theta = 90^\circ$ ; and the minimum gap ( $\sim 0$ ) appear at the edges ( $\theta = 90^\circ$  and  $180^\circ$ ), in accordance with a prediction of the spin fluctuation mechanism shown in Fig. 5.16(a). It is also consistent with the above-mentioned conclusion that the orbital fluctuation decreases with increasing doping concentration. According to the parameters shown in Fig. 5.16(a), the orbital fluctuation parameter  $g$  is rather small (e.g., close to 0) while the spin fluctuation parameter  $U$  is relatively larger (e.g., close to 1) in heavily over doped materials (e.g.,  $x = 0.45$ ); that is to say, under this condition the pairing mechanism is  $s_{\pm}$ -wave.

Based on what we mentioned in section 5.3.1, the value of  $\Delta$  shifts to the negative direction with increasing spin fluctuation, and the superconducting gap size tend to decrease with increasing doping concentration, the spin fluctuation parameter  $U$  decreases with increasing  $x$  as above-mentioned orbital fluctuation parameter  $g$  decrease. In addition, the orbital fluctuation is dominant in the composition  $x = 0.34$  (as mentioned in section 5.3.1), different from the situation in the material with  $x = 0.45$ . Thus, in the range of  $0.3 < x < 0.45$ , both parameters decrease with increasing  $x$ , yet  $g$  decreases at a faster rate, as illustrated in Fig. 5.18.

By comparing the experimental results of composition  $x = 0.3$  and  $0.34$  in Fig. 5.2(b) and Fig. 5.4(b), it is noticed that the gap anisotropy of the material at  $x =$

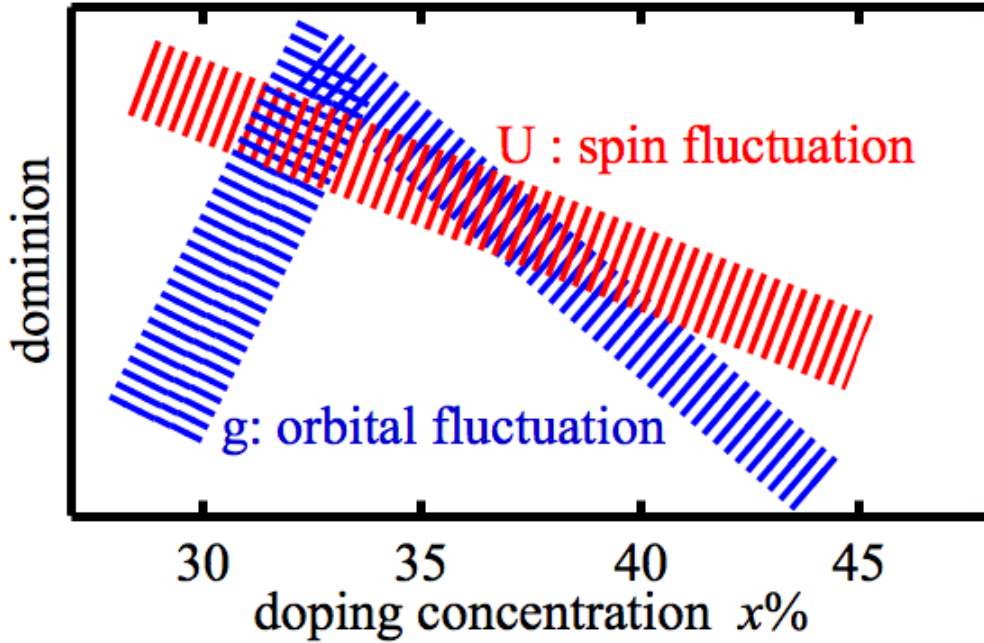


Figure 5.18: Sketch map of weight between spin and orbital fluctuations inferred from experimental results as shown in Fig. 5.10.

0.3 is more significant than that at  $x = 0.34$ ; yet the  $|\Delta|$  value of the former one is also larger than that of the latter one. It is just like at  $x = 0.3$  the parameter  $U$  is larger than the case at  $x = 0.34$  while the parameter  $g$  is smaller than that at  $x = 0.34$ . In other words, the parameter  $g$  might begin to decrease when  $x < 0.3$ , as shown in Fig. 5.18. For better comprehending competition of spin and orbital fluctuation, experimental studies on the hole Fermi surface is also important, which will be introduced in the next section. This issue will be discussed in the following section.

## 5.4 Analysis of the superconducting gap on the hole Fermi surfaces

ARPES experiments of  $\text{BaFe}_2(\text{As}_{1-x}\text{P}_x)_2$  ( $x = 0.35$ ) on the hole Fermi surface at  $k_z \approx 3/4\pi$  with photon energy of 7 eV were performed by Shimojima *et al.* [79]. The full superconducting gaps on the inner, middle, and outer hole Fermi surfaces are found to be almost the same, as shown in Fig. 2.16(I), section 2.4.1. This gap symmetry does not correspond to the spin fluctuation case shown in Fig. 5.19(c), in which the gap on the inner hole Fermi surface is about 2 times as the gap on

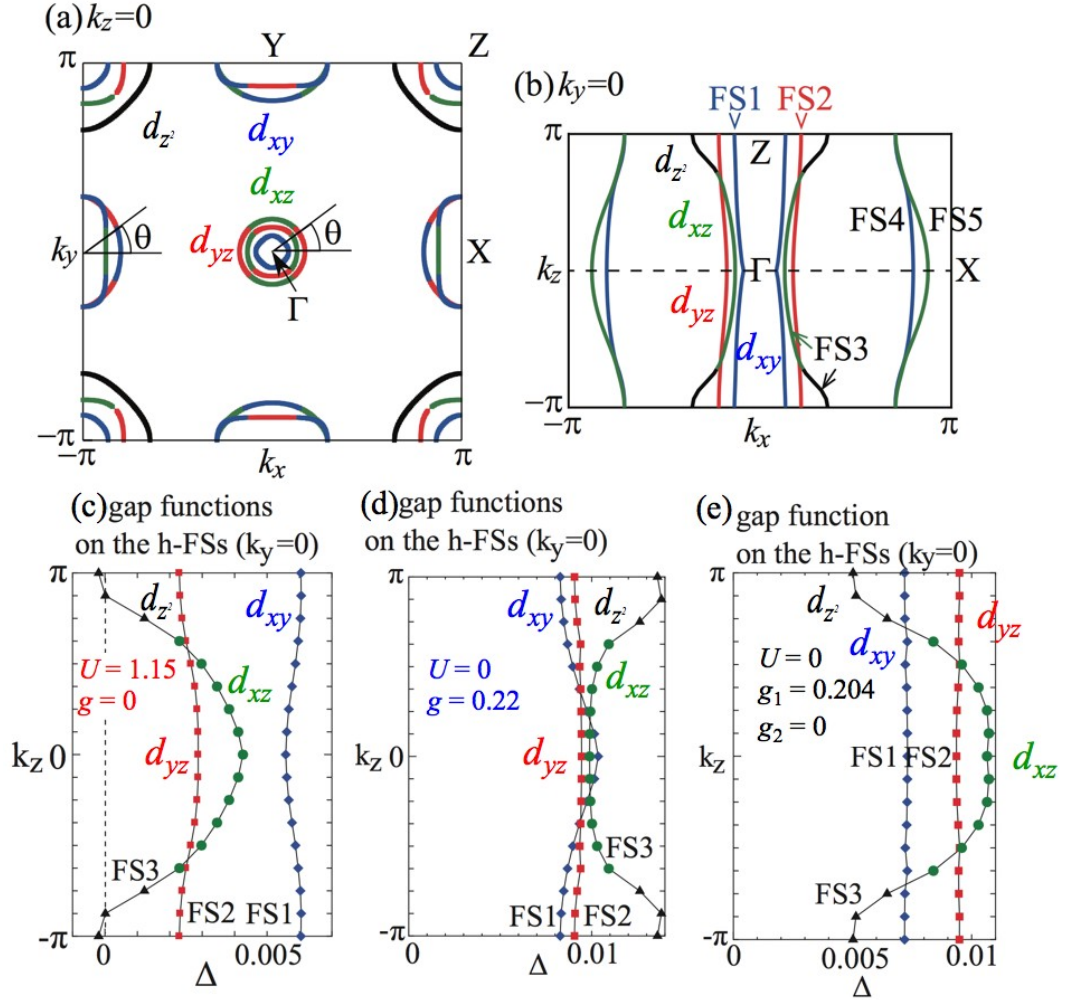


Figure 5.19: Fermi surfaces in the (a)  $k_z = 0$  and (b)  $k_y$  plane. Superconducting gap functions on the hole Fermi surfaces in the presence of (c) spin fluctuation pairing mechanism with  $U = 1.15$  and  $g_1 = g_2 = g = 0$ , (d) orbital fluctuation pairing mechanism with  $U = 0$  and  $g_1 = g_2 = g = 0.22$ , and (e)  $U = 0$ ,  $g_1 = 0.204$ , and  $g_2 = 0$  [67].

the middle and outer hole Fermi surfaces near  $k_z \approx 3/4\pi$ . Instead it is consistent with the orbital fluctuation case shown in Fig. 5.19(d) and (e), in which the gaps on the hole Fermi surfaces have almost the same values as the gaps near  $k_z \approx 3/4\pi$ . The experiments carried out by Shimojima *et al.* [79] suggested a similar viewpoint to ours, i.e., the orbital fluctuation is dominant for the sample with  $x = 0.34$ , as mentioned in section 5.3.1.

The ARPES experiments on hole Fermi pockets of  $\text{BaFe}_2(\text{As}_{1-x}\text{P}_x)_2$  ( $x = 0.3$ ) were reported by Zhang *et al.* [87] and Yoshida *et al.* [88], as introduced in section 2.4.1, Fig. 2.16(III) and (II), respectively. The loop nodes around  $Z$  point were observed in the ARPES measurement of Zhang *et al.* [87], which seems to be corresponding to the spin fluctuation-dominating case or limited value  $g_1$  and  $g_2 = 0$  case, as shown in Fig. 5.19(c) and (e), respectively. However, Yoshida *et al.* [88] failed to observe the loop nodes as well as the gaps on the hole Fermi surfaces with various  $k_z$ , as shown in Fig. 2.16(II.c); which looks like the case between orbital fluctuation-dominating case and the spin fluctuation-dominating case ( $g_1$  is a limited value and  $g_2 = 0$ ). Here,  $g_1$  and  $g_2$  are given by Eq. 2.3 in section 2.4.2, representing the electron-phonon interaction of the iron ion oscillations. Especially,  $g_1$  is related to the  $d_{yz}$  and  $d_{xz}$  orbitals while  $g_2$  is related to the  $d_{xy}$  orbitals. Thus, we cannot exclude the small possibility of the oscillation of  $d_{xy}$  orbitals. Anyhow, the experimental results from Zhang *et al.* [87] is more like the spin fluctuation-dominating case while results from Yoshida *et al.* [88] is more like the spin fluctuation-dominating case, even though the claimed compositions are all  $x = 0.3$ .

The cause of this contradiction might be the stoichiometric ratio of their sample deviating from  $x = 0.3$ , because their conclusion seems like spin fluctuation mechanism, which is the mechanism in the under doped materials shown in Fig. 5.18. Another possibility is the lower temperature available at BL5-4 of SSRL, which might enhance the influence of the spin fluctuation mechanism.

## 5.5 Summary

In this Chapter, we have measured the spectra on the electron Fermi surfaces around the  $Z$  point below and above  $T_c$  via ARPES measurement, and deduced the superconducting gap size from the fitting using the Norman function. Comparing

- (1) the change of the superconducting gap size,
- (2) gap anisotropy,
- (3) and the possible appearance or disappearance of line nodes

of our experimental results of superconducting gap on the inner electron Fermi surface with the previous theoretical study on the competition between spin and orbital fluctuations, the doping concentration  $x$ -dependence of the spin and orbital fluctuations was inferred. With the deduced  $x$  dependence we successfully

explained the contradiction between previous ARPES experiments.



# Chapter 6

## Conclusions and prospects

### 6.1 Conclusions

We studied the superconducting gap structure on the Fermi surfaces in the isovalent-substituted  $\text{BaFe}_2(\text{As}_{1-x}\text{P}_x)_2$  by ARPES for investigating the superconducting gap anisotropy and symmetry. For investigating the superconducting gap structure precisely, rigorous gap analysis methods are required.

We use the electric dipole approximation and selection rules in case of the mixing of different orbital characters in the spectrum in  $\text{BaFe}_2(\text{As}_{1-x}\text{P}_x)_2$ . Since in most of ARPES experiments the photoelectrons are detected by rotating the specimens, which results in the deviation of the incident light from the symmetry plane. Thus the analysis of spectrum based on symmetry of orbitals could lack rigour. Numerically photoemission spectroscopy calculations for different electron orbitals were carried out. The convolution of superimposed Lorenz functions and Gaussian function is used to fit the energy distribution curves (EDCs) and momentum distribution curves (MDCs) for determining the  $k_F$ . The Norman function is used to fit the symmetrized and subtracted EDCs for obtaining the superconducting gap.

According to the previous theoretical studies, enhanced spin fluctuation promotes the transformation from  $s_{++}$ - or nodeless  $s_{\pm}$  wave to nodal  $s$ -wave pairing; furthermore, the greater the orbital fluctuation is, the weaker the gap anisotropy is. Thus we inferred the trend of spin and orbital fluctuations according to our experimental results by comparing the change of the gap anisotropy (inferring the orbital fluctuation parameter  $g$ ) and superconducting gap size (inferring the spin fluctuation parameter  $U$ ).

Around the optimal doping concentration ( $x = 0.3$ ) momentum-dependent anisotropy in the superconducting gap is observed, in which the spin fluctuation-mediated pairing is more significant than the orbital fluctuation-mediated pairing parameter. When the doping concentration increases to  $x = 0.34$ , the anisotropy

turns to small, in which orbital fluctuation-mediated pairing slowly increases and gradually become dominant. We thus infer that, when the doping concentration continues to increase, the orbital fluctuation coupling parameter  $g$  decreases faster than the Coulomb interaction  $U$ , which enhances spin fluctuations, decreases. In the over-doped range, obvious anisotropy is observed for  $x = 0.38$  more strongly than for  $x = 0.34$ . When the doping concentration increases further more, obvious anisotropy and very small superconducting gap on the edges of inner electron Fermi surface is observed in  $x = 0.45$ , in which parameter of spin fluctuation  $U$  is more significant than the orbital fluctuation parameter  $g$ .

## 6.2 Prospects

- (1) To compare the competing spin and orbital fluctuations, the superconducting gap of  $\text{BaFe}_2(\text{As}_{1-x}\text{P}_x)_2$  should also be measured with various  $k_z$  on the hole and electron pockets.
- (2) In ARPES experiments, although  $k_z$  is nearly a constant while changing  $k_{\parallel}$  when the hole surface is measured with one photon energy, the Fermi surface bends heavily in 3D space, especially with low photon energies when detecting the electron surfaces. Therefore, it is necessary to obtain a 3D superconducting gap by detecting the entire electron surface using a series of photon energies so as to determine the gap anisotropy and possible nodal structure.
- (3) In addition, to discuss the change of spin fluctuation parameter  $U$  and orbital fluctuation parameter  $g$  more precisely, measurements of the superconducting gap of the outer hole pocket near the  $Z$  point in under-doped  $\text{BaFe}_2(\text{As}_{1-x}\text{P}_x)_2$  are required. If the appearance of a gap or an abrupt decrease of loop nodal gap is observed, it can be inferred that in the under-doped region  $g$  decreases abruptly while the spin fluctuation becomes dominant gradually.

# Acknowledgments

It is my honor to convey my sincere gratitude to the people who contributed in different ways to the present study. Foremost I thank all the participants of this research for their time and effort to help me with this dissertation, I sincerely acknowledge their contribution.

First of all, and the most of all, I would like to express my deepest gratitude to my supervisor Professor Atsushi Fujimori, Department of Physics, The University of Tokyo for his supervision. I would like to thank him for his patient guidance, valuable advice, constructive comments, and continuous encouragement throughout my doctoral course, and also for his critical reading of this manuscript. Moreover thanks for the trust and confidence in my studies during the three years and a half.

I would like to express my gratitude to Professor Kozo Okazaki, Institute for Solid State Physics, the University of Tokyo; Professor Teppei Yoshida, Graduate School of Human and Environmental Studies, Kyoto University; and Mr. Hakuto Suzuki in our lab for their systematic teaching the experimental methods and analysis procedures.

I would like to gratefully acknowledge Professor Zhi-Xun Shen, Dr. Donghui Lu, and Dr. Makoto Hashimoto, Department of Physics, Stanford University; Professor Kanta Ono and Professor Hiroshi Kumigashira, Photon Factory, National Laboratory for High Energy Physics (PF, KEK) for their technical support.

I am also very grateful to Dr. Masamichi Nakajima, Special research fellow in National Institute of Advanced Industrial Science and Technology (AIST) for providing his high quality samples and meaningful cooperation.

I would like to thank Professor Shi-ichi Uchida, Dr. Shinichiro Ideta, the University of Tokyo; Dr. Chul-Ho Lee, Dr. Akira Iyo, and Dr. Hiroshi Eisaki, Research Institute for Energy Conservation, AIST for their cooperation.

I want to express my gratitude to Professor Kozo Okazaki, Department of Physics, the University of Tokyo; Professor Teppei Yoshida, Graduate School of Human and Environmental Studies, Kyoto University; and Mr. Hakuto Suzuki in our lab for their systematic teaching the experimental methods and analysis procedures.

I would like to thank all the members of Fujimori group for the academic

atmosphere and comfortable environment. I will always remember good memories with you: doctoral course students: Dr. Keisuke Ishigami, Dr. Cristobal C Leo Ambolode III, Dr. Liang Liu, Mr. Goro Shibata, Mr. Hakuto Suzuki, Mr. Masafumi Horio, and Mr. Shoya Sakamoto; master course students: Mr. Yukio Takahashi, Mr. Keisuke Koshiishi, Mr. Yousuke Nonaka, Mr. Keisuke Ikeda, and Mr. Zhendong Chi.

I would like to thank secretaries Ms. Yuko Shimazaki for purchasing the lab supplies and arranging the travel and reimbursement on expenses associated with the conferences and experiments.

I want to thank the Ministry of Education, Culture, Sports, Science and Technology (MEXT) for the financial support.

Finally, I would like to thank my parents and sister for supporting my student life and research activities. Especially I am extremely thankful to my husband Dr. Liu Yaoyang for his understanding, patience, and supporting in my life.

December 2015

Xu Jian

**References**

- [1] Superconductivity, <https://en.wikipedia.org/wiki/Superconductivity>.
- [2] H. K. Onnes, *Commun. Phys. Lab. Univ. Leiden* **12**, 120+ (1911).
- [3] C. P. Poole, *Handbook of superconductivity* (Academic Press, New York, 2000).
- [4] W. Meissner and R. Ochsenfeld, *Naturwissenschaften* **21**, 787 (1933).
- [5] W. de Hass, *Nature* **123**, 130 (1929).
- [6] W. de Hass, E. von Aubel, and J. Voogd, *Proceedings of the Koninklijke Akademie van Wetenschappen te Amsterdam* **32**, 226 (1929).
- [7] W. de Hass, E. van Aubel, and J. Voogd, *Proceedings of the Koninklijke Akademie van Wetenschappen te Amsterdam* **32**, 715 (1929).
- [8] J. McLennan, *Nature* **125**, 168 (1930).
- [9] J. Bardeen, L. N. Cooper, and J. R. Schrieffer, *Physical Review* **108**, 1175 (1957).
- [10] H. H. Wen, *Chinese Journal of Materials Research* **29**, 241 (2015), in Chinese.
- [11] J. Bednorz and K. Müller, *Zeitschrift für Physik B Condensed Matter* **64**, 189 (1986).
- [12] R. H. Liu, T. Wu, G. Wu, H. Chen, X. F. Wang, Y. L. Xie, J. J. Ying, Y. J. Yan, Q. J. Li, B. C. Shi, W. S. Chu, Z. Y. Wu, and X. H. Chen, *Nature Letters* **459**, 64 (2009).
- [13] Y. Ando, S. Komiya, K. Segawa, S. Ono, and Y. Kurita, *Physical Review Letters* **93**, 267001 (2004).
- [14] A. Batista-Leyva, R. Cobas, M. Orlando, C. Noda, and E. Altshuler, *Physica C: Superconductivity* **314**, 73 (1999).
- [15] J. Schwartz, K. Amm, Y. Sun, and C. Wolters, *Physica B: Condensed Matter* **216**, 261 (1996).
- [16] I. Y. Korenblit, A. Aharony, and O. Entin-Wohlman, *Physical Review B* **60**, 17 (1999).

- [17] C. Fang, J. Hu, S. Kivelson, and S. Brown, *Physical Review B* **74**, 094508 (2006).
- [18] C. H. Cheng, H. Zhang, Y. Zhao, Y. Feng, X. F. Rui, P. Munroe, H. M. Zeng, N. Koshizuka, and M. Murakami, *Superconductor Science and Technology* **16**, 1182 (2003).
- [19] A. P. Drozdov, M. I. Erements, I. A. Troyan, V. Ksenofontov, and S. I. Shylin, *Nature* **525**, 73 (2015).
- [20] Y. Kamihara, T. Watanabe, M. Hirano, and H. Hosono, *Journal of the American Chemical Society* **130**, 3296 (2008), pMID: 18293989.
- [21] J. Paglione and R. L. Green, *Nature Physics* **29**, 645 (2010).
- [22] B. Zeng, G. Mu, H. Q. Luo, T. Xiang, I. I. Mazin, H. Yang, L. Shan, C. Ren, P. C. Dai, and H. H. Wen, *Nature Communications* **1**, 112 (2010).
- [23] J. Maletz, V. B. Zabolotnyy, S. T. D. V. Evtushinsky, A. U. B. Wolter, L. Harnagea, A. N. Yaresko, A. N. Vasiliev, D. A. Chareev, A. E. Bohmer, F. Hardy, T. Wolf, C. Meingast, E. D. L. Rienks, B. Buchner, and S. V. Borisenko, *Physical Review B* **89**, 220506 (2014).
- [24] K. Hashimoto, S. Kasahara, R. Katsumata, Y. Mizukami, M. Yamashita, H. Ikeda, T. Terashima, A. Carrington, Y. Matsuda, and T. Shibauchi, *Physical Review Letters* **108**, 047003 (2012).
- [25] Y. Nakai, T. Iye, S. Kitagawa, K. Ishida, S. Kasahara, T. Shibauchi, Y. Matsuda, and T. Terashima, *Physical Review B* **81**, 020503 (2010).
- [26] T. Yildirim, *Physical Review Letters* **101**, 057010 (2008).
- [27] W. Malaeb, T. Shimojima, Y. Ishida, K. Okazaki, Y. Ota, K. Ohgushi, K. Kihou, T. Saito, C. H. Lee, S. Ishida, M. Nakajima, S. Uchida, H. Fukazawa, Y. Kohori, A. Iyo, H. Eisaki, C. T. Chen, S. Watanabe, H. Ikeda, and S. Shin, *Physical Review B* **85**, 224520 (2012).
- [28] S. Charpentier, G. Roberge, S. Godin-Proulx, X. Bechamp-Laganier, K. D. Truong, and P. Fournier, *Physical Review B* **81**, 104509 (2010).
- [29] Y. Nakai, T. Iye, S. Kitagawa, K. Ishida, H. Ikeda, S. Kasahara, H. Shishido, T. Shibauchi, Y. Matsuda, and T. Terashima, *Physical Review Letters* **105**, 107003 (2010).

- [30] T. Shimojima, K. Ishizaka, Y. Ishida, N. Katayama, K. Ohgushi, T. Kiss, M. Okawa, T. Togashi, X.-Y. Wang, C.-T. Chen, S. Watanabe, R. Kadota, T. Oguchi, A. Chainani, and S. Shin, *Physical Review Letters* **104**, 057002 (2010).
- [31] History of superconductivity, [https://en.wikipedia.org/wiki/History\\_of\\_superconductivity](https://en.wikipedia.org/wiki/History_of_superconductivity).
- [32] R. Li, X. Wu, Z. Chen, Y. Qian, C. Zhu, H. Wei, S. Wang, J. Sha, and J. Xia, *Physics Letters A* **144**, 35 (1990).
- [33] Y. Itoh, T. Machi, N. Koshizuka, M. Murakami, H. Yamagata, and M. Matsumura, *Physical Review B* **69**, 184503 (2004).
- [34] K. Levin, Q. Si, and Y. Zha, *Physica C: Superconductivity* **235–240, Part 1**, 71 (1994).
- [35] U. Schwingenschlogl and C. Schuster, *Physical Review Letters* **99**, 237206 (2007).
- [36] M. R. Norman, H. Ding, M. Randeria, J. C. Campuzano, T. Yokoya, T. Takeuchi, T. Takahashi, T. Mochiku, K. Kadowaki, P. Guptasarma, and D. G. Hinks, *Nature* **392**, 157 (1998).
- [37] J. N. Eckstein, I. Bozovic, D. G. Schlom, and J. S. H. Jr., *Applied Physics Letters* **57**, 1049 (1990).
- [38] K. Momma and F. Izumi, *J. Appl. Crystallogr.* **44**, (2011).
- [39] Mott insulator, [https://en.wikipedia.org/wiki/Mott\\_insulator](https://en.wikipedia.org/wiki/Mott_insulator).
- [40] J. Zaanen, G. A. Sawatzky, and J. W. Allen, *Physical Review Letters* **55**, 418 (1985).
- [41] M. J. Lawler, K. Fujita, J. Lee, A. R. Schmidt, Y. Kohasaka, C. K. Kim, H. Eisaki, S. Uchida, J. C. Davis, J. P. Sethna, and E.-A. Kim, *Nature* **466**, 347 (2010).
- [42] T. Sato, T. Kamiyama, T. Takahashi, K. Kurahashi, and K. Yamada, *Science* **291**, 1517 (2001).
- [43] S. Kashiwaya, T. Ito, K. Oka, S. Ueno, H. Takashima, M. Koyanagi, Y. Tanaka, and K. Kajimura, *Physical Review B* **57**, 8680 (1998).
- [44] V. J. Emery, *Phys. Rev. Lett.* **58**, 2794 (1987).

- [45] M. Hashimoto, Ph.D. thesis, The University of Tokyo, Tokyo, 2007.
- [46] M. Ikeda, Ph.D. thesis, The University of Tokyo, Tokyo, 2008.
- [47] S. ichiro Ideta, Ph.D. thesis, The University of Tokyo, Tokyo, 2011.
- [48] R. Yu and Q. Si, *Physical Review B* **86**, 085104 (2012).
- [49] Y. Tokura, S. Koshihara, T. Arima, H. Takagi, S. Ishibashi, T. Ido, and S. Uchida, *Physical Review B* **41**, 11657 (1990).
- [50] V. Cvetkovic and O. Vafek, *Physical Review B* **88**, 134510 (2013).
- [51] Z. X. Shen, W. E. Spicer, D. M. King, D. S. Dessau, and B. O. Wells, *Science* **267**, 343 (1995).
- [52] N. V. Smith, *Abstracts of papers of the American Chemical Society* **172**, 115 (1976).
- [53] P. K. Larsen, G. Margaritondo, J. E. Rowe, M. Schluter, and N. V. Smith, *Physical Letters A* **58**, 423 (1976).
- [54] H. Ding, M. R. Norman, J. C. Campuzano, M. Randeria, A. F. Bellman, T. Yokoya, T. Takahashi, T. Mochiku, and K. Kadowaki, *Physical Review B* **54**, R9678 (1996).
- [55] A. G. Loeser, Z.-X. Shen, D. S. Dessau, D. S. Marshall, C. H. Park, P. Fournier, and A. Kapitulnik, *Science* **273**, 325 (1996).
- [56] A. Damascelli, Z. Hussain, and Z.-X. Shen, *Rev. Mod. Phys.* **75**, 473 (2003).
- [57] Iron Pnictide Superconductors, <http://hoffman.physics.harvard.edu/materials-/Pnictides.php>.
- [58] S. Ishibashi, K. Terakura, and H. Hoson, *Journal of the Physical Society of Japan* **77**, 053709 (2008).
- [59] I. R. Shein and A. L. Ivanovskii, *Scripta Materialia* **59**, 1099 (2008).
- [60] K. Kuroki, H. Usui, S. Onari, R. Arita, and H. Aoki, *Physical Review B* **79**, 224511 (2009).
- [61] F.-C. Hsu, J.-Y. Luo, K.-W. Yeh, T.-K. Chen, T.-W. Huang, P. M. Wu, Y.-C. Lee, Y.-L. Huang, Y.-Y. Chu, D.-C. Yan, and M.-K. Wu, *Proceedings of the National Academy of Sciences* **105**, 14262 (2008).
- [62] D. Liu *et al.*, *Nature Communications* **3**, 931 (2012).

- [63] K. Suzuki, H. Usui, and K. Kuroki, *Journal of the Physical Society of Japan* **80**, 013710 (2011).
- [64] J. Knolle, I. Eremin, A. V. Chubukov, and R. Moessner, *Physical Review B* **81**, 140506 (2010).
- [65] M. M. Korshunov and I. Eremin, *Physical Review B* **78**, 140509 (2008).
- [66] P. J. Hirschfeld, M. M. Korshunov, and I. I. Mazin, *Reports on Progress in Physics* **74**, 124508 (2011).
- [67] T. Saito, S. Onari, and H. Kontani, *Physical Review B* **88**, 045115 (2013).
- [68] S. Graser, T. A. Maier, P. J. Hirschfeld, and D. J. Scalapino, *New Journal of Physics* **11**, 025016 (2009).
- [69] Y. Zhang, F. Chen, C. He, B. Zhou, B. P. Xie, C. Fang, W. F. Tsai, X. H. Chen, H. Hayashi, J. Jiang, H. Iwasawa, K. Shimada, H. Namatame, M. Taniguchi, J. P. Hu, and D. L. Feng, *Physical Review B* **83**, 054510 (2011).
- [70] R. M. Fernandes, L. H. VanBebber, S. Bhattacharya, P. Chandra, V. Keppens, D. Mandrus, M. A. McGuire, B. C. Sales, A. S. Sefat, and J. Schmalian, *Physical Review Letters* **105**, 157003 (2010).
- [71] S. Kasahara, H. J. Shi, K. Hashimoto, S. Tonegawa, Y. Mizukami, T. Shibauchi, K. Sugimoto, T. Fukuda, T. Terashima, A. H. Nevidomskyy, and Y. Matsuda, *Nature* **486**, 382 (2012).
- [72] R. M. Fernandes, D. K. Pratt, W. Tian, J. Zarestky, A. Kreyssig, S. Nandi, M. G. Kim, A. Thaler, N. Ni, P. C. Canfield, R. J. McQueeney, J. Schmalian, and A. I. Goldman, *Physical Review B* **81**, 140501 (2010).
- [73] T. Shang, L. Yang, Y. Chen, N. Cornell, F. Ronning, J. L. Zhang, L. Jiao, Y. H. Chen, J. Chen, A. Howard, J. Dai, J. D. Thompson, A. Zakhidov, M. B. Salamon, and H. Q. Yuan, *Physical Review B* **87**, 075148 (2013).
- [74] K. Hashimoto, T. Shibauchi, T. Kato, K. Ikada, R. Okazaki, H. Shishido, M. Ishikado, H. Kito, A. Iyo, H. Eisaki, S. Shamoto, and Y. Matsuda, *Phys. Rev. Lett.* **102**, 017002 (2009).
- [75] N. Terasaki, H. Mukuda, M. Yashima, Y. Kitaoka, K. Miyazawa, P. M. Shirage, H. Kito, H. Eisaki, and A. Iyo, *Journal of the Physical Society of Japan* **78**, 013701 (2009).

- [76] J. D. Fletcher, A. Serafin, L. Malone, J. G. Analytis, J.-H. Chu, A. S. Erickson, I. R. Fisher, and A. Carrington, *Phys. Rev. Lett.* **102**, 147001 (2009).
- [77] C. W. Hicks, T. M. Lippman, M. E. Huber, J. G. Analytis, J.-H. Chu, A. S. Erickson, I. R. Fisher, and K. A. Moler, *Physical Review Letters* **103**, 127003 (2009).
- [78] M. Yamashita, N. Nakata, Y. Senshu, S. Tonegawa, K. Ikada, K. Hashimoto, H. Sugawara, T. Shibauchi, and Y. Matsuda, *Physical Review B* **80**, 220509 (2009).
- [79] T. Shimojima, F. Sakaguchi, K. Ishizaka, Y. Ishida, T. Kiss, M. Okawa, T. Togashi, C.-T. Chen, S. Watanabe, M. Arita, K. Shimada, H. Namatame, M. Taniguchi, K. Ohgushi, S. Kasahara, T. Terashima, T. Shibauchi, Y. Matsuda, A. Chainani, and S. Shin, *Science* **332**, 564 (2011).
- [80] M. A. Tanatar, J.-P. Reid, H. Shakeripour, X. G. Luo, N. Doiron-Leyraud, N. Ni, S. L. Bud'ko, P. C. Canfield, R. Prozorov, and L. Taillefer, *Physical Review Letters* **104**, 067002 (2010).
- [81] K. Hashimoto, M. Yamashita, S. Kasahara, Y. Senshu, N. Nakata, S. Tonegawa, K. Ikada, A. Serafin, A. Carrington, T. Terashima, H. Ikeda, T. Shibauchi, and Y. Matsuda, *Physical Review B* **81**, 220501 (2010).
- [82] X. Qiu, S. Y. Zhou, H. Zhang, B. Y. Pan, X. C. Hong, Y. F. Dai, M. J. Eom, J. S. Kim, Z. R. Ye, Y. Zhang, D. L. Feng, and S. Y. Li, *Physical Review X* **2**, 011010 (2012).
- [83] H. Ding, P. Richard, K. Nakayama, K. Sugawara, T. Arakane, Y. Sekiba, A. Takayama, S. Souma, T. Sato, T. Takahashi, Z. Wang, X. Dai, Z. Fang, G. F. Chen, J. L. Luo, and N. L. Wang, *EPL (Europhysics Letters)* **83**, 47001 (2008).
- [84] K. Hashimoto, A. Serafin, S. Tonegawa, R. Katsumata, R. Okazaki, T. Saito, H. Fukazawa, Y. Kohori, K. Kihou, C. H. Lee, A. Iyo, H. Eisaki, H. Ikeda, Y. Matsuda, A. Carrington, and T. Shibauchi, *Physical Review B* **82**, 014526 (2010).
- [85] K. Okazaki *et al.*, *Science* **337**, 1314 (2012).
- [86] M. Yamashita, Y. Senshu, T. Shibauchi, S. Kasahara, K. Hashimoto, D. Watanabe, H. Ikeda, T. Terashima, I. Vekhter, A. B. Vorontsov, and Y. Matsuda, *Physical Review B* **84**, 060507 (2011).

- [87] Y. Zhang, Z. R. Ye, Q. Q. Ge, F. Chen, J. Jiang, M. Xu, B. P. Xie, and D. L. Feng, *Nature Physics* **8**, 371 (2012).
- [88] T. Yoshida *et al.*, *Scientific Reports* **4**, 7292 (2014).
- [89] J. Kang, A. F. Kemper, and R. M. Fernandes, *Physical Review Letters* **113**, 217001 (2014).
- [90] I. I. Mazin and J. Schmalian, *Physica C* **469**, 614 (2009).
- [91] K. Nakamura, R. Arita, and M. Imada, *Journal of the Physical Society of Japan* **77**, 093711 (2008).
- [92] T. M. McQueen, M. Regulacio, A. J. Williams, Q. Huang, J. W. Lynn, Y. S. Hor, D. V. West, M. A. Green, and R. J. Cave, *Physical Review B* **78**, 024521 (2008).
- [93] Y. Kamihara, H. Hiramatsu, M. Hirano, R. Kawamura, H. Yanagi, T. Kamiya, and H. Hosono, *Journal of the American Chemical Society* **128**, 10012 (2006).
- [94] H. Kontani and S. Onari, *Physical Review Letters* **104**, 157001 (2010).
- [95] Y. Yanagi, Y. Yamakawa, N. Adachi, and Y. Ōno, *Physical Review B* **82**, 064518 (2010).
- [96] M. Yoshizawa, D. Kimura, T. Chiba, S. Simayi, Y. Nakanishi, K. Kihou, C.-H. Lee, A. Iyo, H. Eisaki, M. Nakajima, and S. ichi Uchida, *Journal of the Physical Society of Japan* **81**, 024604 (2012).
- [97] T. Goto, R. Kurihara, K. Araki, K. Mitsumoto, M. Akatsu, Y. Nemoto, S. Tatematsu, and M. Sato, *Journal of the Physical Society of Japan* **80**, 073702 (2011).
- [98] H. Kontani and S. Onari, *Phys. Rev. Lett.* **104**, 157001 (2010).
- [99] S. Kasahara, T. Shibauchi, K. Hashimoto, K. Ikada, S. Tonegawa, R. Okazaki, H. Shishido, H. Ikeda, H. Takeya, K. Hirata, T. Terashima, and Y. Matsuda, *Physical Review B* **81**, 184519 (2010).
- [100] K. Hashimoto, K. Cho, T. Shibauchi, S. Kasahara, Y. Mizukami, R. Katsumata, Y. Tsuruhara, T. Terashima, H. Ikeda, M. A. Tanatar, H. Kitano, N. Salovich, R. W. Giannetta, P. Walmsley, A. Carrington, R. Prozorov, and Y. Matsuda, *Science* **336**, 1554 (2012).
- [101] S. A. Kivelson, E. Fradkin, and V. J. Emery, *Nature* **393**, 550 (1998).

- [102] S. Hufner, *Photoelectron Spectroscopy: Principles and Applications* (Springer, ADDRESS, 2003).
- [103] H. Ibach, in *Electron Spectroscopy for Surface Analysis*, edited by H. Ibach (Springer, ADDRESS, 1977), Vol. 4.
- [104] S. Tanuma, C. J. Powell, and D. R. Penn, *Journal of Vacuum Science and Technology A* **8**, 2213 (1990).
- [105] M. R. Norman, M. Randeria, H. Ding, and J. C. Campuzano, *Physical Review B* **57**, R11093 (1998).
- [106] F. Ning, K. Ahilan, T. Imai, A. S. Sefat, R. Jin, M. A. McGuire, B. C. Sales, and D. Mandrus, *Journal of the Physical Society of Japan* **77**, 103705 (2008).
- [107] H.-J. Grafe, D. Paar, G. Lang, N. J. Curro, G. Behr, J. Werner, J. Hamann-Borrero, C. Hess, N. Leps, R. Klingeler, and B. Büchner, *Physical Review Letters* **101**, 047003 (2008).
- [108] K. Matano, Z. A. Ren, X. L. Dong, L. L. Sun, Z. X. Zhao, and G. qing Zheng, *EPL (Europhysics Letters)* **83**, 57001 (2008).
- [109] K. Matano, Z. Li, G. L. Sun, D. L. Sun, C. T. Lin, M. Ichioka, and G. qing Zheng, *EPL (Europhysics Letters)* **87**, 27012 (2009).
- [110] M. Yashima, H. Nishimura, H. Mukuda, Y. Kitaoka, K. Miyazawa, P. M. Shirage, K. Kihou, H. Kito, H. Eisaki, and A. Iyo, *Journal of the Physical Society of Japan* **78**, 103702 (2009).
- [111] P. Jeglič, A. Potočnik, M. Klanjšek, M. Bobnar, M. Jagodič, K. Koch, H. Rosner, S. Margadonna, B. Lv, A. M. Guloy, and D. Arčon, *Physical Review B* **81**, 140511 (2010).
- [112] I. I. Mazin, D. J. Singh, M. D. Johannes, and M. H. Du, *Phys. Rev. Lett.* **101**, 057003 (2008).
- [113] S. V. Borisenko, V. B. Zabolotnyy, A. A. Kordyuk, D. V. Evtushinsky, T. K. Kim, I. V. Morozov, R. Follath, and B. Büchner, *Symmetry* **4**, 251 (2012).
- [114] Z. P. Yin, K. Haule, and G. Kotliar, *Nature Physics* **10**, 845 (2014).
- [115] L. Malone, J. D. Fletcher, A. Serafin, A. Carrington, N. D. Zhigadlo, Z. Bukowski, S. Katrych, and J. Karpinski, *Physical Review B* **79**, 140501 (2009).

- [116] R. T. Gordon, N. Ni, C. Martin, M. A. Tanatar, M. D. Vannette, H. Kim, G. D. Samolyuk, J. Schmalian, S. Nandi, A. Kreyssig, A. I. Goldman, J. Q. Yan, S. L. Bud'ko, P. C. Canfield, and R. Prozorov, *Physical Review Letters* **102**, 127004 (2009).
- [117] A. F. Kemper, T. A. Maier, S. Graser, H.-P. Cheng, P. J. Hirschfeld, and D. J. Scalapino, *New Journal of Physics* **12**, 073030 (2010).
- [118] W.-C. Lee, S.-C. Zhang, and C. Wu, *Physical Review Letters* **102**, 217002 (2009).